

CONTROL OF FLOW STRUCTURE ON LOW SWEPT DELTA WING USING
UNSTEADY LEADING EDGE BLOWING

A THESIS SUBMITTED TO
THE GRADUATE SCHOOL OF NATURAL AND APPLIED SCIENCES
OF
MIDDLE EAST TECHNICAL UNIVERSITY

BY

CENK ÇETİN

IN PARTIAL FULFILLMENT OF THE REQUIREMENTS
FOR
THE DEGREE OF MASTER OF SCIENCE
IN
MECHANICAL ENGINEERING

JUNE 2016

Approval of the thesis:

**CONTROL OF FLOW STRUCTURE ON LOW SWEPT DELTA WING
USING UNSTEADY LEADING EDGE BLOWING**

submitted by **CENK ÇETİN** in partial fulfillment of the requirements for the degree of **Master of Science in Mechanical Engineering Department, Middle East Technical University** by,

Prof. Dr. Gülbin Dural Ünver
Dean, Graduate School of **Natural and Applied Sciences**

Prof. Dr. R. Tuna Balkan
Head of Department, **Mechanical Engineering**

Assoc. Prof. Dr. Mehmet Metin Yavuz
Supervisor, **Mechanical Engineering Dept., METU**

Examining Committee Members:

Prof. Dr. Kahraman Albayrak
Mechanical Engineering Dept., METU

Assoc. Prof. Dr. M. Metin Yavuz
Mechanical Engineering Dept., METU

Assoc. Prof. Dr. Cüneyt Sert
Mechanical Engineering Dept., METU

Assoc. Prof. Dr. Oğuz Uzol
Aerospace Engineering Dept., METU

Assoc. Prof. Dr. Emrah Özahi
Mechanical Engineering Dept., Gaziantep University

Date: 29.06.2016

I hereby declare that all information in this document has been obtained and presented in accordance with academic rules and ethical conduct. I also declare that, as required by these rules and conduct, I have fully cited and referenced all material and results that are not original to this work.

Name, Last name: Cenk Çetin

Signature :

ABSTRACT

CONTROL OF FLOW STRUCTURE ON LOW SWEPT DELTA WING USING UNSTEADY LEADING EDGE BLOWING

Çetin, Cenk

M.S., Department of Mechanical Engineering

Supervisor : Assoc. Prof. Dr. Mehmet Metin Yavuz

June 2016, 97 pages

There is an increasing interest in recent years in the aerodynamics of low swept delta wings, which can be originated from simplified planforms of Unmanned Air Vehicles (UAV), Unmanned Combat Air Vehicles (UCAV) and Micro Air Vehicles (MAV). In order to determine and to extend the operational boundaries of these vehicles with particular interest in delaying stall, complex flow structure of low swept wings and its control needs to be understood.

Among different flow control strategies, blowing through different locations of the wing has been commonly used due to its high effectiveness. Steady and unsteady blowing with different configurations in terms of excitation pattern at different injection rates needs to be studied thoroughly.

In the current study, it is aimed to control the flow structure of a low swept delta wing with sweep angle of $\Lambda=45^\circ$ using unsteady blowing through leading edges. Experiments are conducted in low speed wind tunnel. First, the unsteady blowing test set-up, which is able to provide a broad range of periodic excitation frequencies and injection rates, is built and characterized using Hot Wire Anemometry. Then, the flow structure on the wing is quantified using surface

pressure measurements and Particle Image Velocimetry (PIV) technique for the attack angles varying from 7 to 20 degrees at Reynolds number of $Re=35000$. Different periodic excitation frequencies, varying from 2 Hz to 24 Hz, at fix momentum coefficient are tested and compared with the steady injection cases. The results indicate that unsteady blowing through leading edges of the planform is quite effective for the eradication of stall.

Keywords: Delta wing, Low swept delta wings, Leading edge vortex, Active flow control, Unsteady leading edge blowing.

ÖZ

DÜŞÜK OK AÇILI DELTA KANAT ÜZERİNDEKİ AKIŞ YAPISININ HÜCUM KENARLARINDAN ZAMANA BAĞLI ÜFLEME İLE KONTROLÜ

Çetin, Cenk

Yüksek Lisans, Makina Mühendisliği Bölümü
Tez Yöneticisi : Doç. Dr. Mehmet Metin Yavuz

Haziran 2016, 97 sayfa

İnsansız Hava Araçları (İHA), İnsansız Savaş Araçları ve Mikro Hava Araçları'nın basitleştirilmiş planformlarından olan düşük ok açılı delta kanatların aerodinamik özellikleri üzerine son yıllarda artan bir ilgi bulunmaktadır. Özellikle perdövites durumunun geciktirilmesine yönelik olarak, bu araçların operasyonel sınırlarının belirlenmesi ve genişletilmesi için, düşük ok açılı delta kanatların akış yapılarının ve kontrolünün anlaşılması gerekmektedir.

Kanadın muhtelif bölgelerinden üfleme tekniği sahip olduğu yüksek verimlilik sebebiyle çeşitli akış kontrol stratejileri arasında sıklıkla kullanılmaktadır. Daimi ve zamana bağlı üfleme tekniğinin değişen üfleme oranlarında farklı tahrik yapıları ile oluşturulabilecek konfigürasyonlarının derinlemesine çalışılması gerekmektedir.

Bu çalışmada 45 derece ok açılı delta kanat akış yapısının, kanat ucundan zamana bağlı üfleme tekniği ile kontrol edilmesi amaçlanmıştır. Deneyler düşük hızlı rüzgar tüneline gerçekleştirilmiştir. İlk olarak geniş bir aralıkta periyodik tahrik frekansı ve üfleme oranlarını sağlayabilen zamana bağlı üfleme akış kontrol deney

düzenine kurulmuş ve Kızgın Tel Anemometre (HWA) ile karakterizasyonu yapılmıştır. Daha sonra delta kanat üzerindeki akış yapısı, Reynolds sayısı $Re=35000$ 'de, 7 dereceden 20 dereceye kadar olan hücum açıları için, yüzey basınç ölçümleri ve parçacık görüntülemeli hız ölçme tekniği (PIV) ile nicelendirilmiştir. Sabit üfleme katsayısında 2 Hz ile 24 Hz arasında değişen periyodik tahrik frekansları test edilerek, daimi üfleme durumları ile karşılaştırılmıştır. Elde edilen sonuçlar kanat hücum kenarından yapılan zamana bağlı üfleme tekniğinin perdövitesi önlenmesinde oldukça etkili olduğunu göstermiştir.

Anahtar Kelimeler: Delta kanat, düşük ok açılı delta kanatlar, Hücum kenarı girdabı, Aktif akış kontrolü, Kanat hücum kenarından zamana bağlı üfleme tekniği.

To my parents

ACKNOWLEDGMENTS

I would like to express my deepest gratitude to my thesis supervisor, Dr. Mehmet Metin Yavuz, for his continuous guidance, encouragement, criticism, support and insight throughout the research. Without him, this thesis could not be as improved as it is now. I am also thankful to him for his accepting me to join Yavuz Research Group *YRG*, it has been a great chance for me to gain invaluable hands on experiences and a deep knowledge in the field.

I would like to express my gratitude to my parents for their invaluable love. Awareness of being loved no matter what you do must be the most comforting feeling in the world.

I would like to thank to Dr. Ayşegül Abuşoğlu and Dr. Sadettin Kapucu from University of Gaziantep for their recommendation of me to apply Middle East Technical University. And also I owe my sincere acknowledgement to Dr. Kahraman Albayrak and Dr. Emrah Özahi for sharing their valuable experiences in the experimental fluid mechanics field.

This thesis would not have been possible without the help and support of my dearest friends and colleagues Alper Çelik, Mahmut Murat Göçmen, Dr. Ali Karakuş, Gizem Şencan, Burak Gülsaçan, Gökay Günacar, Mohammad Reza Zharfa and İlhan Öztürk.

The technical assistance of Mr. Rahmi Ercan and Mr. Mehmet Özçiftçi are gratefully acknowledged.

I would also like to express my sincere thanks to Dr. Oğuz Uzol from METU Aerospace Engineering Department for sharing their experimental apparatus.

TABLE OF CONTENTS

ABSTRACT.....	v
ÖZ.....	vii
ACKNOWLEDGMENTS	x
TABLE OF CONTENTS.....	xi
LIST OF TABLES	xiii
LIST OF FIGURES	xiv
NOMENCLATURE.....	xviii
CHAPTERS	
1. INTRODUCTION	1
1.1 Motivation.....	3
1.2 Aim of the Study	3
1.3 Structure of the Thesis	4
2. LITERATURE SURVEY	7
2.1 Flow Past Delta Wings.....	7
2.1.1 Separated Shear Layers and Instabilities	9
2.1.2 Vortex Breakdown	10
2.1.3 Flow Reattachment	12
2.2 Delta Wing Flow Control Techniques	13
2.2.1 Passive Control	14
2.2.2 Active Control.....	15
2.2.2.1 Unsteady Forcing	17
3. EXPERIMENTAL SET-UP AND TECHNIQUES.....	27
3.1 Wind Tunnel Facility	27

3.1.1 Wind Tunnel Characterization	28
3.2 Delta Wing Model	28
3.3 Flow Control Set-up	29
3.3.1 Blowing Scenario	31
3.3.2 Unsteady Blowing Measurements via Hot Wire Anemometry	32
3.4 Pressure Measurements	33
3.5 Particle Image Velocimetry (PIV) Measurements	35
3.6 Uncertainty Estimates.....	36
4. RESULTS AND DISCUSSION.....	49
4.1 Blowing Characterization.....	49
4.1.1 Unsteady Blowing Cases	49
4.1.2 Steady Blowing Cases	52
4.2 Surface Pressure Measurement Results.....	53
4.2.1 Spectral Analysis of the Pressure Measurements	57
4.3 Particle Image Velocimetry Measurement Results	58
5. CONCLUSION	73
5.1 Summary and Conclusions.....	73
5.2 Recommendations for Future Work.....	75
REFERENCES	77
APPENDICES	
A. UNSTEADY BLOWING MEASUREMENTS RAW DATA.....	85
B. SOURCE CODES FOR PRESSURE COEFFICIENT CALCULATION	89
C. PRESSURE MEASUREMENT RESULTS.....	93

LIST OF TABLES

TABLES

Table 3.1 Relative uncertainties of the measured variables used in momentum coefficient calculation	377
Table 4.1 Momentum coefficient values calculated from the mean of the peak velocities at the valve-open condition.....	51
Table 4.2 Momentum coefficient values calculated for different hole locations...	52

LIST OF FIGURES

FIGURES

Figure 1.1 Schematic representation of shear layer and leading edge vortices over a delta wing [3].	5
Figure 1.2 Delta wing vortex formation: main delta wing flow features (a) and vortex bursting characteristics (b) [5].	5
Figure 1.3 Schematic streamline patterns for (a) reattachment over nonslender wings and (b) with no reattachment on wing surface on slender [3].	6
Figure 1.4 Effectiveness of unsteady and steady blowing techniques [3].	6
Figure 2.1 Sketch of dual vortex formation [23].	20
Figure 2.2 Spectrum of unsteady flow phenomena over delta wings [6].	20
Figure 2.3 Illustration of free shear layer, rotational core and viscous subcore over a delta wing [30].	21
Figure 2.4 Mean axial velocity profile through the vortex core [20].	21
Figure 2.5 Instantaneous vortex structure over a delta wing [20].	22
Figure 2.6 Vortex breakdown visualization [40].	22
Figure 2.7 Magnitude of time-averaged velocity and streamline pattern near the wing surface in water-tunnel experiments. breakdown visualization [31].	23
Figure 2.8 Boundaries of vortex breakdown and flow reattachment as a function of angle of attack and sweep angle [3].	23
Figure 2.9 Variation of the time-averaged lift coefficient for a flexible delta wing [48].	24
Figure 2.10 Different control loops for active flow control [46].	24
Figure 2.11 Optimum effectiveness of various blowing/suction techniques [3].	25
Figure 2.12 Cross flow PIV measurements for unsteady blowing [87].	25
Figure 3.1 View from wind tunnel facility (a) and test section (b).	39
Figure 3.2 Wind tunnel calibration graph.	40
Figure 3.3 Wing model plan and back view.	40

Figure 3.4 Isometric view of the wing model.	41
Figure 3.5 Photographs of fabricated wing.	41
Figure 3.6 Wing model, mount and test section assembly.	42
Figure 3.7 Unsteady blowing flow control setup.	42
Figure 3.8 MHJ9-QS-4-MF solenoid valve (a), MHJ9-KMH control module (b), photos courtesy of FESTO corp.	43
Figure 3.9 Unsteady blowing control setup block diagram in LabVIEW environment.	43
Figure 3.10 NI cRIO 9263 DAQ Card and circuitry, photo courtesy of National Instrument corp.	44
Figure 3.11 Experimental Matrix.	44
Figure 3.12 CTA Bridge Circuit.	45
Figure 3.13 CTA Main Unit.	45
Figure 3.14 Dantec 55P16 hot wire probe.	45
Figure 3.15 CTA measurement chain.	46
Figure 3.16 Hot wire calibration curve and data.	46
Figure 3.17 Custom designed platform for hot wire probe.	47
Figure 3.18 Pressure scanner device and wing tubing connections.	47
Figure 3.19 Scheme of the PIV experiment set-up.	48
Figure 4.1 Time series of unsteady blowing jet velocity (moving average applied) for all excitation frequencies.	60
Figure 4.2 Power spectral densities of unsteady blowing jet velocity for 4 Hz and 16 Hz excitation frequencies.	62
Figure 4.3 Power spectral density of unsteady blowing jet velocity in log-log domain for 24 Hz excitation frequency.	62
Figure 4.4 Time series of unsteady blowing jet velocity at different hole locations for 8 Hz excitation frequency on a random flow meter adjustment.	63
Figure 4.5 Time series of steady blowing jet velocity for $C_{\mu}=0.0025$ and $C_{\mu}=0.01$	63
Figure 4.6 Spanwise $-C_p$ distribution on $x/C=0.56$ at $\alpha=7^\circ$ and $Re=35000$ for selected cases.	64

Figure 4.7 Spanwise $-C_p$ distribution on $x/C=0.56$ at $\alpha=13^\circ$ and $Re=35000$ for selected cases.....	64
Figure 4.8 Spanwise $-C_p$ distribution on $x/C=0.56$ at $\alpha=16^\circ$ and $Re=35000$ for selected cases.....	65
Figure 4.9 Spanwise $-C_p$ distribution on $x/C=0.56$ at $\alpha=20^\circ$ and $Re=35000$ for selected cases.....	65
Figure 4.10 Spanwise $-C_p$ distribution on $x/C=0.56$ for no control, steady control with $C_\mu=0.0025$, steady control with $C_\mu=0.01$ and unsteady control with 16 Hz excitation frequency for different attack angles at $Re=35000$	66
Figure 4.11 Spanwise $C_{p,RMS}$ distribution on $x/C=0.56$ at $\alpha=7^\circ$ and $Re=35000$ for selected cases.....	67
Figure 4.12 Spanwise $C_{p,RMS}$ distribution on $x/C=0.56$ at $\alpha=13^\circ$ and $Re=35000$ for selected cases.....	67
Figure 4.13 Spanwise $C_{p,RMS}$ distribution on $x/C=0.56$ at $\alpha=16^\circ$ and $Re=35000$ for selected cases.....	68
Figure 4.14 Spanwise $C_{p,RMS}$ distribution on $x/C=0.56$ at $\alpha=20^\circ$ and $Re=35000$ for selected cases.....	68
Figure 4.15 Power spectral densities of pressure signals measured at $x/C=0.56$ and $y/S=0.63$ for all attack angles (4 Hz excitation frequency on the left and 16 Hz excitation frequency on the right).....	69
Figure 4.16 Time averaged cross flow velocity vectors at $x/C=0.56$ and $\alpha=16^\circ$ for no control, steady control $C_\mu=0.0025$, 0.01 and unsteady control with 4, 16 Hz excitation frequencies.....	70
Figure 4.17 Time averaged cross flow vorticity contours at $x/C=0.56$ and $\alpha=16^\circ$ for no control, steady control $C_\mu=0.0025$, 0.01 and unsteady control with 4, 16 Hz excitation frequencies.....	71
Figure 4.18 Time averaged cross flow streamline patterns at $x/C=0.56$ and $\alpha=16^\circ$ for no control, steady control $C_\mu=0.0025$, 0.01 and unsteady control with 4, 16 Hz excitation frequencies.....	72
Figure A.1 Time series of unsteady blowing jet velocity for all excitation frequencies.....	85

Figure A.2 Power spectral densities of unsteady blowing jet velocity for the remaining frequencies.	87
Figure C.1 Spanwise $-C_p$ distribution on $x/C=0.56$ at $\alpha=7^\circ$ and $Re=35000$ for all cases.	94
Figure C.2 Spanwise $-C_p$ distribution on $x/C=0.56$ at $\alpha=13^\circ$ and $Re=35000$ for all cases.	94
Figure C.3 Spanwise $-C_p$ distribution on $x/C=0.56$ at $\alpha=16^\circ$ and $Re=35000$ for all cases.	95
Figure C.4 Spanwise $-C_p$ distribution on $x/C=0.56$ at $\alpha=20^\circ$ and $Re=35000$ for all cases.	95
Figure C.5 Spanwise $C_{p,RMS}$ distribution on $x/C=0.56$ at $\alpha=7^\circ$ and $Re=35000$ for all cases.	96
Figure C.6 Spanwise $C_{p,RMS}$ distribution on $x/C=0.56$ at $\alpha=13^\circ$ and $Re=35000$ for all cases.	96
Figure C.7 Spanwise $C_{p,RMS}$ distribution on $x/C=0.56$ at $\alpha=16^\circ$ and $Re=35000$ for all cases.	97
Figure C.8 Spanwise $C_{p,RMS}$ distribution on $x/C=0.56$ at $\alpha=20^\circ$ and $Re=35000$ for all cases.	97

NOMENCLATURE

Λ	Sweep angle
C	Chord length
S	Semi span length
α	Angle of attack
Re	Reynolds number based on chord length
U_∞	Free stream velocity
V	Velocity vector
U_j	Blowing jet exit velocity
\bar{U}_j	Mean of the blowing jet exit velocity during valve open state
u	Streamwise velocity
ω	Vorticity
ψ	Streamfunction
x	Chordwise distance from wing apex
y	Spanwise distance from wing root chord
f	Frequency
St	Dimensionless frequency
p	Static pressure
\bar{p}	Average of the static pressure
p_{RMS}	Root mean square of the static pressure
p_∞	Static pressure of the flow
p_{dyn}	Dynamic pressure of the flow
p_{supply}	Valve supply pressure
C_p	Dimensionless pressure coefficient
$C_{p,RMS}$	Root mean square of the pressure coefficient
ρ	Fluid density
ν	Fluid kinematic viscosity
N	Number of samples in a measurement

C_μ	Momentum coefficient
$C_{\mu,eff}$	Effective momentum coefficient
$C_{\mu,max}$	Maximum momentum coefficient
PIV	Particle Image Velocimetry
HWA	Hot Wire Anemometry
ω_i	Uncertainty estimate of a variable i
u_i	Relative uncertainty estimate

CHAPTER 1

INTRODUCTION

Increasing popularity of Micro Air Vehicles (MAV), Unmanned Combat Air Vehicles (UCAV) and Unmanned Air Vehicles (UAV) for commercial and military purposes in recent years, attracts aerodynamicists to work on possible techniques in order to extend the operational boundaries of low swept (non-slender) delta wings which constitute a basis for the design and analysis of some of these vehicles [1]. These vehicles experience complex flow structures during steady flight conditions or under defined maneuvers. For optimization of delta wing's flight performances, these complex flow structures must be well understood [2,3].

Delta wings are classified according to their sweep angles as, slender (with sweep angles greater than 55°) and non-slender (with sweep angles between 35° and 55°) delta wings. Although much effort has been dedicated to slender (high swept) delta wings, there are very few studies addressing the unsteady behavior of non-slender delta wings and the effects of Reynolds number, angle of attack and control techniques on flow structure. Earnshaw and Lawford [4] showed that the lift coefficient is directly proportional to the sweep angle in a certain range, and as the sweep angle decreases, the critical angle of attack also decreases. Actually this relation among above parameters has pushed numerous studies in literature as becoming a key point.

The flow over delta wing at angle of attack separates from windward side of the leading edges then turns into curved free shear layers [3], whose further formation generally depends upon the sweep angle and also on the angle of attack. Two counter rotating leading edge vortices dominate the flow at a moderate

incidence over slender delta wings. The sketch of leading edge vortices over a slender delta wing is shown in Figure 1.1 [3]. This primary vortex structure is said to be fully developed as long as its formation exists along the entire leading edge [5]. The interaction of the primary vortex with the boundary layer developing at the inboard of the wing is resulted with secondary vortex formation rotating in opposite direction with respect to primary vortices, which can be seen also for non-slender delta wings at low incidences [1, 5].

Increase in attack angle causes formation of different forms of instabilities including vortex breakdown, vortex shedding, vortex wandering, helical mode instability, and shear layer instability [1]. Vortex breakdown comes out at higher incidences such that the jet like axial core flow stagnates and results with the sudden expansion of the core as summarized by Breitsamter [5]. As stated in Gursul [6], breakdown formation and motion are generally affected by two main parameters: swirl level and pressure gradient. Figure 1.2 [5] shows the main flow structure over a delta wing with the schematic representation of vortex breakdown.

In addition to the aforementioned instabilities, recent investigations reveal the significance of the reattachment of the flow to the wing surface, which is separated from the leading edge [6]. For slender delta wings reattachment line is through the inboard of the vortex core that occurs only at low incidences, whereas the shear layer separated from leading edge may reattach to the wing surface for non-slender delta wings constituting a vortex bound which may occur even after vortex breakdown [3]. Figure 1.3 shows the schematic of the cross flow pattern for both types of the wings.

At sufficiently high angle of attack, onset of the breakdown location is shifted closer the wing apex and when it reaches to the apex the wing is completely stalled [5]. For non-slender delta wings primary attachment location is through the outboard of the wing root chord, even when the breakdown approaches to apex. Increasing attack angle moves the attachment line towards the inboard plane that causes the considerable buffeting within the attachment region. And a further

increase in angle of attack causes the eradication of flow reattachment which is resulted with the coalescence of vortex bounds from both sides of the wings together with the stall of the wing [1].

In order to control of the leading edge vortices, blowing technique has been widely utilized using pneumatic devices. Blowing which is an effective technique for energizing the leading edge vortices can be implemented with various configurations such as: leading edge blowing, trailing edge blowing and along core blowing [3]. Application of these methods could be conducted in steady and unsteady (periodic) ways. There is a well-documented knowledge on steady applications. The interest has been increased for unsteady blowing control within the last decades.

1.1 Motivation

Micro Air Vehicles (MAV), Unmanned Combat Air Vehicles (UCAV) and Unmanned Air Vehicles (UAV) experience complex flow patterns during steady flight and/or defined maneuvers which must be first well understood and then controlled in order to optimize the flight performances including the enhancement in lift and the reduction in buffet loading etc. Gursul et al. [3] outlined the effectiveness of blowing technique both for steady and unsteady applications mainly from studies for slender wings as shown in Figure 1.4. As indicated in that figure, unsteady forcing has more potential to regulate the flow structure compared to the steady practices for slender wings. The studies of flow control on low swept wings using steady and/or unsteady blowing techniques would ultimately help to construct similar effectiveness charts for low swept wings which could be used for flight performance optimizations of aforementioned air vehicles.

1.2 Aim of the Study

The current study aims to control the flow past a delta wing with 45° sweep angle using unsteady leading edge blowing technique. For this purpose, first, the flow control setup was designed and built, which was able to supply unsteady blowing

at different excitation patterns and frequencies from the leading edges of the wing model. Generated unsteady patterns and frequencies were characterized in detail using hot wire anemometry (HWA) measurements. Then, the flow structure on the wing was quantified using surface pressure measurements and Particle Image Velocimetry (PIV) technique for the attack angles varying from 7 to 20 degrees at Reynolds number of $Re=35000$. The measurements were performed at square pattern excitation for a duty cycle of 25% at fix momentum coefficient. Different periodic excitation frequencies, varying from 2 Hz to 24 Hz, were tested and compared with the steady injection case.

1.3 Structure of the Thesis

This thesis is composed of five main chapters. Chapter 1 provides introductory information for the delta wing flows and the aim of the study along with the motivation.

The related previous studies including the flow structure on delta wings and flow control techniques are summarized and discussed in Chapter 2. The topics related to slender delta wings are briefly mentioned and the major attention is given to the non-slender delta wings.

Technical details of the flow control set-up and the measurement systems used in the current study are given in Chapter 3. The methodology followed for conducting the unsteady blowing measurements is discussed in detail.

The results are summarized and discussed in Chapter 4. First, the characterization of the unsteady blowing set-up is given. Then, the pressure measurement results are reported. Finally, the results of the Particle Image Velocimetry (PIV) experiments are presented.

Chapter 5 provides the conclusions throughout the study including the recommendations for possible future work.

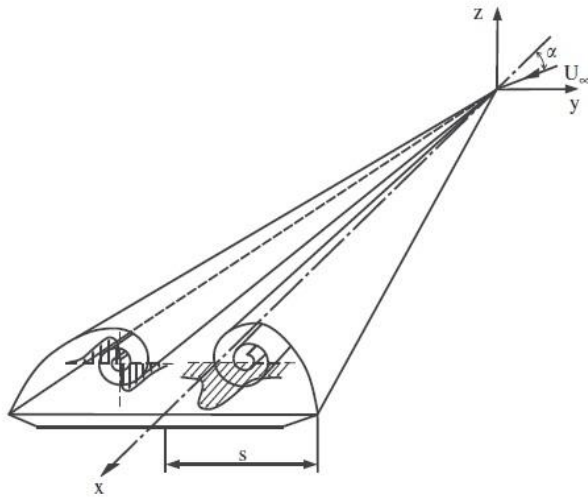


Figure 1.1 Schematic representation of shear layer and leading edge vortices over a delta wing [3].

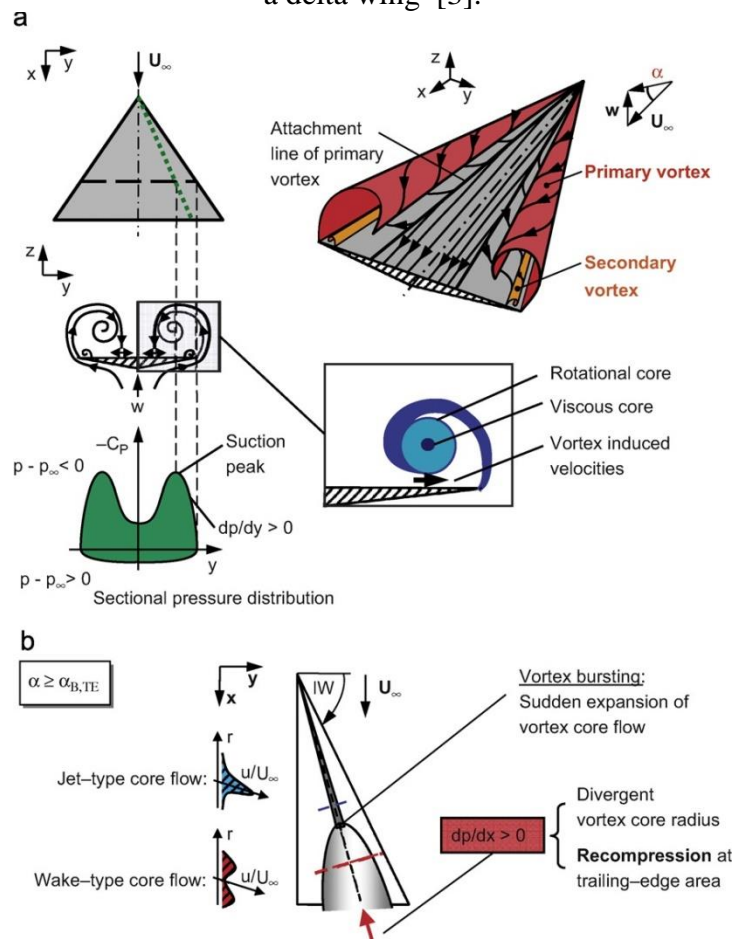


Figure 1.2 Delta wing vortex formation: main delta wing flow features (a) and vortex bursting characteristics (b) [5].

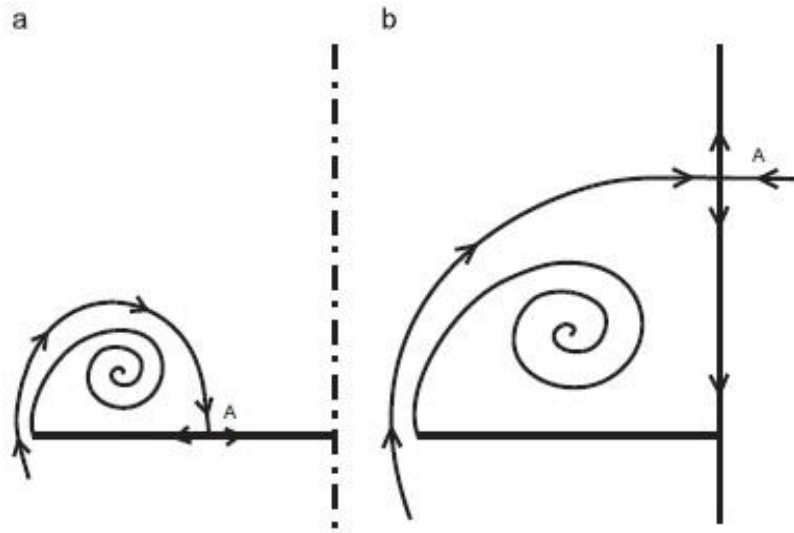


Figure 1.3 Schematic streamline patterns for (a) reattachment over nonslender wings and (b) with no reattachment on wing surface on slender [3].

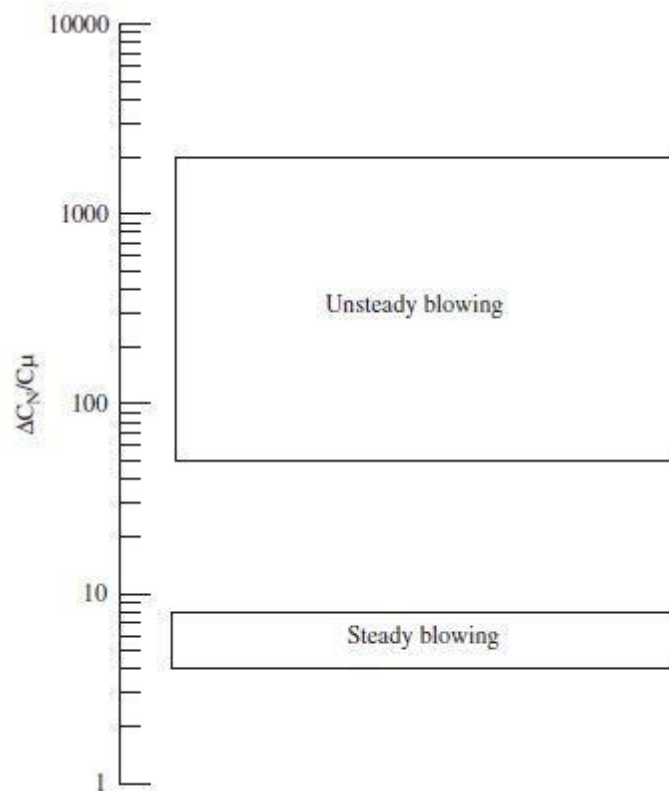


Figure 1.4 Effectiveness of unsteady and steady blowing techniques [3].

CHAPTER 2

LITERATURE SURVEY

2.1 Flow Past Delta Wings

Flow structure over slender delta wings has been extensively investigated, whose foundation may be told as well established. Although there are comparably less studies on non-slender delta wings in the literature, it is seen that major differences take place between respective flow structures. In this topic individual flow characteristics of slender and non-slender delta wings are given with comparisons and similarities.

The flow past a delta wing is prevailed by two counter rotating leading edge vortices that are developed by rolling up vortex sheets. The free stream separates through the leading edges that turns into curved free shear layers over the suction side of the wing [3]. For slender delta wings, the time averaged axial velocity of the vortex core can be as large as four or five times of the upstream velocity [6]. Considering the energy conservation of the flow over the wing, there occur low pressure and high velocity couple on the suction side compared to the free stream conditions, which generates lift force on the wing. Some of the early studies proposing the aerodynamics of delta wings were conducted by Werle [7], Earnshaw and Lawford [4], Bird [8], Polmhamus [9] and Erickson [10]. In these studies, vortex breakdown due to increasing angle of attack could also be reported. Further contributions to vortex breakdown concept were made by researchers involving Benjamin [11, 12], Sarpkaya [13-15], Wedemayer [16] and Escudier [17]. The separated flow forms into the discrete vortices over the slender wings as inspected by Gad-el-Hak and Blackwelder [18]. The vortex formation at low incidences on non-slender delta wings is closer to the wing surface compared

to the slender wings as observed by Ol and Gharib [19]. This formation triggers the further major differences in the flow structure like; reattachment, boundary layer interaction and further vortex formations. Since the secondary flow separating from the wing surface splits primary vortex, non-slender delta wings experience dual vortex structure in the main core at low angle of attacks. Gordnier and Visbal [20] first identified this dual vortex structure computationally. The Particle Image Velocimetry (PIV) measurements performed by Taylor et al. [21] and Yaniktepe and Rockwell [22] evidenced the formation of dual vortex structure. Jin-Jun and Wang [23] conducted an extensive experimental study proposing the development of the dual vortex over the delta wings with sweep angles ranging from 45° to 65° at moderate Reynolds numbers of $1.2 \cdot 10^4$ and $1.8 \cdot 10^4$. It was seen that as the sweep angle increases the range of the attack angle having dual vortex decreases. Figure 2.1 shows the sketch of dual vortex structure [23].

There was less severe attention given to the unsteady nature of these flow structures until 1990's, which is not important only for performance and stability issues but also for endurance of the wings against buffet loading which may cause vibration therefore the fatigue damage. Ashley et al. [24], Rockwell [25], Gordnier and Visbal [26] and Gursul [27] were among the researchers in 1990's studying the unsteady aspect of vortex flow and vortex breakdown over slender delta wings. As the importance of unsteady aerodynamics was understood, contribution to the field had been increased by researchers involving Menke et al. [28] and Gursul and Xie [29]. Nelson and Pelletier [30] proposed an important review for unsteady behavior considering dynamic movements of slender delta wings with suggesting a nonlinear aerodynamic model. Gursul [6] also summarized unsteady aspects both for stationary and dynamic slender wings, classifying according to shear layer instabilities, vortex wandering, vortex breakdown by relating them with wing buffeting. Figure 2.2 shows the spectrum of unsteadiness on delta wings as a function of dimensionless frequency called Strouhal Number [6]. When non-slender delta wings are considered, number of attempts identifying their unsteady aspects has been increased in order to enhance

aerodynamic capabilities in the last decades, as a result of increasing application of UAV's, UCAV's, and MAV's, but they are still limited. Taylor and Gursul [31] conducted Particle Image Velocimetry (PIV) and Laser Doppler Anemometer (LDA) measurements to identify the unsteady vortex flow and buffeting response on a delta wing of sweep angle $\Lambda=50^\circ$. Yanıktepe and Rockwell [22] applied the technique of high image density PIV to relate the vortex breakdown – stall conditions to the buffeting mechanism as a function of attack angle for a delta wing of sweep angle $\Lambda=38.7^\circ$. Yavuz et al. [32] identified the near surface flow patterns with high image density PIV technique for a delta wing of sweep angle $\Lambda=38.7^\circ$ also reporting the effect of wing perturbations experiencing transient motions. Breitsamter [5] presented a comparative study investigating the unsteady flow phenomena both for a slender delta wing $\Lambda=76^\circ$ and a detailed aircraft configuration of canard - delta wing type with sweep angles $\Lambda=45^\circ$ and $\Lambda=50^\circ$ respectively. Öztürk [33] performed surface pressure measurements together with LDA measurements for a delta wing of sweep angle $\Lambda=45^\circ$ to figure out three dimensional separation of flow and unsteady nature. Zharfa et al.[34] characterized the flow structure over a $\Lambda=35^\circ$ delta wing with laser illuminated flow visualization, Laser Doppler Anemometry and pressure measurements over a broad range of Reynolds number and angle of attack.

2.1.1 Separated Shear Layers and Instabilities

According to viscous flow theory, if the flow in contact with a body experiences an adverse pressure gradient, separation occurs. Right after the separation, boundary layer theory is not valid anymore. When the sharp edge wings are the case, separation is always on the sharp leading edges. Earnshaw [35] stated that, the vortex occurring as result of separation through the leading edges of a delta wing could be investigated in three different regions called; free shear layer, rotational core and viscous subcore. In the Figure 2.3 three regions within a leading edge vortex are illustrated [30]. Yanıktepe and Rockwell [22] summarized the vortex flow structure according to large scale patterns and small scale patterns. Instabilities are generally linked to the small scale patterns of the

vortex structure. Figure 2.4 shows the mean axial core velocity profile along the spanwise direction from the numerical simulations for a $\Lambda=50^\circ$ sweep delta wing [20]. The vortex formation in the separated shear layer is generally associated with two dimensional Kelvin-Helmholtz type of instability. Gad-el-Hak and Blackwelder [18] first observed these unstable formations both for slender and non-slender delta wings with $\Lambda=60^\circ$ and $\Lambda=45^\circ$ respectively. Özgören et al. [36] brought an additional insight to the unsteady flow nature of a $\Lambda=75^\circ$ sweep delta wing at high angle of attacks up to $\alpha=35^\circ$ at Reynolds number of $1.07 \cdot 10^4$, which is also in line with the time varying instabilities observed by Riley and Lowson [37]. For a $\Lambda=38.7^\circ$ sweep delta wing Yavuz et al. [32] showed the average vorticity regions that indicates the co-rotating pattern of small scale vorticity concentrations. In their numerical study, Gordnier and Visbal [20] concluded that shear layer instability is a bursting outcome of the previously mentioned secondary flow due to the interaction of primary vortex with surface boundary layers which is resulted with serious movement of vortex core periodically around the mean direction so called vortex wandering. Figure 2.5 illustrates the instantaneous vortex structure over a delta wing of $\Lambda=50^\circ$ [20].

2.1.2 Vortex Breakdown

Vortex breakdown can be simply defined as the abrupt change in vortex flow structure with a very apparent retardation in the jet like axial flow that is resulted with expansion of the core until the boundaries of the flow field, which may be the case for most of the swirling flows [38]. Vortex breakdown takes place over a delta wing at higher incidences, at which the axial flow upstream behaves as wake like flow with a considerably low velocity [3]. The answer of the question what happens when the vortex breaks down is that: as a result of decreasing velocity, pressure increases on the suction side therefore there occurs the dramatic drop in both lift and momentum coefficients, which means the loss of aerodynamic capabilities up to stall conditions. In their review paper, Lucca-Negro and O'doherty classified vortex breakdown under seven different types [39]. The types observed over delta wings commonly are bubble and spiral types,

where slender delta wings generally exhibit spiral type [7]. For slender wings, the picture just after the breakdown is the occurrence of negative axial velocity due to the switch of the vortex core to rotate in the reverse direction of the original rotation. Among the different approaches over vortex breakdown phenomenon like hydrodynamic instability, wave propagation and flow stagnation, it is widely accepted that, it is the wave propagation analogous to shocks in gas dynamics [6]. Early qualitative observation on vortex breakdown in experimental manner could be achieved with visualization of streaklines by injecting dye or smoke to the flow field depending upon the testing environment [1]. One of the early studies in the field was given by Lambourne and Bryer [40] which identified the vortex breakdown over a slender delta wing of $\Lambda=65^\circ$ as shown in Figure 2.6. Wentz and Kohlman [41] presented a parametric study over delta wings to investigate the effects of sweep angle (ranging from 45° to 85°) and angle of attack on vortex breakdown progression at Reynolds Number about 1×10^6 . In his water tunnel experiments for sweep angles ranging between $\Lambda=60^\circ$ and 80° , Erickson [10] had shown that the vortex breakdown location observations were in good agreement with wind tunnel and real flight observations.

Non-slender delta wings differ from slender ones when the vortex breakdown is considered, in terms of occurrence geometry, they tend to exhibit more conical shape of breakdown whereas no reversed axial velocity or swirling in the core is observed [22, 31]. Identification of vortex breakdown on non-slender delta wings experimentally or numerically requires advanced techniques. Spectrum of vortex breakdown over slender delta wings extends distinct peak points whereas non-slender delta wings present an extensive band of frequency spectrum. Gursul et al. [1], compared the experimental study of Yaniktepe and Rockwell [22] with the numerical study of Gordnier and Visbal [20] identifying the three different stages of vortex breakdown namely: small scale bubbles, pinch off region, large scale breakdown.

An early investigation in the field by Lawson [42] showed that the vortex breakdown location over a stationary slender delta wing is not fixed instead it is fluctuating along the streamwise direction. More recent investigations [19, 21], for

non-slender delta wings exhibited similar fluctuations over the 40-50 percent of the chord length while this interval was 10 percent for slender delta wings [42]. Gursul [6] and Yavuz [43] implied that these fluctuations of vortex breakdown location are among the sources of wing buffeting that are significant for control and stability issues.

2.1.3 Flow Reattachment

Flow reattachment is among the characteristic features of non-slender delta wings [1] that can simply be explained as the attachment of separated shear layers from leading edges to the wing surface through the wing symmetry plane. When the slender delta wings are considered reattachment does not take place beyond the small attack angles [3] which is difficult to control. Unlike the slender delta wings non-slender ones are more prone to exhibit this structure over a wide interval. Honkan and Andreopoulos [44] conducted an experimental study for a $\Lambda=45^\circ$ sweep delta wing to identify the flow structure using spatio-temporal measurement techniques. They showed that the reattachment region and secondary vortices are related with high turbulence intensity, besides they noticed that the vorticity near the reattachment region experiences high levels of fluctuations. Taylor and Gursul [31] studied the progression of reattachment for a 50° sweep delta wing in a detailed manner showing that as the attack angle increases, primary reattachment line shifts through the wing inboard and when it reaches the centerline, complete stall is about to take place, where the reattachment becomes impossible. They also noted that the occurrence of high velocity fluctuations along the reattachment line, which is in line with the conclusions of Honkan and Adreopoulos [44]. Taylor and Gursul suggested that the unsteadiness due to above mentioned fluctuations along the reattachment region is one of the sources of wing buffeting [31]. Figure 2.7 shows the inboard movement of the reattachment line [31].

After 1980's surface flow topology gained significance in aerodynamics field. In the study of Peake and Tobak [45], three dimensional separation and reattachment were interrelated with continuous vector field approach using the fundamental

laws of topology in order to constitute flow fundamentals with singular points concept: nodes, spiral nodes and saddles.

Gursul et al. [3] plotted the behavior of vortex breakdown and flow reattachment as a function of both attack angle and wing sweep angle from various studies denoting the stall onsets, that is given in Figure 2.8. The reattachment formation over non-slender delta wings could be promoted in the post stall region by means of flow control techniques, for which it is expected to obtain enhancement in lift therefore the delay in stall.

2.2 Delta Wing Flow Control Techniques

This part aims to address important studies in the field together with the critical approaches and concluding remarks rather than giving a deep review. In order to obtain desired flight performance and stable aerodynamic capabilities for aero vehicles, relevant flow field should be investigated in detail and controlled in a strategic manner. At that point, in his review paper Gad-El-Hak [46] defined the flow control term for various applications as the ability to manage the flow field of interest in an active or passive way to employ a desired change. When the delta wings are the case, flow control strategies rely on manipulation of flow separation, separated shear layer, vortex formation, flow reattachment and vortex breakdown [3], for which the expected outcomes are increase in lift, minimization of unsteady loading therefore the delay in stall. More specifically, for slender delta wings, aim is the control and prevention of vortex breakdown while it becomes control and promotion of flow reattachment for non-slender delta wings. As stated in above definition flow control actions can be investigated in two branches: passive and active flow control techniques. Major distinction between them is the energy requirement. Passive flow control techniques do not require any energy input and generally depend on shape modifications and/ or utilization of additional control surfaces for delta wings. Active flow control technique require energy input for control action using the applications including, pneumatic methods like blowing and suction, unsteady excitation methods like small and large amplitude perturbations, mechanical systems like controllable flaps, variable

sweep wing. It is seen that there exist a considerable potential in flow control techniques in order to broaden the boundaries of MAV, UAV and UCAV at low Reynolds number flights. After giving some introductory remarks about flow control concept, fundamental and recent approaches from literature are to be given under the following subtitles.

2.2.1 Passive Control

Passive control methods are regarded as simple, less expensive techniques among aerodynamicists, however unlike their advantages they may be resulted with unexpected disturbances.

Vardaki et al. [47] proposed the utilization of flexible wings as a potential passive control method for non-slender delta wings indicating that a flexible design could enhance lift in post stall region by promoting flow reattachment thanks to their oscillating nature. Taylor et al. [48] investigated the effect of wing flexibility on lift for wings with sweep angle $\Lambda=40^\circ-60^\circ$. They obtained the greatest improvement in lift for the lowest sweep angle of $\Lambda=40^\circ$ compared to rigid wings having same dimensions which is represented in Figure 2.9. Considerable increase in lift in the amount of 50% and 7 degree delay in stall attack angle could be achieved in the post stall region for $\Lambda=40^\circ$, however there was almost no enhancement for $\Lambda=60^\circ$ sweep delta wing which may evidence that the responsible mechanisms for control of flow over non-slender and slender delta wings are different. Yang et al. [49] conducted a similar study over delta wings of sweep angle ranging between $\Lambda=25^\circ-65^\circ$ and they obtained results analogous to Vardaki et al. and Taylor et al.

Modifying the edge geometry is among the passive control methodologies encountered. Such an attempt may remarkably effect three dimensional separation and reattachment thus the flow topology over a non-slender delta wing as concluded from findings of Goruney and Rockwell [50] over delta wings with sinusoidal leading edge geometries of various wavelength and amplitudes. Chen et al. [51], Chen and Wang [52] proposed similar studies, both concluding that utilization of sinusoidal leading edge profile came out as an unusual way to delay

stall. In their novel study Çelik and Yavuz [53] qualitatively studied the effect of leading edge and trailing edge geometry modifications inspired from the nature by comparison with a $\Lambda=45^\circ$ swept delta wing.

One of the widely investigated methodologies in literature is the design of delta wings having stationary flap extensions. Klute et al. [54] conducted experiments on a slender delta wing with drooping apex flap which was an effective way to delay vortex breakdown. There are numerous studies analysing the contribution of leading edge vortex flaps that constitutes additional control surfaces. It directly effects the strength, structure of the leading edge vortices and lift-to-drag ratio especially for slender delta wings [55]. Lamar and Campbell [56], Spedding et al. [57], and Deng and Gursul [58] were among the researchers worked on the effect of leading edge vortex flaps.

Another methodology so called bleeding is recently suggested that utilizes the pressure difference between the pressure and suction sides across the slots opened close to the wingtip as explained by Hu et al [59]. It is claimed that the bleed of air through these slots would be promising without any negative effect. Although it has not been applied to delta wings yet, there are some other applications, Kearney and Glezer [60] examined effect of bleeding on airfoils lift performance while Jin et al. [61] investigated for finite aspect ratio wings.

2.2.2 Active Control

Compared to the passive control techniques, active flow control can be employed in various ways. Gad-El-Hak [46] reviewed active control techniques under two sub-branches: predetermined and reactive. Predetermined control consists of steady or unsteady energy input regardless the current state of the flow with no sensing action, while reactive control is a particular sub-branch at which the control input is progressively adapted depending on sensor signals of some kind. Figure 2.10 shows different control loops of active flow control [46]. There are numerous studies in the literature applied to the delta wings for both experimental cases and real practices. After diverse fundamental approaches in active flow

control techniques were implemented, it has become significant to design and propose energy efficient and applicable methods.

As a pneumatic technique, control by suction and blowing has been widely performed for the control of leading edge vortices, in various configurations such as: leading edge suction/ blowing, trailing edge blowing and along core suction/blowing [3]. Application of these methods could be conducted in steady and unsteady (periodic) ways. There is a well-documented knowledge on steady applications. Unsteady forcing, which is the technique used in this study is to be reviewed under the following separate sub-title. As in other approaches over delta wing, major attention initially had been given to slender delta wings for pneumatic techniques. Wood et al. [62] applied steady blowing along the leading edges of a $\Lambda=60^\circ$ sweep delta wing. They obtained the controllability of vortex structure even at high attack angles up to 50° . McCormick and Gursul [63] studied the effect of steady suction near the separation points of a $\Lambda=70^\circ$ sweep delta wing showing that small amount of suction could adjust the location of vortex core and move downstream the breakdown. Helin and Watry [64] employed the steady trailing edge blowing technique to a $\Lambda=60^\circ$ sweep delta wing showing that the onset of vortex breakdown location changed with the jet velocity and the adverse pressure gradient was considerably effected. Shih and Ding [65] studied this technique both for static and dynamic (pitching up) wings while Phillips et al [66] investigated the effect of technique together with a fin mounted on the wing. Guillot et al. [67] and Mitchell et al. [68] showed that the along core blowing is an effective technique thus accelerates the axial core flow and considerably adjusts the pressure gradient. Gursul et al. [3] compared the effectiveness of these techniques in terms of the change in the vortex breakdown location on the wing chord under applied momentum coefficient for which the along the core blowing is found to be the most effective one as shown in Figure 2.11.

There have been relatively few attempts for the control of non-slender delta wings using the pneumatic methods. Wang et al. [69] applied the trailing edge blowing to both non-slender and slender delta wings with sweep angles of $\Lambda=50^\circ$ and $\Lambda=65^\circ$ respectively, concluding that it gets difficult to postpone the onset of

vortex breakdown on non-slender delta wings due to earlier occurrence. Yavuz and Rockwell [70, 71] characterized the near surface flow topology and structure in crossflow planes for a $\Lambda=35^\circ$ sweep delta wing which is subjected to steady trailing edge blowing. Zharfa et al. [34] employed steady blowing through the leading edges of a $\Lambda=35^\circ$ delta wing which was an effective way to prevent the occurrence of three dimensional separations from the surface. There is an increasing interest in the control of non-slender wings in recent years and it is expected to see the utilization of them in a broad range of operation.

There are some other studies other than the predetermined techniques for active control of delta wings. Gursul et al. [72] proposed a feedback closed loop control system for a high sweep delta wing that measured pressure fluctuations, identified the vortex breakdown and changed the sweep angle. Liu et al. [73] designed a reactive control system that employed along core blowing and showed that such closed loop systems could significantly adjust the surface pressure distribution and prevent the vortex breakdown.

2.2.2.1 Unsteady Forcing

Being the inspiration point, unsteady forcing techniques of various kinds can be related with the current study. Unsteady is not the only corresponding term. The terms of periodic, transient and oscillating have also been used depending upon the method. Oscillating wings, oscillating leading edge flaps, acoustic excitations, periodic blowing and suction using pneumatic methods are widely used ones. Such techniques are generally linked to the naturally occurring unsteady phenomenon on delta wing flows in terms of the frequencies of instabilities. However this approach is much more acceptable for slender wings due to the recorded spectral peaks.

Deng and Gursul [74] showed that oscillating leading edge flaps modified the strength of vortices emanates from a high swept wing. Yang and Gursul [75] investigated how harmonic variations of sweep angle effected the vortex breakdown. For slender delta wings beside mechanical systems, pneumatic techniques have been widely utilized. Gad-el-Hak and Blackwelder [76], Gu et

al. [77], Guy et al. [78], and Guy et al. [79], experimentally studied the effect of periodic blowing and suction through the leading edges of slender delta wings. Common outputs of these studies were the significant delay of the vortex breakdown and stall where the lift could be improved. Morton et al. [80] numerically investigated the case for which there was a good agreement with the experimental studies. Mitchell and Delery [81] provided a deep review for these methods. Margalit et al. [82] applied a wide range of excitations to a $\Lambda=60^\circ$ sweep delta wing, inspiring the effective frequencies and momentum coefficients from the just above mentioned references using zero-net mass flux piezoelectric actuators to propose the energy efficient waveforms. Kölzsch and Breitsamter [83] were able to shift the breakdown location downstream and boost the vortex flow through the trailing edge by applying the pulsatile leading edge blowing using fast switching solenoid valves. Unsteady trailing edge blowing was first applied by Jiang et al. [84] to both slender and non-slender delta wings investigating dynamic response of breakdown and normal force coefficient. It was shown by Kuo and Lu [85] that along core blowing applied in transient manner was an effective way to adjust pressure gradient and to delay breakdown.

There is an increasing trend in unsteady applications when non-slender wings are considered for which the flow reattachment is the critical parameter to be controlled as it was mentioned earlier. Vardaki et al. [86] studied small amplitude roll oscillations applied to non-slender delta wings with sweep angles ranging from 30° to 50° . They reported not only the effect of the sweep angle but also the excitation frequency, mode and amplitude. They were able to considerably promote flow reattachment in post-stall conditions for which the vortex core started to reform from the wing tip and breakdown came next. The reported optimum dimensionless excitation frequency, Strouhal number ($f.C/U_\infty$) range $St=1-2$ was found to be generic for all sweep angles. Williams et al. [87] conducted pressure measurement and PIV experiments to report how the unsteady blowing modifies the leading vortices of a $\Lambda=50^\circ$ sweep delta wing. In their parametrical study, effects of momentum coefficient, excitation frequency, blowing slot configurations and attack angle were documented. It was noticed that

as the attack angle increases the optimum momentum coefficient increases. PIV experiments in cross flow and surface planes evidenced that the flow reattachment was promoted with forcing. Figure 2.12 shows the fully stalled no control case together with the reattached, forced case at a high attack angle of 30° [87].

Considering the scope of this study, literature survey is not limited to delta wings. Unsteady blowing applications on airfoils [88-90] have been also reviewed in terms of experimental set-up, excitation capabilities and calibration procedures which are discussed in the next chapter.

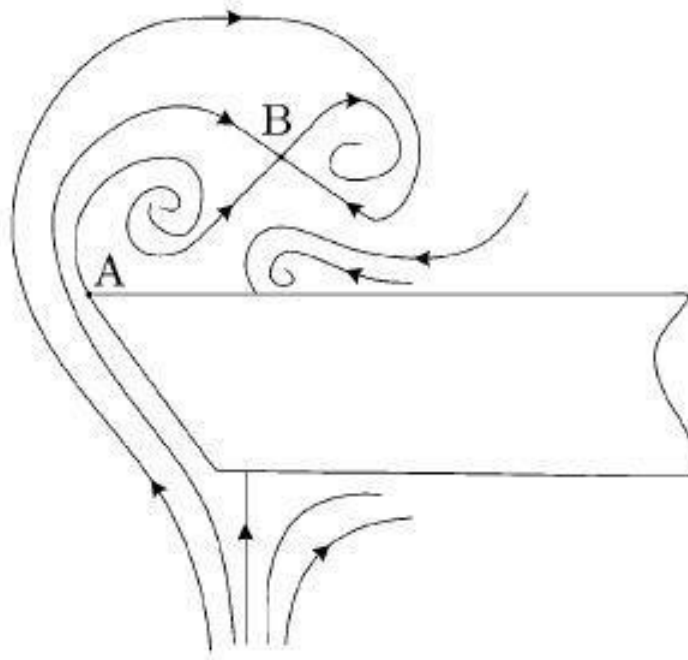


Figure 2.1 Sketch of dual vortex formation [23].

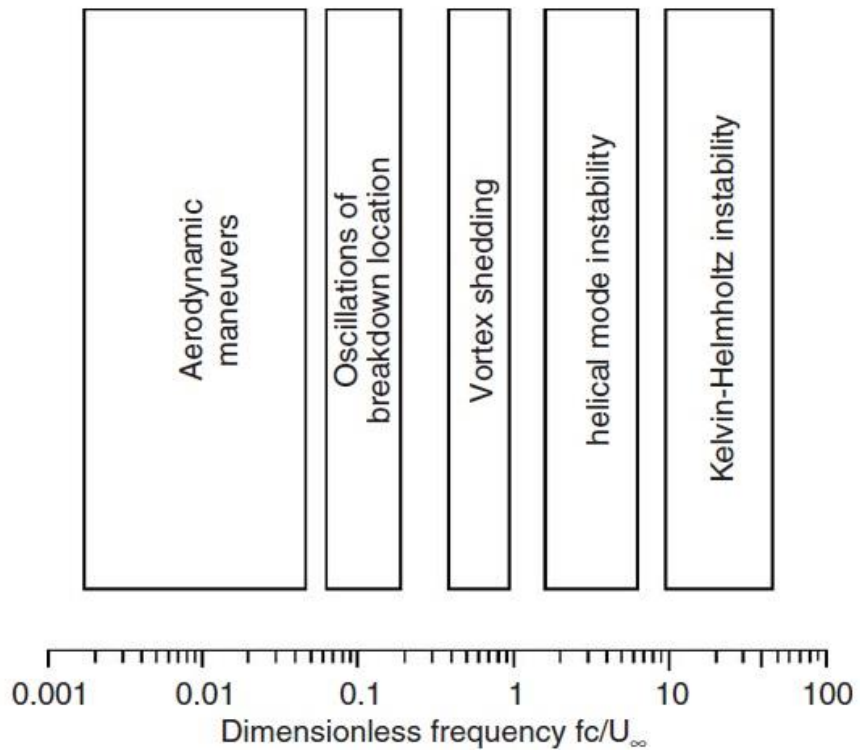


Figure 2.2 Spectrum of unsteady flow phenomena over delta wings [6].

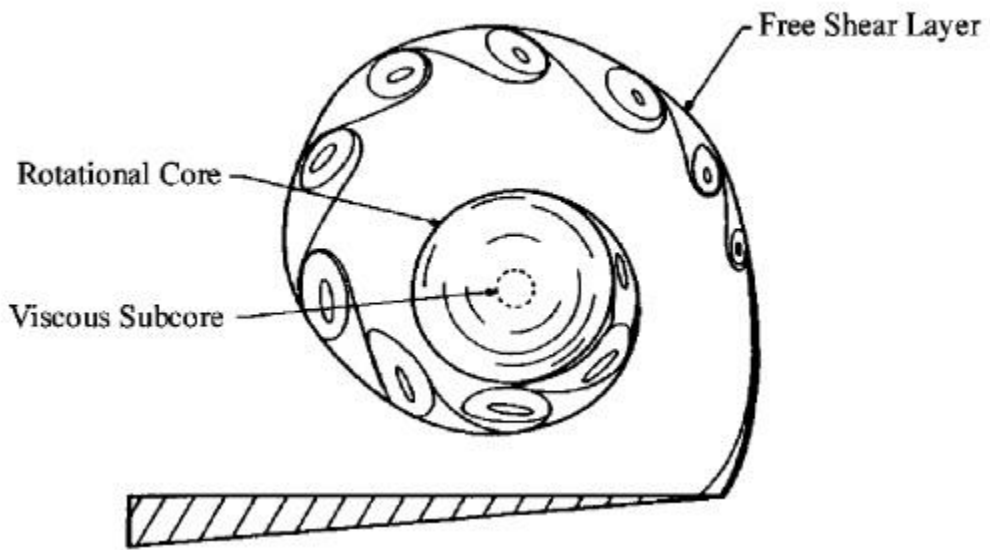


Figure 2.3 Illustration of free shear layer, rotational core and viscous subcore over a delta wing [30].

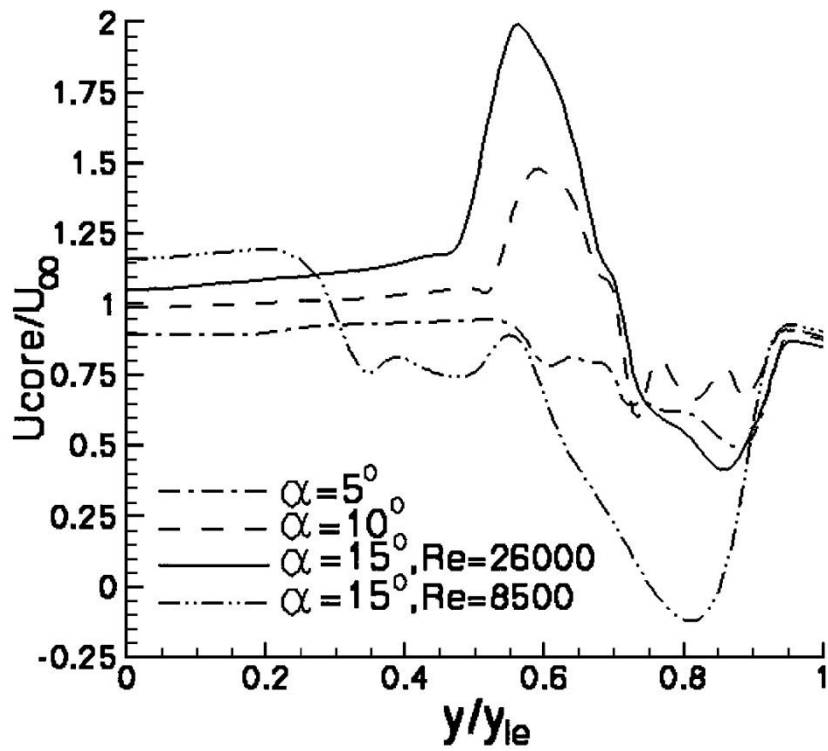


Figure 2.4 Mean axial velocity profile through the vortex core [20].

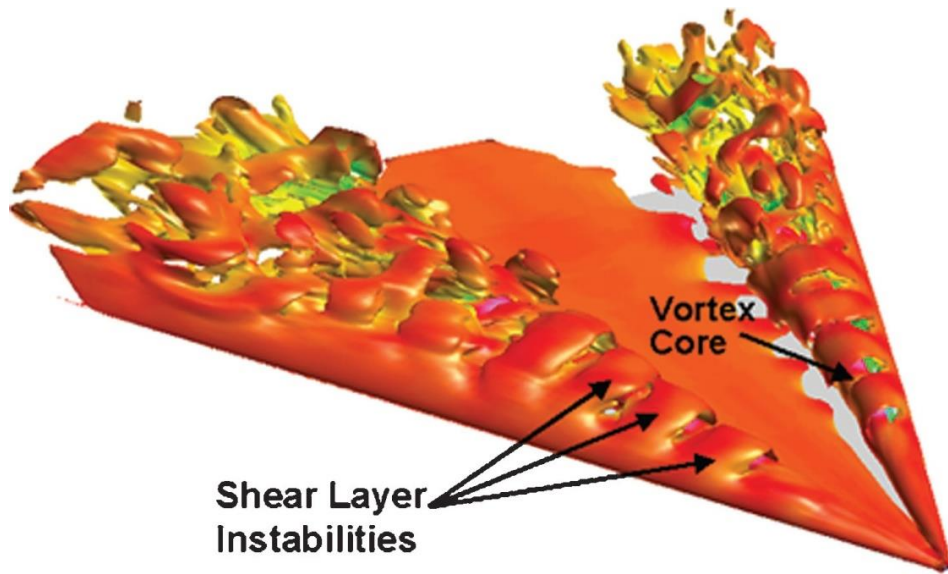


Figure 2.5 Instantaneous vortex structure over a delta wing [20].

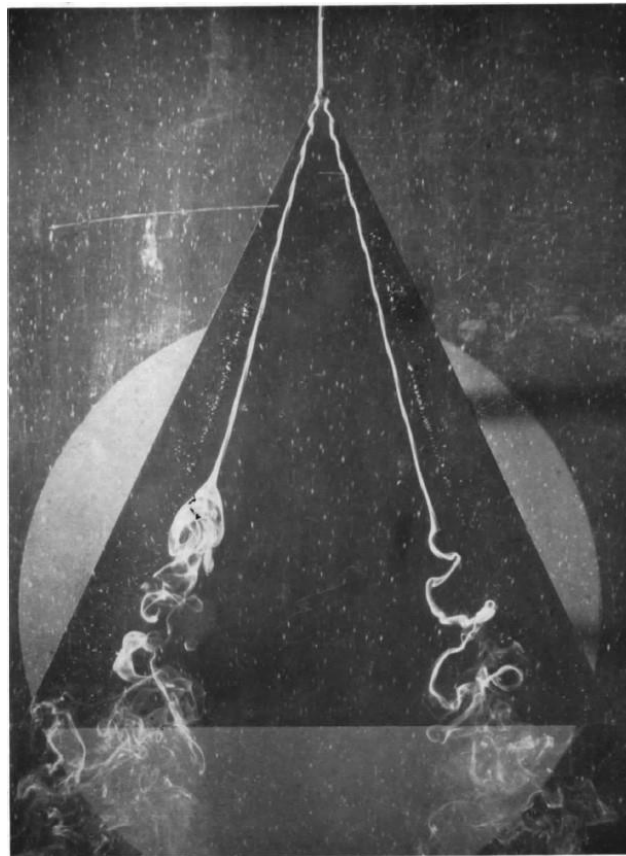


Figure 2.6 Vortex breakdown visualization [40].

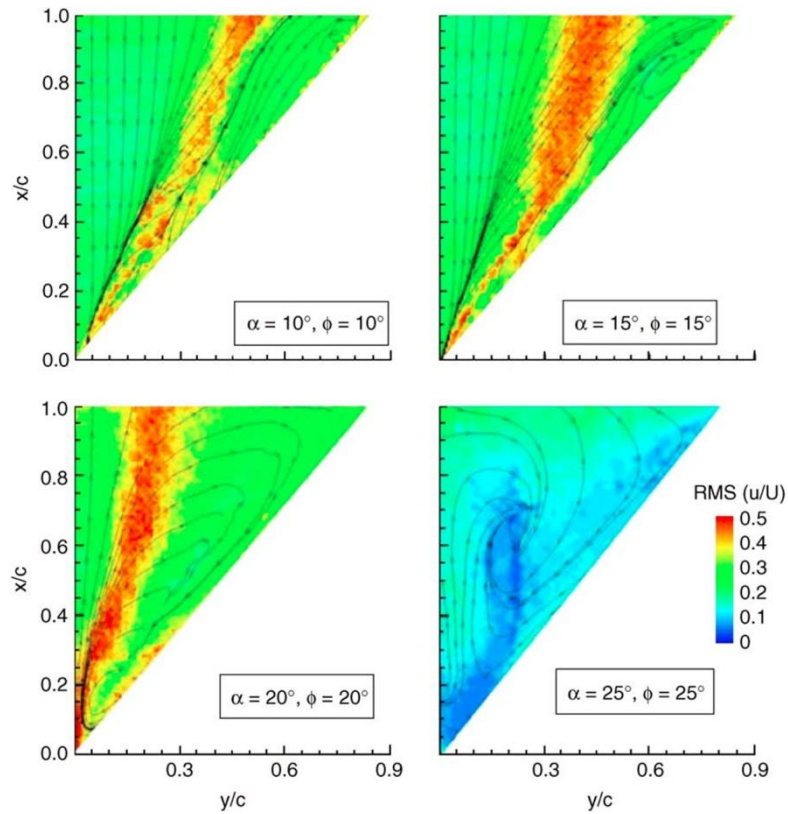


Figure 2.7 Magnitude of time-averaged velocity and streamline pattern near the wing surface in water-tunnel experiments.breakdown visualization [31].

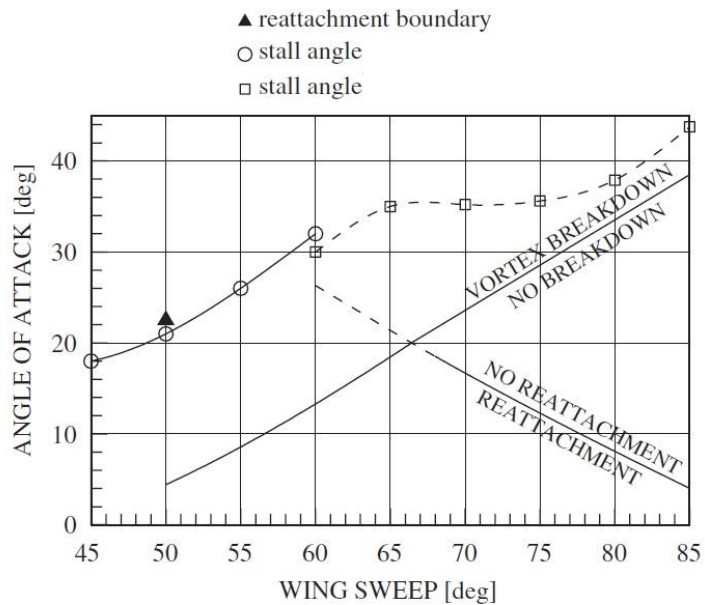


Figure 2.8 Boundaries of vortex breakdown and flow reattachment as a function of angle of attack and sweep angle [3].

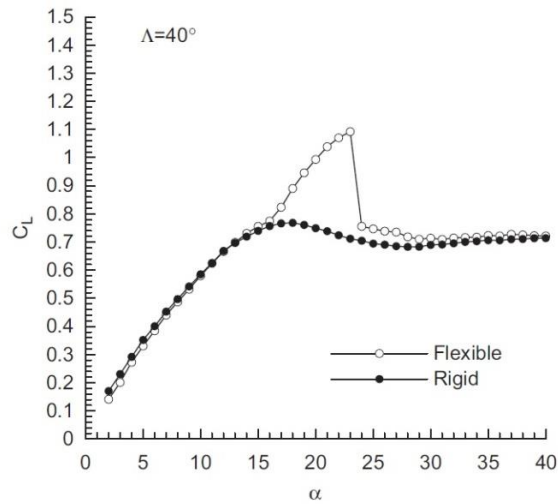


Figure 2.9 Variation of the time-averaged lift coefficient for a flexible delta wing [48].

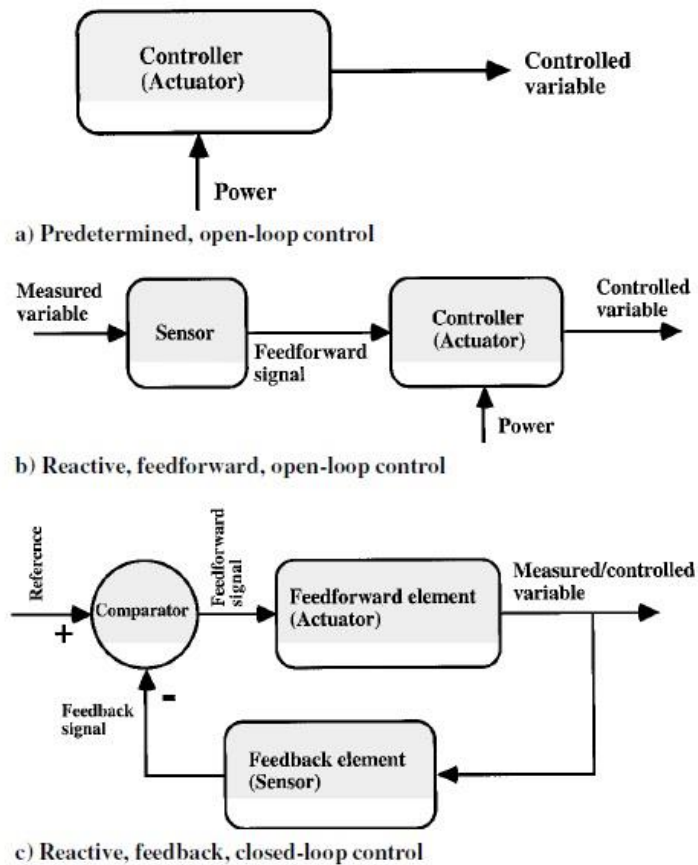


Figure 2.10 Different control loops for active flow control [46].

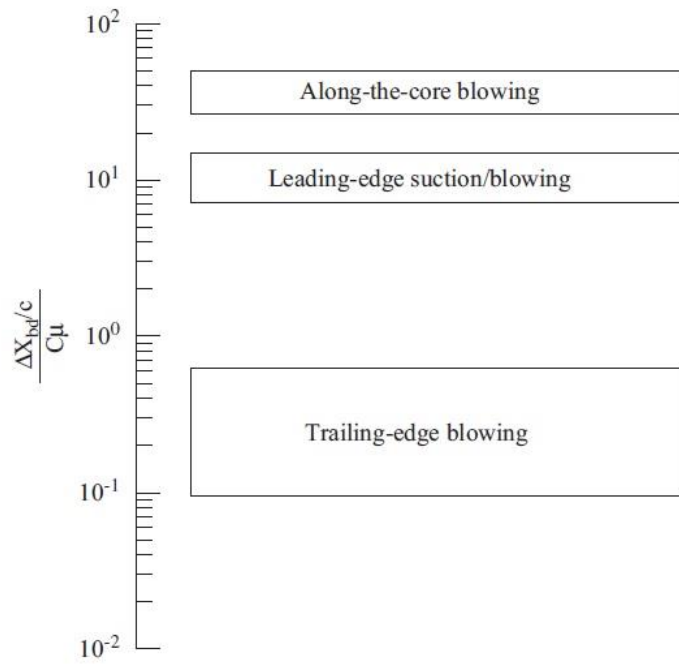


Figure 2.11 Optimum effectiveness of various blowing/suction techniques [3].

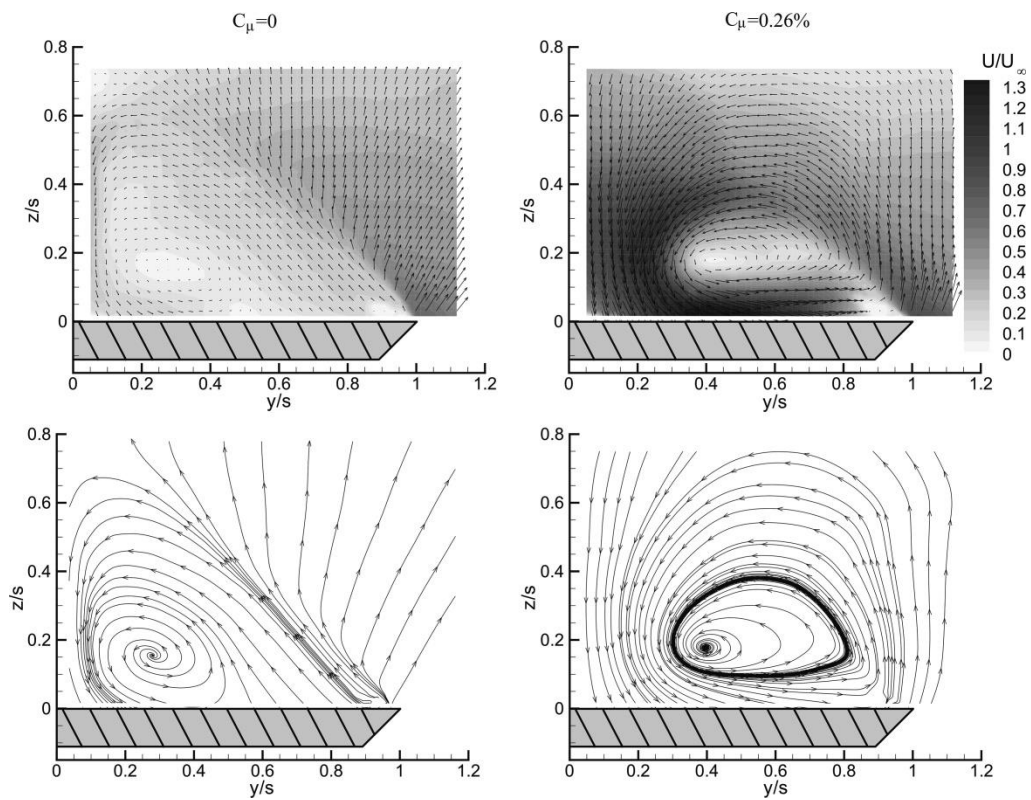


Figure 2.12 Cross flow PIV measurements for unsteady blowing [87].

CHAPTER 3

EXPERIMENTAL SET-UP AND TECHNIQUES

3.1 Wind Tunnel Facility

This experimental study was conducted in a low speed, suction type, open circuit wind tunnel facility located at the Fluid Mechanics Laboratory of Mechanical Engineering Department at Middle East Technical University. The tunnel is built on five main parts namely settling chamber, contraction cone, test section, diffuser and fan. The tunnel facility is shown in Figure 3.1.

Air is allowed through the tunnel from two symmetrical inlet sections located at the sides of the tunnel. In order to prevent any foreign object entrance and to increase the uniformity of air, fine-mesh screens are mounted at both inlets. The length of the settling chamber, also called as entrance section, is 2700 mm. A honeycomb and additional three fine-mesh screens are installed along this section to keep turbulence intensity at low levels and to increase uniformity of the airflow in the test section. The contraction cone has the ratio of 8:1 and the length of 2000 mm.

The test section, which is fully transparent, has dimensions of 750 mm width, 510 mm height and 2000 mm length. The maximum free stream velocity that can be obtained in the test section is 30 m/s.

The diffuser decelerates the high-speed flow leaving from the test section, thereby achieving static pressure recovery and reducing the load required to drive the system. The cross sectional area of the 7300 mm long diffuser gradually decreases along its axis, with 3° divergence angle so as to prevent flow separation.

An axial fan and a 10kW AC motor assembly are mounted at the exit of the tunnel

with a remote frequency control unit to run the tunnel at desired velocities.

The tests were conducted at a free stream velocity of 3.5 m/s that corresponds to a Reynolds number of 35000 based on the wing chord length, which is calculated as shown in Equation 3.1.

$$Re = \frac{U_{\infty} C}{\nu} \quad (3.1)$$

3.1.1 Wind Tunnel Characterization

In order to reach the required velocities in the test section, the wind tunnel was characterized prior to the experiments. The system was operated at a wide range of fan powers and velocity measurements were taken at a certain point in the test section both by direct and indirect methods for comparison purposes. As a direct method Laser Doppler Anemometry (LDA) technique was used while Pitot-Static probe connected to pressure scanner was used for indirect measurement. For the calculation of the velocity from Pitot-Static probe dynamic pressure measurements; current temperature, humidity and elevation conditions of the laboratory were taken into account. Average velocity was plotted against tunnel power as shown in Figure 3.2 for which turbulence intensity values were also given. It is seen that there exists almost a linear behavior for the fan power greater than 4%. The maximum turbulence intensity obtained in the test section was 0.9%. In addition, the difference in velocity values taken from both measurement techniques was found to be around 3 %.

3.2 Delta Wing Model

A sharp-edged delta wing model with a sweep angle of $\Lambda=45^{\circ}$ was used in the experiments. The wing was made of fine polyamide PA2200 and manufactured using rapid-prototyping machine located in the METU BİLTİR Center. The chord, span and thickness of the wing were 150 mm, 300 mm and 15 mm respectively. The leading edges of the wing were beveled on the windward side at an angle of 45° . Figure 3.3 illustrates the two dimensional sketches of the wing model from plan and back views.

The wing was designed such that it has pressure measurement holes on the surface, smoke injection holes at the tip and blowing holes at the leading edges whose accesses were from the trailing edge. The dimensions of the wing were determined considering the test section dimensions therefore the blockage ratio. The maximum blockage ratio at the highest attack angle of $\alpha=20^\circ$ was 2%. The wing model had 54 pressure taps which were symmetrically distributed over three stations located at chordwise distances of $x/C=0.32$, 0.56 and 0.80 respectively. Taking the limitations of the production processes into consideration, the total number and the locations of the pressure taps were determined in order to obtain high measurement resolution during the experiments. The diameter of the pressure taps was 0.5 mm in order to minimize the effect of tap diameter on pressure measurement. A total of six blowing holes, three in each half of the wing, with a diameter of 2 mm each were located 1 mm inboard of the leading edges. The blowing holes were positioned at the chordwise distances of $x/C=0.16$, 0.44 and 0.68 corresponding to 35, 97 and 150 mm distances away from the apex of the planform, respectively. The blowing holes were parallel to the bevel surfaces so that the air leaves the hole with a jet angle of 45° from the wing surface. The 3D solid model and the actual pictures of the wing are shown in Figures 3.4 and 3.5, respectively. The sketch of the wing, the mount and the test section assembly are illustrated in Figure 3.6.

3.3 Flow Control Set-up

The unsteady blowing setup was installed in order to supply the pulsed air through the leading edges of the wing model. The schematic representation of the setup is shown in Figure 3.7. The pulsed blowing generation was initially tried to be obtained using a REXROTH ED02 series 3/3 pressure regulator valve that was available in the laboratory. However as a result of the inaccurate switching capability, desired frequencies and valve closing actions could not be achieved. ED02 was replaced with a FESTO MHJ9-QS-4-MF Fast Switching Solenoid Valve and a MHJ9-KMH control module, which are shown in Figure 3.8. The valve function is defined as 2/2 way, single solenoid-closed by the producer. The

operating voltage range was 12-53 Volts and the control voltage range was 3-30 Volts. The valve could properly function under the supply pressures from +0.5 to +6 bar. The switch on and off times of the valve were 0.9 and 0.4 micro-seconds respectively, so this pneumatic system was able to transmit the digital signal in the form of a square wave at a high level of repeatability.

The valve control signal was generated by the LabVIEW virtual instruments that output the desired waveform to the valve control module using a National Instrument NI-9263 analogue output card. LabVIEW is capable of generating sine, square, triangle, sawtooth wave signals for which one can specify the frequency, phase, amplitude, offset, samples per second, number of samples, and number of duty cycles. The block diagram for the control set-up is shown in Figure 3.9. NI-9263 analogue data acquisition card had output control signal range of ± 10 V with 16 bit resolution. It had 4 simultaneous channels in total each having an analogue output terminal AO and a common terminal COM [91]. Built in channel digital-to-analog converter (DAC) provided simultaneous analogue output signal to the valve system. Figure 3.10 shows the NI-9263 module and its circuitry. The operating voltage required by the valve system was supplied using an external DC power supply.

The pressurized air for the valve was supplied from the main compressed air line of Fluid Mechanics Laboratory. Prior to the valve, the compressed air was filtered and the pressure was regulated to 6 bars. The flow rate of the air was manually controlled using a rotameter located just after the pressure regulator and filter. The exit of the valve was connected to the wing model using the pneumatic tubing and fittings. The valve system was positioned as close as possible to the wing model and the tubing was kept as short as possible.

In order to make sure the injected pattern, the velocity distribution at the blowing holes was measured using Hot Wire Anemometry (HWA) prior to the experiments conducted. First, the flow meter was adjusted to an initial position, then the velocity pattern was started to be recorded and the flow meter was continuously adapted until the desired momentum coefficient was obtained, calculated using hot wire data.

3.3.1 Blowing Scenario

In this study blowing scenario depends on the parameters including excitation pattern, excitation frequency, duty cycle, and the momentum coefficient. The excitation pattern was in the form of a square wave with a duty cycle of 25 % and the excitation frequencies varied from 2 Hz to 24 Hz.

The unsteady blowing cases are characterized by the dimensionless momentum coefficient, which is generally defined as the ratio of the momentum of the applied control to the free stream momentum on the wing. In other words, it expresses the amount of energy added to the flow field. In the literature momentum coefficient for unsteady blowing and/or suction techniques was calculated with different approaches like using the root mean square of the jet velocity or time averaged value of the jet velocity. Such methods are generally preferred for waveforms like sine and triangle. These waveforms do not exhibit any sharp state change as in square wave. There is no widely accepted methodology for the momentum coefficient calculation of square waves. For the comparison purposes, in the current study, two different numbers have been assigned and used namely; maximum momentum coefficient, $C_{\mu,max}$ and effective momentum coefficient, $C_{\mu,eff}$. They are calculated as follows;

$$C_{\mu,max} = \frac{Q_j \bar{U}_j}{U_\infty^2 A_s} \quad (3.2)$$

where, \bar{U}_j is the mean of the velocities when the valve is at open state, Q_j is the mean flow rate when the valve is at open state, U_∞ is the free stream velocity and A_s is the surface area of the planform.

$$C_{\mu,eff} = DC \cdot C_{\mu,max} \quad (3.3)$$

The effective momentum coefficient is found by multiplication of maximum momentum coefficient with duty cycle, DC. Preliminary tests have been conducted to determine the momentum coefficients to be tested in the experiments. $C_{\mu,max}=0.01$ and thus, $C_{\mu,eff}=0.0025$ were applied for all excitation frequencies. The effective momentum coefficient $C_{\mu,eff}$ represents the amount of

cumulative momentum added to the flow, whereas $C_{\mu,max}$ shows the momentum added the system as if the valve operates at 100 % DC as in steady blowing condition. The steady blowing cases with $C_{\mu}=0.01$ and 0.0025 were also applied for comparison purposes.

The experiments were performed at four different attack angles; $\alpha=7^\circ$, 13° , 16° and 20° for above told blowing conditions. Figure 3.11 shows the experimental matrix of the current study.

3.3.2 Unsteady Blowing Measurements via Hot Wire Anemometry

The hot wire anemometry technique has been used for many years in order to measure the fluid velocity. In spite of the availability of non-intrusive velocity measurement systems like LDA and PIV, it is still widely applied, due to its continuous data sampling ability at high frequency rates. The hot wire anemometer also still remains as the unique technique that outputs a truly analogue representation of the fluid velocity.

The basic operation principle is based on sensing the changes in heat transfer from a small, electrically heated wire exposed to the fluid motion. Heat transfer takes place in the mode of convection which is the function of the fluid velocity for which the radiative heat transfer is assumed to be negligible. Thus a relationship between the fluid velocity and the electrical output can be established.

In this study Dantec DISA 56C01 Constant Temperature Anemometry (CTA) main unit and 56C17 bridge were used together with a Dantec type 55P16 hot wire probe. The CTA Bridge whose circuit diagram shown in Figure 3.12 keeps the resistance and hence the temperature of the wire constant by controlling the current using a servo amplifier. The bridge voltage represents the heat transfer and it is a direct measure of the fluid velocity. The CTA unit is shown in Figure 3.13. The hot wire probe used for unsteady blowing measurements was a general purpose type platinum plated tungsten miniature wire probe, 55P16 which had $5\ \mu\text{m}$ wire diameter and $1.25\ \text{mm}$ active sensor length. The probe was cable-equipped one with a straight support and a BNC connector as illustrated in

Figure 3.14. A 12-bit National Instrument PCI-6024E DAQ card connected to the main board of a desktop computer was used to acquire and digitize the analog voltage signal from CTA bridge. Samples were recorded using LabVIEW SignalExpress software at a 2 kHz sampling frequency for 4 seconds. Figure 3.15 shows the schematic representation of the measurement chain. Hot-wire probe was calibrated by means of a Dantec 54H10 calibration unit that belongs to METU Aerospace Engineering Department. It is a robust device that provides a free jet for easy access with probe. The probe signal linearization was achieved using the spreadsheet provided in the manual of the calibration unit. The calibration curve and data are given in Figure 3.16.

For the characterization and calibration of the unsteady blowing, the wing model was positioned in the wind tunnel at zero attack angle. The unsteady blowing jet leaves the leading edge of the wing model being parallel to the bevel surface. The hot wire probe was positioned facing the center of jet in perpendicular orientation 2 mm away from the leading edge using the custom designed platform shown in Figure 3.17. The position of the platform was ensured using the graph paper.

3.4 Pressure Measurements

Pressure measurements were carried out using a Netscanner 9116 Intelligent Pressure Scanner that integrates 16 silicon piezoresistive pressure transducers. The sensors are capable of measuring the pressure in the range of 0-2.5 kPa. This device was pre-calibrated over certain pressure and temperature spans by the supplier. The calibration settings of each transducer were stored in the EEPROM (Electrically Erasable Programmable Read-Only Memory). Due to the integrated microprocessor and the temperature sensors, the device is able to compensate the transducer outputs for offset, nonlinearity, sensitivity and thermal effects prior to transferring data to the computer. Therefore the system ensures a measurement resolution of $\pm 0.003\%$ FS (full scale).

The wing model had 54 pressure tabs in total. A couple of measurements were taken to check whether a complete symmetrical pattern could be obtained or not. Once a complete symmetrical pattern was observed, the rest of the experiments

were performed at the half side of the wing for which three sets of measurements were taken at the second station $x/C=0.56$ for all cases. The data was recorded at a 500 Hz sampling rate for 10 seconds. Pressure scanner was connected to the pressure taps on the wing via nylon tubing of 1/8" internal diameter. The pressure scanner device and wing connections are illustrated in Figure 3.18. The device was fixed on the table and the tubing was hanged over supporters in order to minimize the noise created by the environmental disturbances. Before starting the each experiment set, noise values were recorded at the same sampling rate and acquisition time, and then subtracted from corresponding actual measurements in order to handle the refined data.

Dimensionless pressure coefficients values C_p were calculated as an expression of the pressure distribution at the respective measurement station using Equation 3.4. For the corresponding pressure distribution charts the C_p values were shown as $-C_p$ that plotted against the dimensionless spanwise location of the pressure tabs. Pressure fluctuations were figure out using root mean square (RMS) calculations of pressure readings and then converted to $C_{p,RMS}$ values as calculated in Equation 3.6. $C_{p,RMS}$ values were also plotted in same manner to provide information about the unsteady behavior of the pressure distribution.

$$C_p = \frac{p - p_\infty}{\frac{1}{2}\rho U_\infty^2} = \frac{p - p_\infty}{p_{dyn}} \quad (3.4)$$

p : Measured static pressure

p_∞ : Static pressure of the flow

p_{dyn} : Dynamic pressure of the flow

ρ : Fluid Density

U_∞ : Free Stream Velocity

$$p_{RMS} = \sqrt{\frac{\sum_{i=1}^N (p_i - \bar{p})^2}{N}} \quad (3.5)$$

N : Number of samples

\bar{p} : Time averaged static pressure value

$$C_{p,RMS} = \frac{p_{RMS}}{p_{dyn}} \quad (3.6)$$

Considering the unsteady control applied in this study, it would become critical to ensure whether the pressure scanner device was capable of measuring unsteady pressure values. For that purpose Fast Fourier Transform was applied on pressure data. It was seen that the excitation frequencies could be observed from pressure data. The corresponding spectral analyses were plotted in the next chapter.

3.5 Particle Image Velocimetry (PIV) Measurements

In order to obtain a better insight through the flow structure, Particle Image Velocimetry (PIV) experiments were conducted for the selected cases based on the results of the pressure measurements. PIV provides a global characterization of the flow field. It is a non-intrusive technique that gives a series of instantaneous velocity fields over the area of interest.

In the current study a TSI 2D PIV system was used for the velocity measurement in the cross flow plane at the dimensionless chordwise distance of $x/C=0.56$ where the surface pressure measurements were previously taken. The PIV system can generate laser pulse pairs up to 200 mJ using a Litron Nd:YAG laser for which the maximum repetition rate is 15 Hz. The PIV camera is a Powerview Plus 8-bit, digital, CMOS camera having a pixel resolution of 2048 x 2048, equipped with a Nikon 50 mm F/1.8D lens. For each of the investigated cases 200 image pairs were taken. The seeding for PIV experiments were provided with a commercial fog generator that uses glycol based fog fluid.

The sketch of the experimental set-up is shown in Figure 3.19. The laser sheet was adjusted perpendicular to the freestream at the selected location. The PIV camera was located outside the test section whose axis was also perpendicular to the vertical side of the test section. It was able to capture the field of interest reflecting from a 15 x 25 cm rectangular mirror located inside the test section at

five chord distance downstream of the wing model with an angle orientation of 45° to the freestream.

The PIV setup was controlled with Insight 4G software. The separation time (Δt) between two laser pulses was set to $100\mu s$. During the adjustment of this parameter for the cross flow measurements, the laser sheet thickness needs to be considered as well to ensure the existence of particles inside the illuminated region. The camera is operated at an aperture setting of $f\#5.6$. Post processing of the PIV measurements was performed within a region of interest of $94.9 \times 40.7 \text{ mm}^2$. The velocity vectors was obtained in an interrogation window of 16×16 pixels. The effective grid size, was 2.71 mm that yielded a total of 35×15 (525) velocity vectors.

PIV experiments were performed at an angle of attack of $\alpha=16^\circ$ and Reynolds number of 35000 for cases; no control, steady blowing with $C_{\mu}=0.0025$, $C_{\mu}=0.01$ and unsteady blowing of excitation frequencies 4 Hz, 16 Hz as shown in Figure 3.11.

3.6 Uncertainty Estimates

Any of the experimental measurements would contain some kind of uncertainty that arises from the possible inaccuracies in measurement devices and the random variations in measured quantities. Before presenting any experimental reports, validity of the result should be presented using uncertainty analysis tool.

In this topic possible sources of uncertainties accounted in momentum coefficient and pressure coefficient calculations are tried to be addressed and documented.

The following equation 3.7 is suggested for calculating the best estimate uncertainty of a result R that is a function of n number of measured variables [92].

$$\omega_R = \left[\left(\omega_{x_1} \frac{\partial R}{\partial x_1} \right)^2 + \left(\omega_{x_2} \frac{\partial R}{\partial x_2} \right)^2 + \dots + \left(\omega_{x_n} \frac{\partial R}{\partial x_n} \right)^2 \right]^{1/2} \quad (3.7)$$

Where ω_{x_i} is the uncertainty estimate of the each measured variables. Similarly fractional uncertainty in other words relative uncertainty of each result or measured variable can be found as in equation 3.8.

$$\frac{\omega_R}{R} = u_R \quad (3.8)$$

Equation 3.7 has been used to propagate the uncertainty of the pressure coefficient denoted in Equation 3.4, which is the function of static pressure p , free stream static pressure p_∞ and dynamic pressure of the flow p_{dyn} . At that point p_{dyn} is not directly measured instead it is found from the pitot static tube measurements by subtracting the p_∞ from p_{stag} . So the equation 3.8 would give the uncertainty of the pressure coefficient as

$$\omega_{C_p} = \left[\left(\omega_p \frac{\partial C_p}{\partial p} \right)^2 + \left(\omega_p \frac{\partial C_p}{\partial p_\infty} \right)^2 + \left(\omega_p \frac{\partial C_p}{\partial p_{stag}} \right)^2 \right]^{1/2} \quad (3.9)$$

ω_p value is same for all pressure values that is calculated from producer specification for pressure scanner whose measurement accuracy is 0.003 % FS. From above conclusions the relative uncertainty value is found as 2.3 % for the maximum absolute $-C_p$ value and as 13 % for the minimum one.

For the uncertainty analysis of the momentum coefficient the relative uncertainties of measured variables namely dynamic pressure, blowing hole area and wing surface area are calculated using the same equations 3.7 and 3.8. The factor taken into account for the blowing jet velocity comes from relative uncertainty of the hot wire anemometer system that is estimated as 4%. For blowing holes the resolution of a Vernier caliper and for wing surface area ruler resolution are considered. The values are listed in following table

Table 3.1 Relative uncertainties of the measured variables used in momentum coefficient calculation.

Variable	$\frac{\omega_{x_i}}{x_i}$
\bar{U}_j	0.04
p_{dyn}	0.0157
A_j	0.1225
A_s	0.0075

Relative uncertainty in any result R can be found by combining the relative uncertainties of n number of measured quantities as follows [93]:

$$u_R = \pm \left[\left(\frac{x_1}{R} \frac{\partial R}{\partial x_1} u_1 \right)^2 + \left(\frac{x_2}{R} \frac{\partial R}{\partial x_2} u_2 \right)^2 + \dots + \left(\frac{x_n}{R} \frac{\partial R}{\partial x_n} u_n \right)^2 \right]^{1/2} \quad (3.10)$$

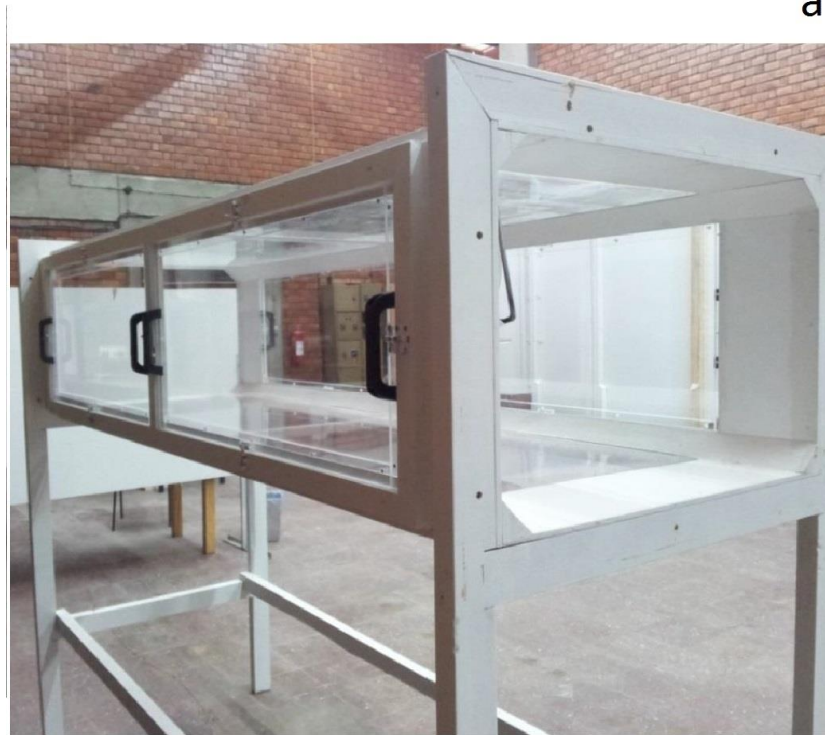
Utilization of the above equation gives:

$$u_{C_\mu} = \pm \left[\left(\frac{\bar{U}_j}{C_\mu} \frac{\partial C_\mu}{\partial \bar{U}_j} u_{\bar{U}_j} \right)^2 + \left(\frac{p_{dyn}}{C_\mu} \frac{\partial C_\mu}{\partial p_{dyn}} p_{dyn} \right)^2 + \left(\frac{A_j}{C_\mu} \frac{\partial C_\mu}{\partial A_j} u_{A_j} \right)^2 + \left(\frac{A_s}{C_\mu} \frac{\partial C_\mu}{\partial A_s} u_{A_s} \right)^2 \right]^{1/2} \quad (3.11)$$

Relative uncertainty of momentum coefficient is found to be 13.2 %. One should note that all above calculated uncertainty results are based on normal distribution of the measured data.



a



b

Figure 3.1 View from wind tunnel facility (a) and test section (b).

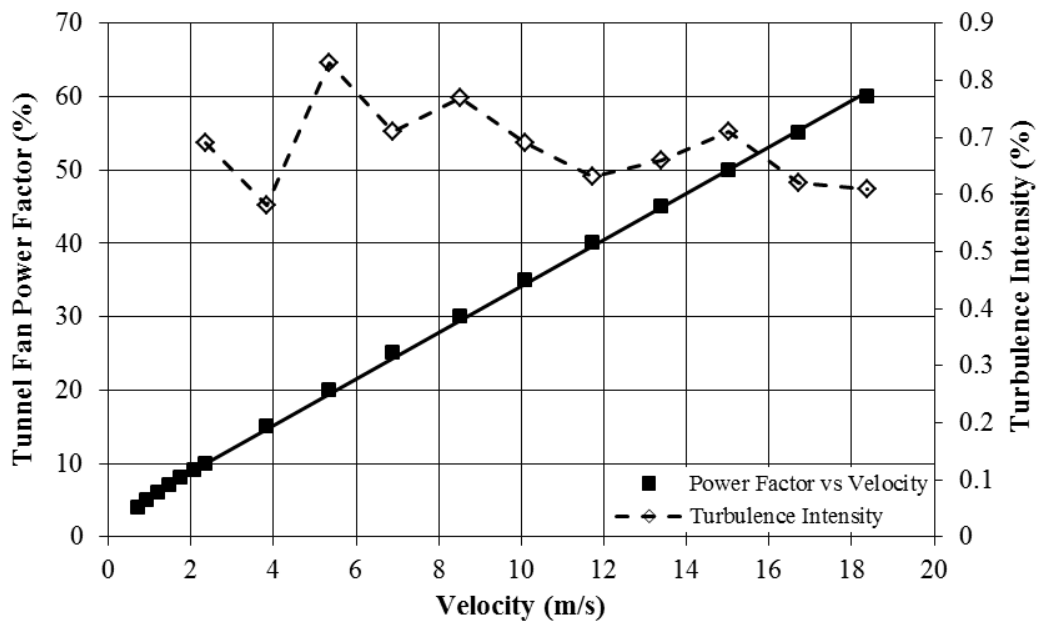


Figure 3.2 Wind tunnel calibration graph.

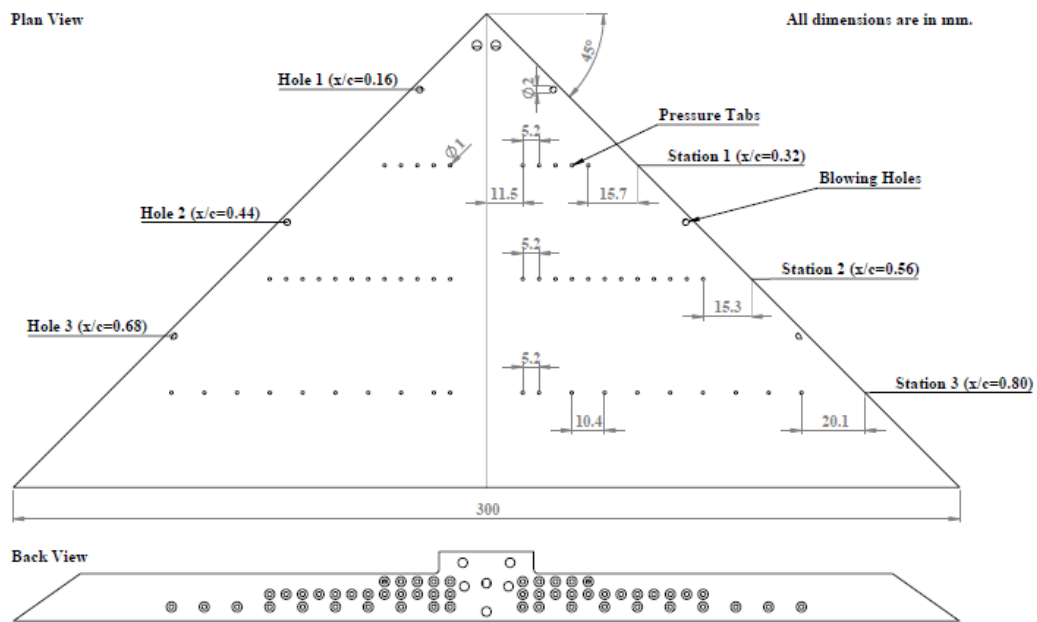


Figure 3.3 Wing model plan and back view.

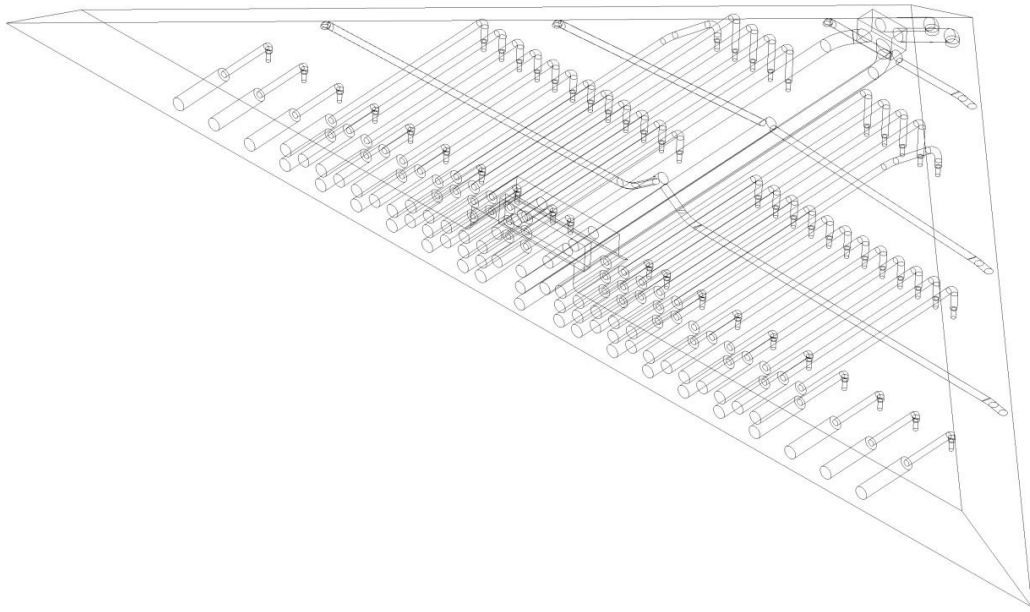


Figure 3.4 Isometric view of the wing model.



Figure 3.5 Photographs of fabricated wing.

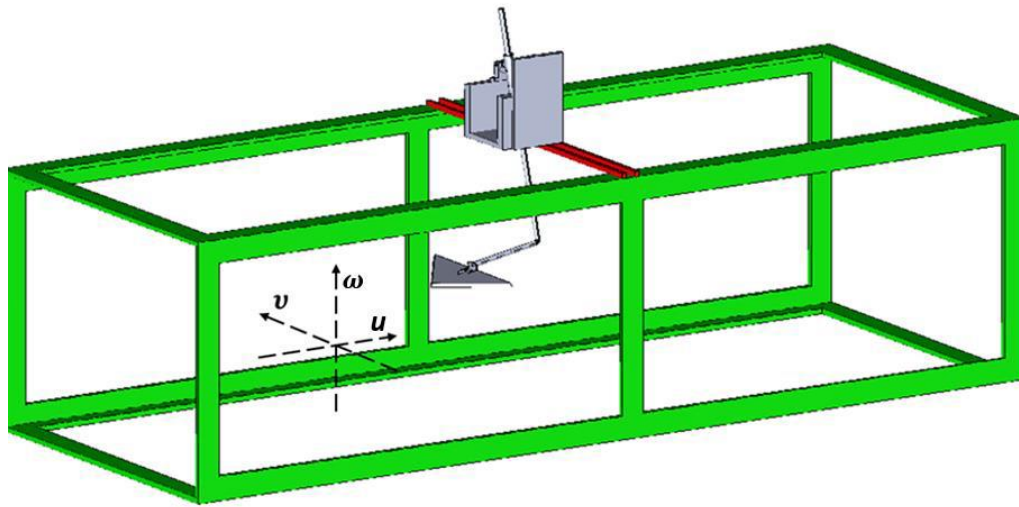


Figure 3.6 Wing model, mount and test section assembly.

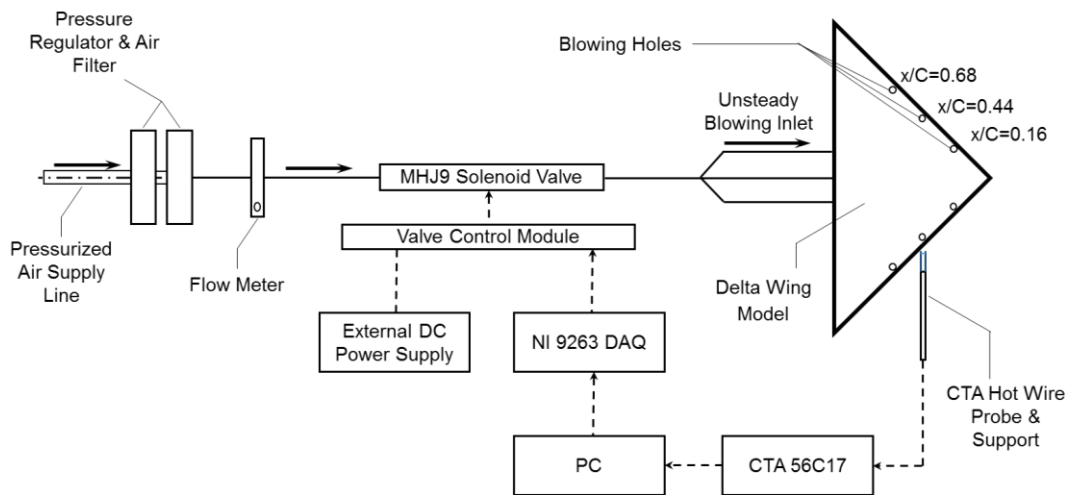


Figure 3.7 Unsteady blowing flow control setup.

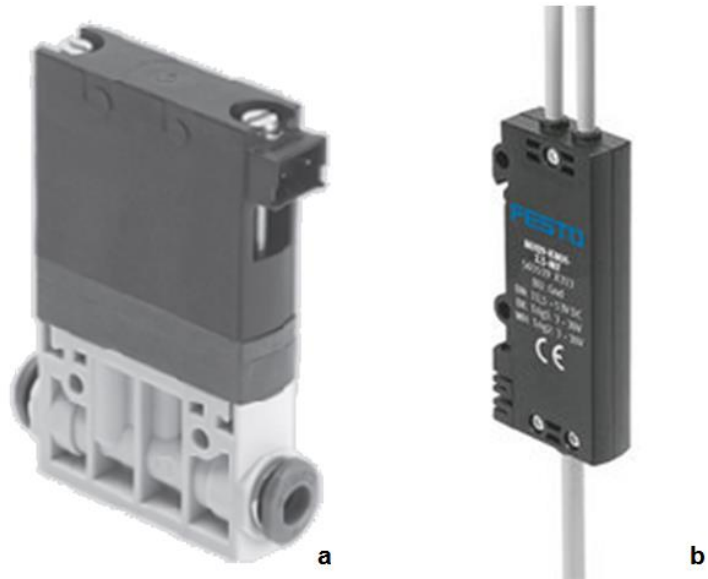


Figure 3.8 MHJ9-QS-4-MF solenoid valve (a), MHJ9-KMH control module (b), photos courtesy of FESTO corp.

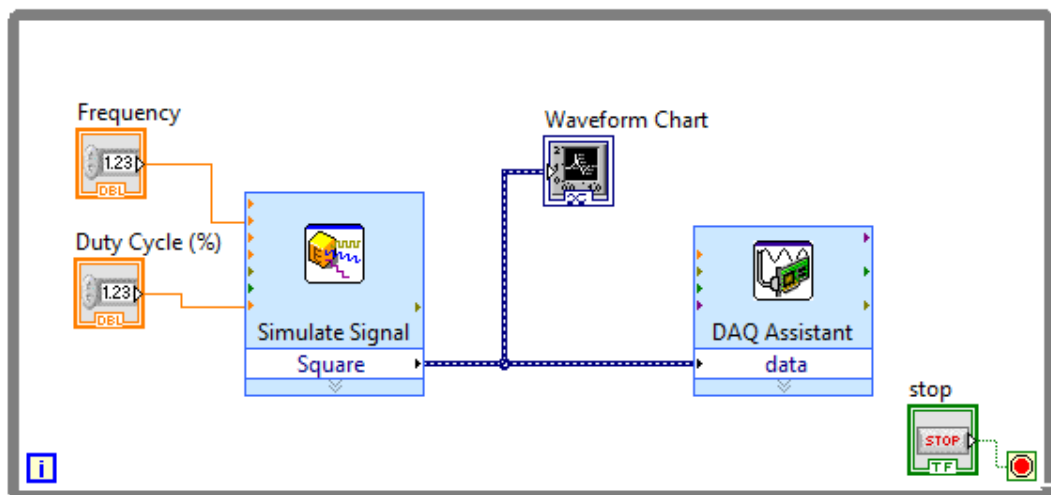


Figure 3.9 Unsteady blowing control setup block diagram in LabVIEW environment.

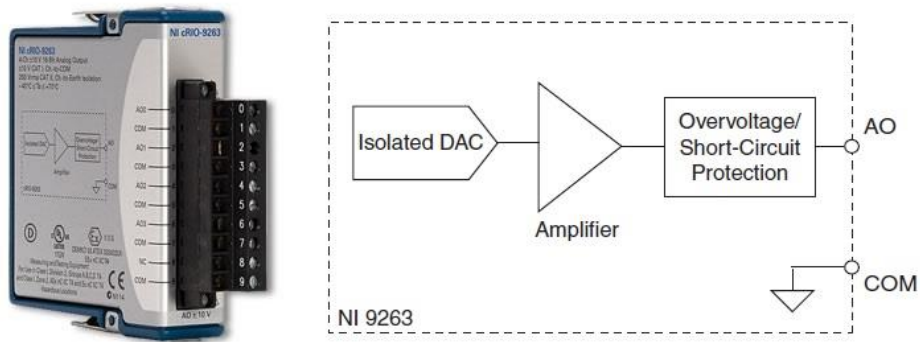


Figure 3.10 NI cRIO 9263 DAQ Card and circuitry, photo courtesy of National Instrument corp.

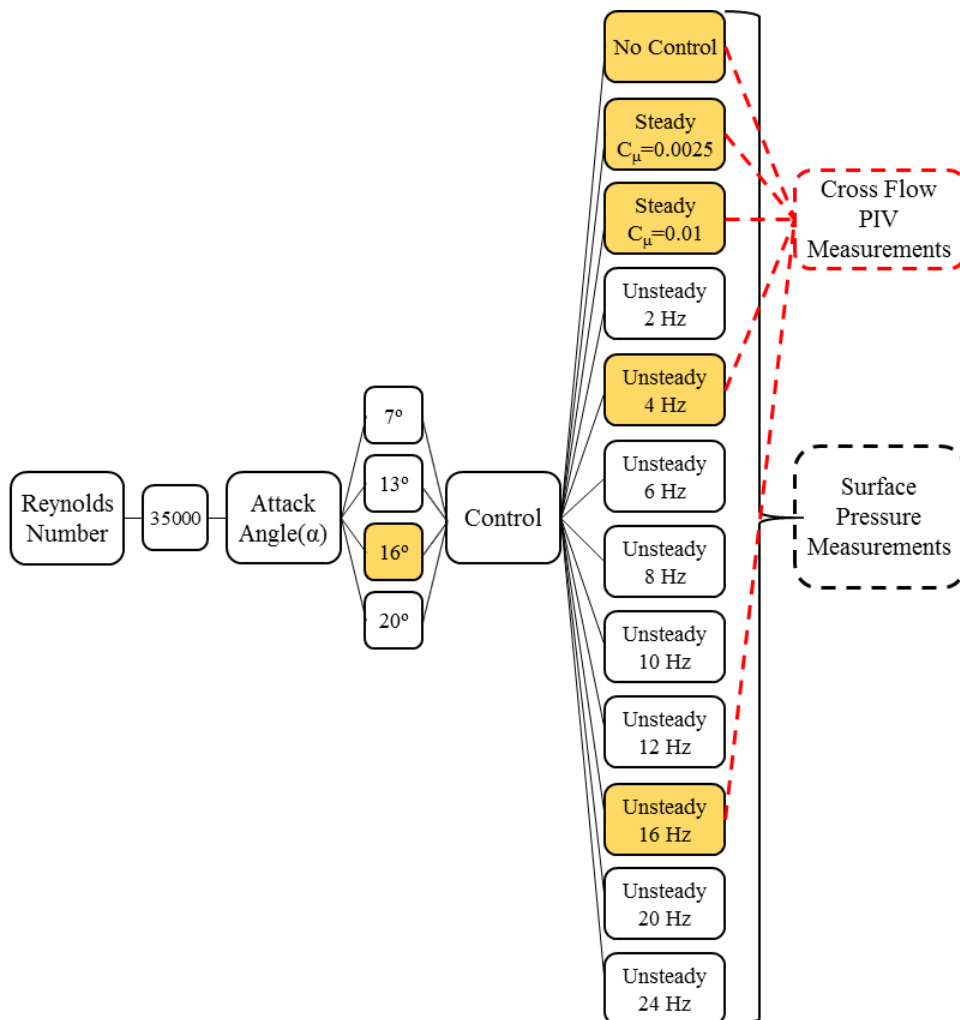


Figure 3.11 Experimental Matrix.

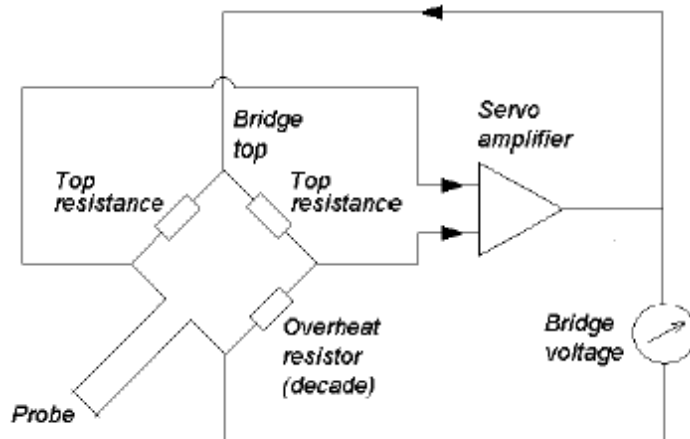


Figure 3.12 CTA Bridge Circuit.

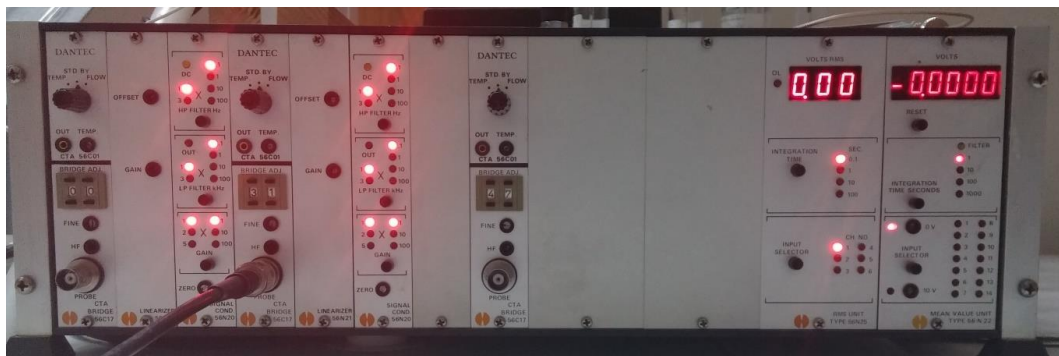


Figure 3.13 CTA Main Unit.

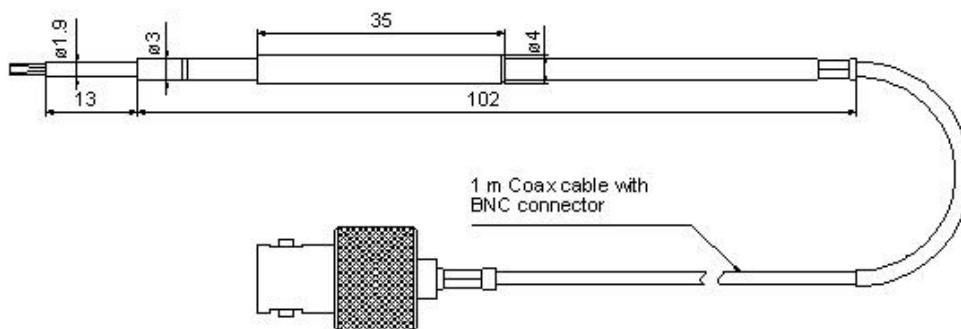


Figure 3.14 Dantec 55P16 hot wire probe.

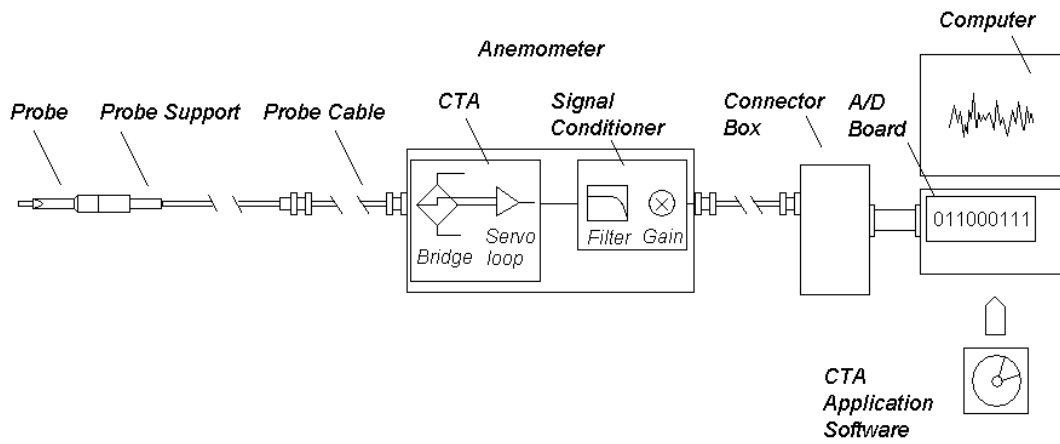


Figure 3.15 CTA measurement chain.

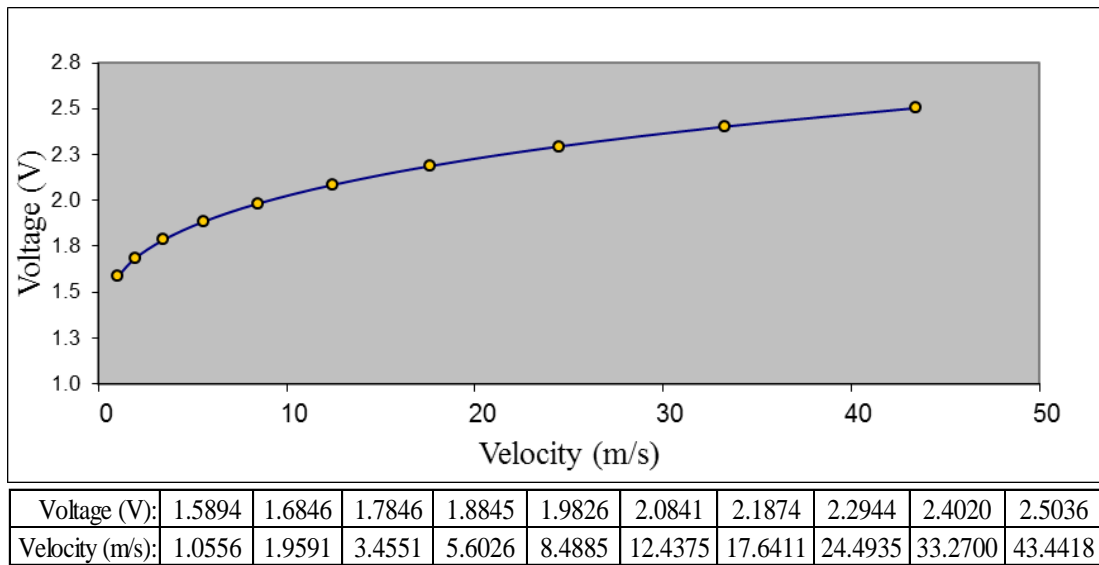


Figure 3.16 Hot wire calibration curve and data.

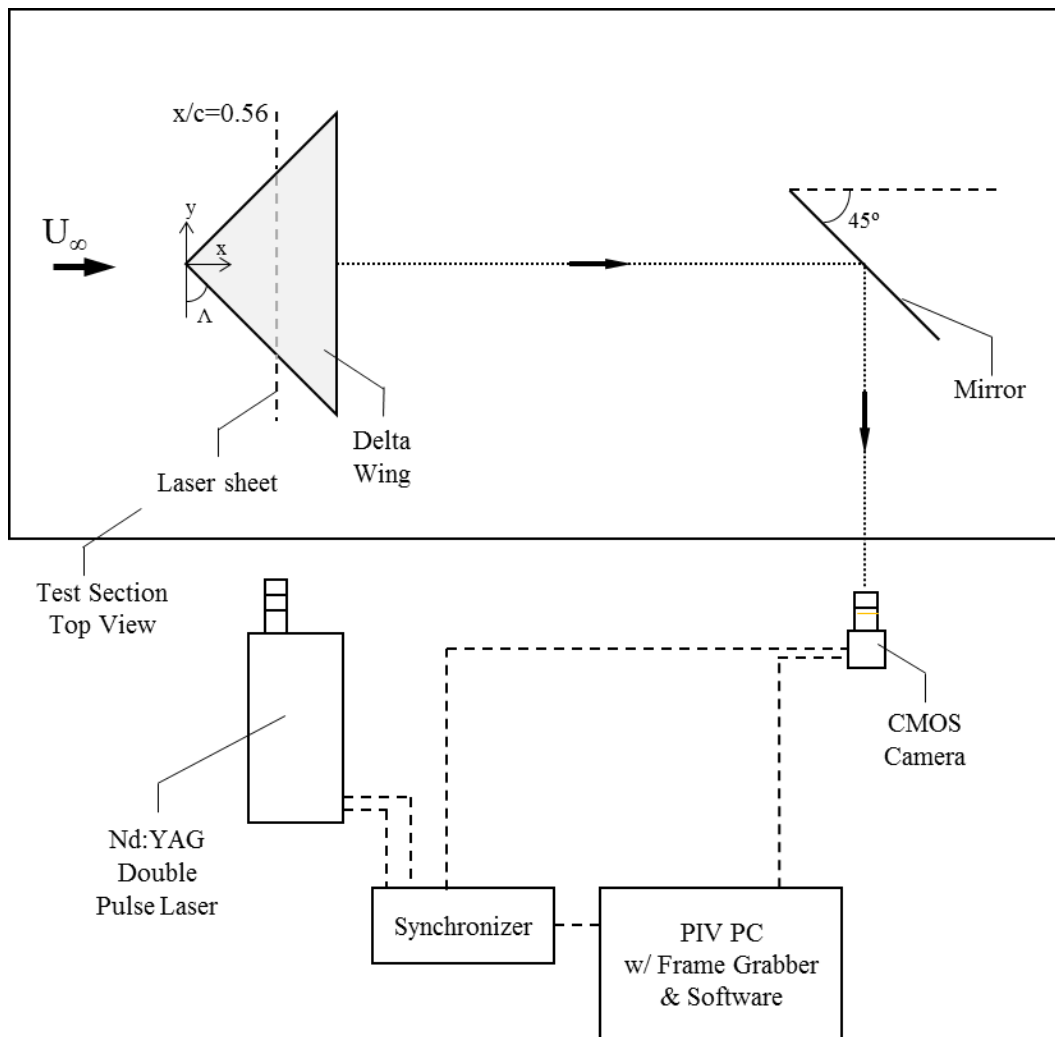


Figure 3.19 Scheme of the PIV experiment set-up.

CHAPTER 4

RESULTS AND DISCUSSION

The results of the experiments throughout this study are given and discussed in this chapter. This section is divided into three parts. First, the characterization of the unsteady blowing setup is discussed in detail. Then, the surface pressure measurements that identify the flow structure both for control and no controlled cases are reported. At last, the results of PIV measurements conducted for selected cases are presented.

4.1 Blowing Characterization

The leading edge blowing both for unsteady and steady cases is characterized using velocity measurements at the exit of the blowing holes via hot wire anemometry measurement technique. In order to obtain the desired momentum coefficients for the unsteady cases, the procedure requires adjusting the flow meter using the actual velocity measurements which can also be named as backward tuning.

4.1.1 Unsteady Blowing Cases

The results of the velocity measurements at the exit of the blowing holes for unsteady blowing cases are given in Figure 4.1 and 4.2 for excitation frequencies varying from 2 Hz to 24 Hz. For these figures, five-data moving average was applied in order to smooth out the short-term fluctuations and to highlight the longer-term trend. The raw data are also provided in Appendix A as Figures A1, A2 and A3.

Initially it was expected to obtain a velocity distribution similar to the input signal which was in the form of square wave for all frequencies. However it is seen that

for frequencies varying from 2 Hz to 10 Hz, blowing velocities cannot be maintained constant at the open position of the valve, instead it shows a decreasing pattern. This discrepancy is also evident in similar studies in literature including [83, 89]. As the frequency increases the slope of this pattern decreases and from 12 Hz to 24 Hz time history of the velocity measurements exhibits a better distribution that is similar to the input signal.

Further comparisons can be performed to consider the frequencies of the velocity measurements with the excitation frequencies of the input signal. The desired excitation frequencies are obtained in velocity measurements as clearly indicated in Figures 4.1 and 4.2. In addition, considering the excitation pattern, the excitation frequency, and the duty cycle in general, the consistency among the pulses is witnessed and the repeatability is quite high.

Another observation from the time series of velocity patterns is that the valve could not be reached to the fully closed state after each pulse. The velocity offset is found to be around 0.55 m/s for all excitation frequency cases and compared to the studies in the literature for unsteady blowing applications [83, 87, 89], it is found to be quite consistent.

In order to confirm the aforementioned discussions and interpret the results in frequency domain, the spectral analyses were conducted using MATLAB, for which the source code was also provided Appendix A. Figures 4.3, shows the spectral analysis applied to the velocity measurements for 4 Hz and 16 Hz excitation frequencies. A sample log-log scale chart was also constructed for 24 Hz excitation case and shown in Figure 4.4. The results of the remaining cases are demonstrated in Appendix A, Figure A.3.

In line with the characterization of the unsteady blowing, the momentum coefficient values calculated using the velocity distributions obtained from hot wire measurements are tabulated in Table 4.1 for all cases together with corresponding dimensionless frequencies, Strouhal number. As discussed in Chapter 3 in detail, two different numbers were taken into account, maximum momentum coefficient $C_{\mu,max}$ and effective momentum coefficient $C_{\mu,eff}$. The

$C_{\mu,max}$ value varies between 0.0098 and 0.0106 and the corresponding $C_{\mu,eff}$ changes from 0.0025 to 0.0027, which are in the range of calculated uncertainty values explained in Chapter 3 in detail. These deviations among different frequencies were simply due to the difficulty in adjustment of the flow meters and backward tuning procedure that uses the velocity distributions obtained from hot wire measurements. Thus, it is concluded that the experiments are conducted at $C_{\mu,max}=0.01$ and $C_{\mu,eff}=0.0025$ throughout the study.

Table 4.1 Momentum coefficient values calculated from the mean velocities at the valve-open condition.

Frequency (Hz)	Dimensionless Frequency (St=f.C/U _∞)	\bar{U}_j (m/s)	$C_{\mu,max}$	$C_{\mu,eff}$
2	0.09	14.61	0.0104	0.0026
4	0.17	14.67	0.0105	0.0026
6	0.26	14.58	0.0104	0.0026
8	0.34	14.20	0.0098	0.0025
10	0.43	14.75	0.0106	0.0027
12	0.51	14.43	0.0101	0.0025
16	0.69	14.21	0.0099	0.0025
20	0.86	14.77	0.0106	0.0027
24	1.03	14.35	0.0100	0.0025

It is important to mention that, the air is supplied to the wing from a single line which is divided into three sub-lines as it can be seen in Figure 3.7. Considering the locations of the blowing holes and the possible variations in pressure drops in the line, the exit velocities from each station is expected to be different. For that purpose, in order to quantify the deviations in exit velocities between the holes at different stations, the hot wire measurements were conducted from the blowing holes at the different chordwise distances for a selected case. Figure 4.5 demonstrates the velocity measurements from all three blowing locations at excitation frequency of 8 Hz and the corresponding momentum coefficients are

tabulated in Table 4.2. The maximum value occurs at the third blowing hole location, which corresponds to the chordwise distance of $x/C=0.68$, and decreases toward the first location. At that point second hole location exhibits an average characteristic through the wing model. For that reason, the reporting of hot wire measurements is based on the velocity measurements conducted from the second hole, which corresponds to the chordwise distance of $x/C=0.44$.

Table 4.2 Momentum coefficient values calculated for different hole locations.

Hole Position x/C	Frequency (Hz)	\bar{U}_j (m/s)	$C_{\mu,max}$	$C_{\mu,eff}$
0.16	8	11.95	0.0023	0.0006
0.44	8	14.47	0.0034	0.0009
0.68	8	16.11	0.0042	0.0010
Total Momentum Coefficient:			0.0099	0.0025
Total Momentum Coefficient based on measurement at $x/C=0.44$:			0.00102	0.0026

4.1.2 Steady Blowing Cases

In order to understand the effect of unsteady blowing on flow structure in detail and to quantify the difference with respect to the base cases obtained with steady blowing, the characterization of blowing set up for steady blowing cases is also needed. In a similar fashion described in unsteady blowing characterization, steady blowing characterization was conducted using hot wire anemometry measurements. For comparison purposes, the maximum and the effective momentum coefficients in unsteady blowing cases, 0.01 and 0.0025, were also obtained for steady blowing cases. The velocity measurements for steady blowing are plotted as a function of time and given in Figure 4.6. The mean velocities of the steady blowing cases are found as 14.29 and 7.25 m/s for which the corresponding momentum coefficient values are 0.01 and 0.0026 respectively. In addition, the root mean square (RMS) values for the velocities are calculated as 2.872 and 1.767 m/s that are indicating the level of turbulence encountered in the blowing set-up.

4.2 Surface Pressure Measurement Results

Effect of unsteady leading edge blowing on the flow structure of a low swept delta wing was investigated by surface pressure measurements. The mean pressure and pressure fluctuation distributions against non-dimensional spanwise distance at chordwise location of $x/C=0.56$ are plotted for all cases. The pressure coefficient C_p was calculated for the mean pressure distribution and the $C_{p,RMS}$ was calculated for the pressure fluctuation analysis. The details of the calculations are provided in the previous chapter. The pressure coefficient C_p distribution helps to understand the vortical behavior of the flow over the planform that can be used as an indicator for the general aerodynamic performance of the wing. The $C_{p,RMS}$ distribution is expected to highlight the locations on the wing surface which can be considered as critical in terms of buffeting. The C_p and $C_{p,RMS}$ values were calculated in MATLAB and the source codes are given in Appendix B.

Figure 4.7, 4.8, 4.9 and 4.10 show the dimensionless pressure distribution for four different attack angles $\alpha=7^\circ$, 13° , 16° and 20° at Reynolds number of 35000, respectively. In each figure the unsteady blowing results at excitation frequencies of 2, 8, 16, 24 Hz along with the results of steady blowing and no control cases are demonstrated. These frequency cases are selected to simplify the charts for discussions. The charts, which involve the results of all excitation frequencies tested, are demonstrated in Appendix C as Figures C1, C2, C3 and C4, respectively.

Considering the results for the attack angle $\alpha=7^\circ$ as shown in Figure 4.7 (C1), the pressure distribution for all cases demonstrate a pattern which can be considered as the footprint of vortical structure on the wing surface. This pattern includes a region of high $-C_p$ values, which is defined as suction and believed to be representing the location of vortex core. Similarly, a region of low $-C_p$ values proximity to the center of the wing indicates flow attachments to the wing surface. Starting from the lowest excitation frequency, the effect of blowing is evident. The effects of excitation frequencies between 2 and 10 Hz appear minimal whereas greater excitation frequencies show relatively higher impact on the C_p

distribution. It is witnessed that as the frequency increases the effect of unsteady blowing on pressure distribution increases and the largest rise relative to no blowing case achieved in $-C_p$, so in suction, is 0.16. Considering the steady blowing cases, It is seen that blowing at $C_\mu=0.01$ is the most effective among all the cases tested and the peak in suction increases a value of 0.3 from the peak obtained for no control case. The steady blowing at $C_\mu=0.0025$ results in pressure distribution that is similar to unsteady control cases with excitation frequencies between 2 to 10 Hz. In addition, it is important to mention that the peak value in suction appears closer to the leading edge when the blowing is applied. The spanwise location of the peak in $-C_p$ is detected at $y/S=0.57$ for no control case and it is around $y/S=0.63$ for the cases which the steady and unsteady blowing are applied.

Figure 4.8 (C.2) shows the results of pressure distributions for the attack angle $\alpha=13^\circ$. The effect of unsteady blowing on pressure distribution is clearly apparent for all excitation frequencies. Excitation frequencies up to 8 Hz generate substantial shifts in pressure distributions compared to their corresponding effect at attack angle of 7 degree shown in Figure 4.7. Increase in excitation frequency causes gradual shift in pressure distribution where the highest shift is obtained at 16 Hz. It is important to emphasize that further increase in frequency exhibits a reduction in the amount of the shift in the pressure distribution. Considering the steady blowing cases, there is no noticeable effect of blowing on pressure distribution at $C_\mu=0.0025$. However, at sufficiently high momentum coefficient of $C_\mu=0.01$, the improvement in the pressure distribution is clearly evident and the distribution is quite similar to the one obtained with unsteady blowing at frequency of 10 Hz. In addition, considering all the blowing cases, the largest increase in peak values of $-C_p$, so in suction is 0.23 which is obtained with unsteady blowing at excitation frequency of 16 Hz.

The results of pressure distributions for $\alpha=16^\circ$ are shown in Figure 4.9 (C.3). No control case tends to show a flat like pressure distribution for most of the spanwise location, which is an indication of loss in the strength of the vortical

structure. When the blowing cases are considered, the effect of blowing on pressure distribution is apparent. As the excitation frequency increases, footprint indicating vortical structure starts to appear. For excitation frequencies greater than 4 Hz, the effect of unsteady blowing control is substantial and exceeds the improvement provided by the steady blowing. Even though an improvement is evident with steady blowing, it seems to be quite limited and does not allow complete transformation of flow structure to vortical structure. In addition, increase in the peak suction reaches to 0.4 at the excitation frequency of 16 Hz where the highest improvement is obtained.

The results of the pressure distributions at the highest attack angle $\alpha=20^\circ$ are given in Figure 4.10 (C.4). For no control case, the pressure distribution shows complete flat behavior, which is a clear indication of stalled wing condition. In addition, there is no significant effect of blowing on pressure distribution for steady blowing at $C_\mu=0.0025$ and $C_\mu=0.01$, and unsteady blowing at frequencies up to 4 Hz. Increase in excitation frequency to 6 and 8 Hz cause a shift in pressure distribution with greater $-C_p$ values while maintaining its flat profile. Further increase in the excitation frequency causes recovery of vortical structures as inferred from the pressure distribution. In line with the observations at lower incidences, the most improved pressure distribution is achieved with the unsteady blowing case at the excitation frequency of 16 Hz. No more improvement is observed for further increase in the excitation frequency.

In order to highlight the effect of attack angle at different blowing conditions, the pressure distributions were plotted in a single chart for four different attack angles as shown in Figure 4.11 for the conditions of no control, steady control with $C_\mu=0.0025$ and 0.001 , and unsteady blowing at 16 Hz. Increasing the attack angle causes a progressive deterioration in pressure distributions from vortical footprint to flat profile up to $\alpha=20^\circ$ for no control and steady blowing with $C_\mu=0.0025$ and $C_\mu=0.01$. In addition, peak suction values considerably decreases and their spanwise locations move toward inboard of the symmetry plane. Considering the unsteady blowing case at the excitation frequency of 16 Hz, clear footprint of

vortical structure is maintained in pressure distribution up to $\alpha=16^\circ$ with varying $-C_p$ values, and a considerably recovered pressure distribution is even identifiable at $\alpha=20^\circ$. In addition, for this blowing condition, the maximum $-C_p$ values have reached to a value around 1.17 for all incidences, which might be quite critical in terms of maintaining similar suction behavior at different attack angles with a single control strategy.

The $C_{p,RMS}$ distributions of the corresponding cases for the attack angles $\alpha=7^\circ$, 13° , 16° and 20° are shown in Figures 4.12, 4.13, 4.14 and 4.15, respectively. The methodology to construct the charts for the mean pressure distribution is applied for $C_{p,RMS}$ distributions, such that in each figure the unsteady blowing results at excitation frequencies of 2, 8, 16, 24 Hz along with the results of steady blowing and no control cases are demonstrated. These frequency cases are selected to simplify the charts for discussions. The charts, which involve the results of all excitation frequencies tested, are demonstrated in Appendix C as Figures C5, C6, C7 and C8, respectively.

For $\alpha=7^\circ$ as shown in Figure 4.12 (C5), the $C_{p,RMS}$ values remain similar at inboard locations that is between $y/S=0.14$ and $y/S=0.38$ for all cases. As moving outward, toward the leading edges, the $C_{p,RMS}$ values start to exhibit variations along the spanwise distance. However, the deviation between the pressure taps is minimal for no control and steady blowing cases while the changes are clearly noticeable for the unsteady blowing cases. There exists an initial peak in $C_{p,RMS}$ at $y/S=0.51$ that is followed by a base value at $y/S=0.58$ then a secondary peak is observed at $y/S=0.63$ for all unsteady control cases. The existence of two peak points in $C_{p,RMS}$ distribution can be the indication of the dual vortex structure for these cases. The outmost $C_{p,RMS}$ pattern occurs at 16 Hz excitation frequency and the maximum $C_{p,RMS}$ value is 0.14 which coincides with the location of the maximum $-C_p$ value.

Considering the results of $\alpha=13^\circ$ as shown in Figure 4.13 (C6), the $C_{p,RMS}$ increases starting from $y/S=0.14$ to $y/S=0.38$ for all cases with similar profile. The

outermost cases are 2 Hz and 4 Hz unsteady control at that location. As moving outward toward the leading edges, the $C_{p,RMS}$ values show a decreasing pattern in a fluctuating manner almost for all cases. The relatively lower values occur for no control case.

For $\alpha=16^\circ$ as shown in Figure 4.14 (C7), the $C_{p,RMS}$ does not significantly vary across the whole span in no control case. For steady control with $C_\mu=0.0025$ the pattern slightly changes from the no control case, whereas the steady control with $C_\mu=0.01$ reaches a broader distribution with greater magnitudes. Unsteady blowing at frequencies varying from 2 Hz to 8 Hz exhibits a similar pattern shifted upward with increasing frequency. For higher frequencies 10 Hz to 24 Hz, the $C_{p,RMS}$ distributions exhibit also similar pattern where the $C_{p,RMS}$ value increases up to the distance $y/S=0.45$ then decreases toward the leading edge.

For the highest attack angle $\alpha=20^\circ$ case which is shown in Figures 4.15 (C8), the variation in $C_{p,RMS}$ along the span is minimal which is analogous to the flat distribution. As the control is applied, slight shifts in $C_{p,RMS}$ distributions are noticed which are evident for all blowing conditions.

Up to $\alpha=16^\circ$, for the most of the cases having vortical structure footprint, greater $C_{p,RMS}$ values are distributed between the reattachment locations and vortex core regions where could be inferred from lowest and peak values of $-C_p$.

4.2.1 Spectral Analysis of the Pressure Measurements

Even though the pressure scanner is primarily used for the mean pressure measurements and is not suitable for unsteady pressure analysis in detail with the current experimental setup, due to acquiring data at high sampling rate, the spectral analyses were also conducted. It was aimed to see whether the fluctuations induced by the periodic blowing could be captured in the pressure data. For that purpose, the spectral analyses of the pressure data at $y/S=0.63$ are presented in Figure 4.16 for the excitation frequencies of 4 Hz and 16 Hz and the attack angles of $\alpha=7^\circ$, 13° , 16° and 20° . The results indicate that the excitation frequencies of 4 Hz and 16 Hz are captured in the spectral analyses of pressure

data for relatively lower attack angles $\alpha=7^\circ$ and 13° . Considering the higher attack angles of $\alpha=16^\circ$ and 20° , there are no significant spectral peaks detected at the excitation frequencies even though the footprints of the corresponding frequencies are evident. It is important to note that these are only the results of single point measurements and not sufficient for global characterization of the fluctuations.

4.3 Particle Image Velocimetry Measurement Results

Cross flow Particle Image Velocimetry experiments at chordwise distance of $x/C=0.56$ were conducted only for the selected cases based on the results of pressure measurements in order to understand the effect of blowing on global flow field and to confirm the conclusions drawn by the results of the pressure measurements. The attack angle of $\alpha=16^\circ$ was selected for PIV measurements. This case is a suitable test case since it includes distinct effects of steady and unsteady blowing on pressure distributions. In addition, this case includes the transformation of flat pressure profile to vortex-dominated profile when the blowing is applied. For that purpose, the cross flow PIV experiments at chordwise distance of $x/C=0.56$ were conducted for the following cases; no control, steady blowing at $C_\mu=0.0025$ and $C_\mu=0.01$, and unsteady blowing at excitation frequencies of 4 Hz and 16 Hz. Preliminary tests were conducted to check the symmetry in the flow field. As once this was confirmed, half wing was utilized in PIV experiments to increase the spatial resolution.

The time-averaged velocity vectors (\mathbf{V}), contours of constant non-dimensional axial vorticity ($\omega C/U_\infty$), and streamlines (ψ) are demonstrated in Figures 4.17, 4.18 and 4.19, respectively. For no control case, the velocity vectors show that the rotational core is very close to the wing centerline where the shear layers reattach to the wing surface. This can be the footprint of stall or pre-stall condition. When the steady blowing $C_\mu=0.0025$ is introduced there hasn't been a considerable change in vector field and streamlines, whereas the spatial extent of the vorticity contours gets smaller and demonstrates a slight movement toward the leading edge. Increase in momentum coefficient to $C_\mu=0.01$, the reattachment line and the vortex core shifts are more apparent with higher crossflow velocities. Considering

the unsteady blowing case at excitation frequency of 4 Hz, it is seen that the flow pattern is quite similar to the ones obtained with steady blowing at $C_{\mu}=0.01$. This observation is quite in line with the results of pressure measurements discussed in the previous sections. When the excitation frequency is 16 Hz, the effect of blowing on flow structure is substantial. The location of vortex core occurs around $y/S=0.50$ and compared to all other cases greater velocity magnitudes and condensed vorticity contours exist. The spatial extent of the vorticity contours along with high magnitudes indicate typical pattern of vortical structure over the wing.

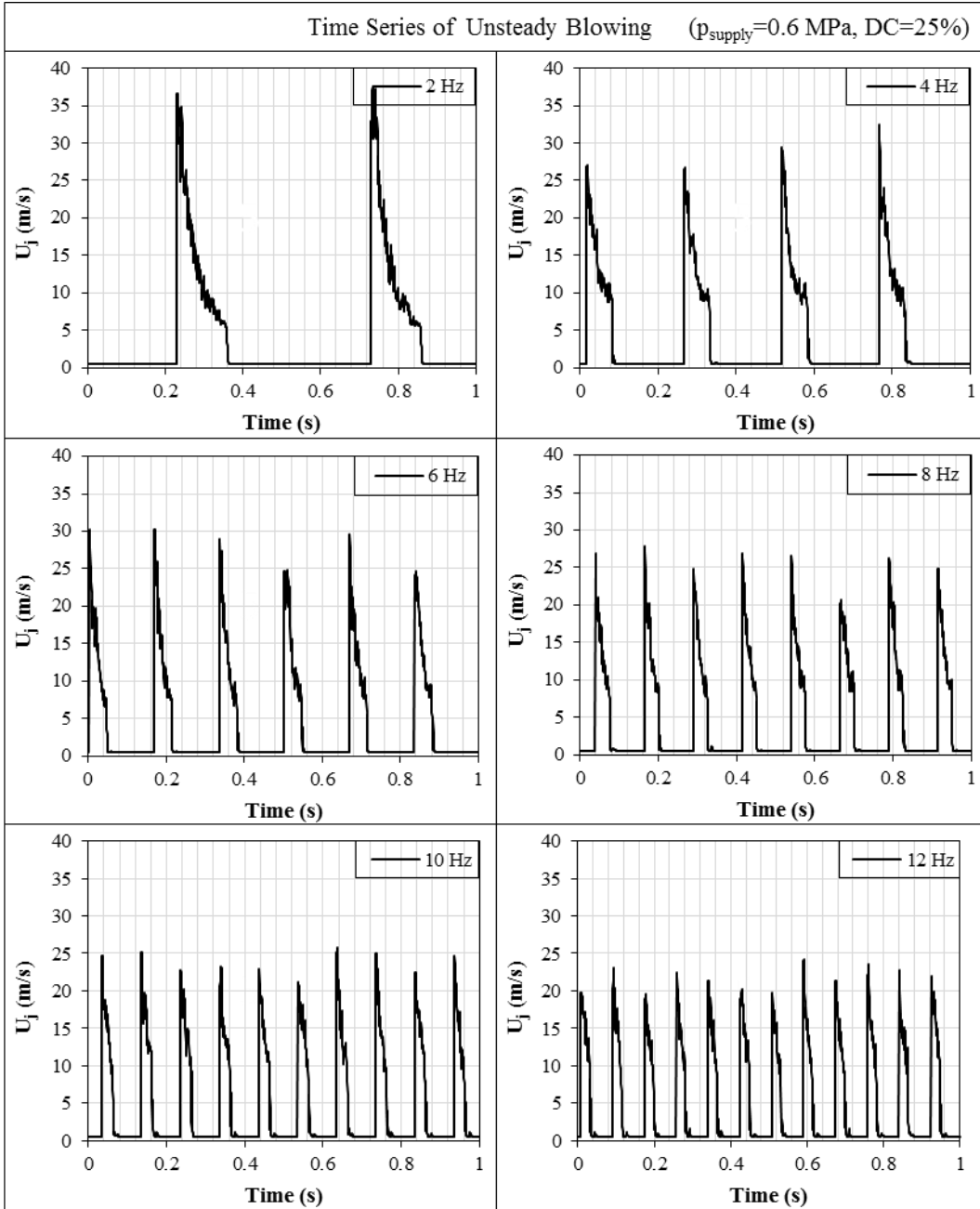


Figure 4.1 Time series of unsteady blowing jet velocity (moving average applied) for all excitation frequencies.

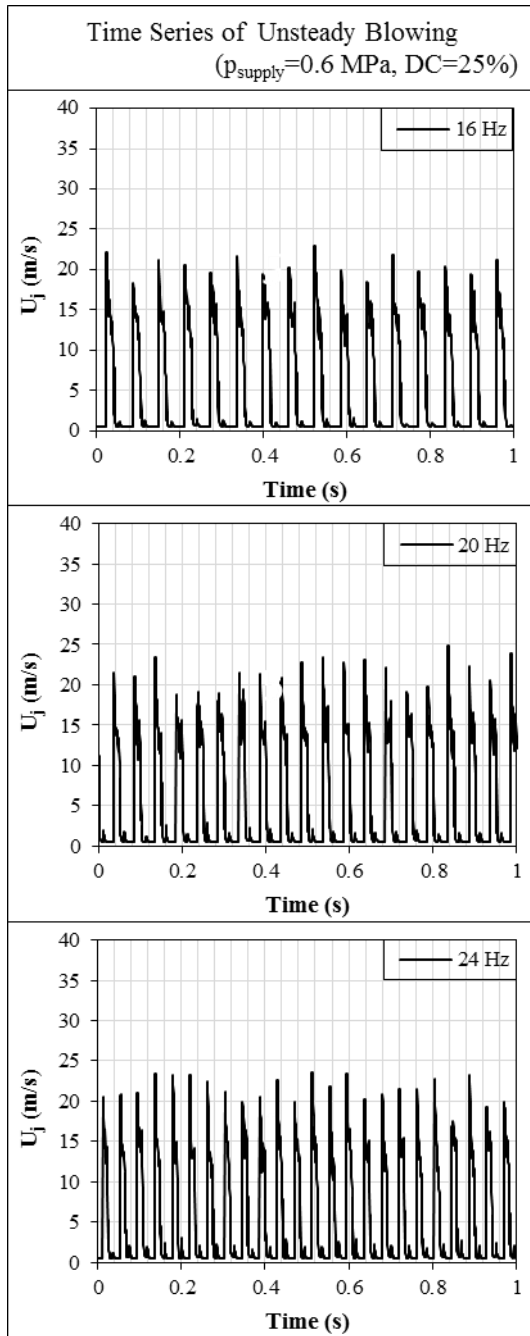


Figure 4.1 (continued) Time series of unsteady blowing jet velocity (moving average applied) for all excitation frequencies.

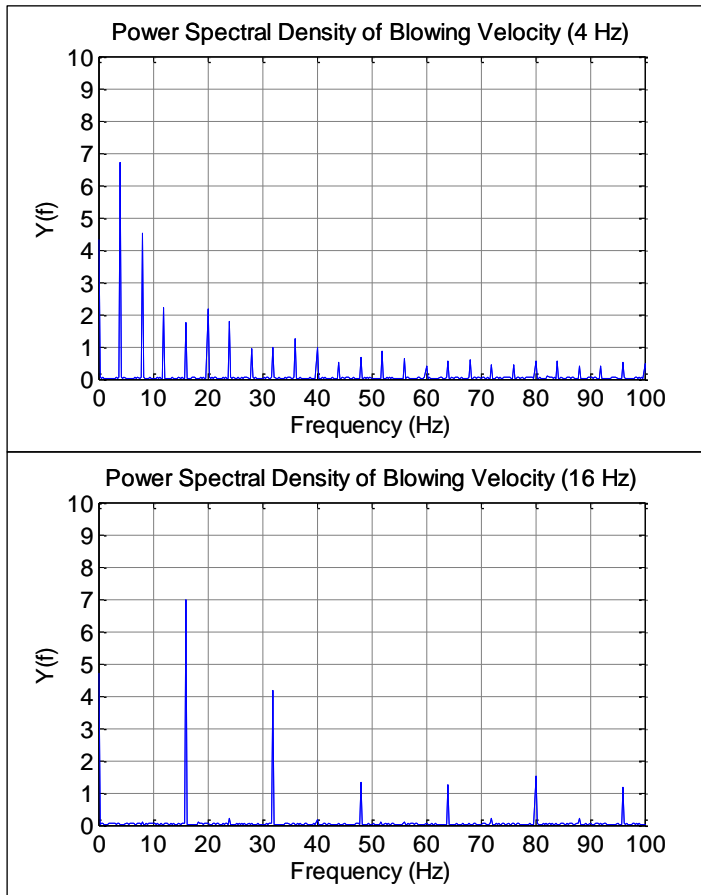


Figure 4.2 Power spectral densities of unsteady blowing jet velocity for 4 Hz and 16 Hz excitation frequencies.

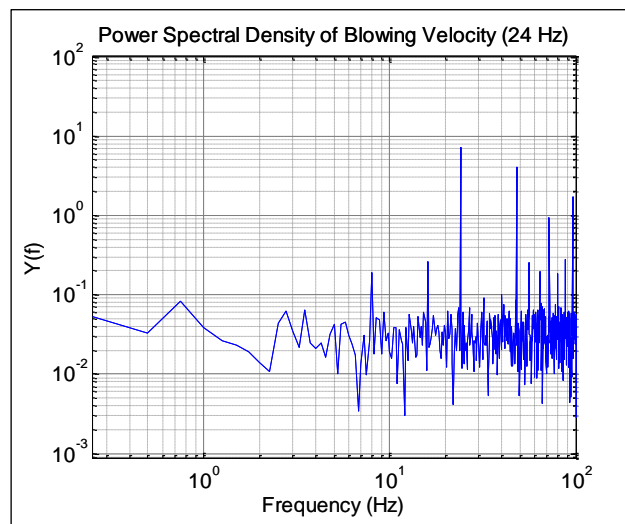


Figure 4.3 Power spectral density of unsteady blowing jet velocity in log-log domain for 24 Hz excitation frequency.

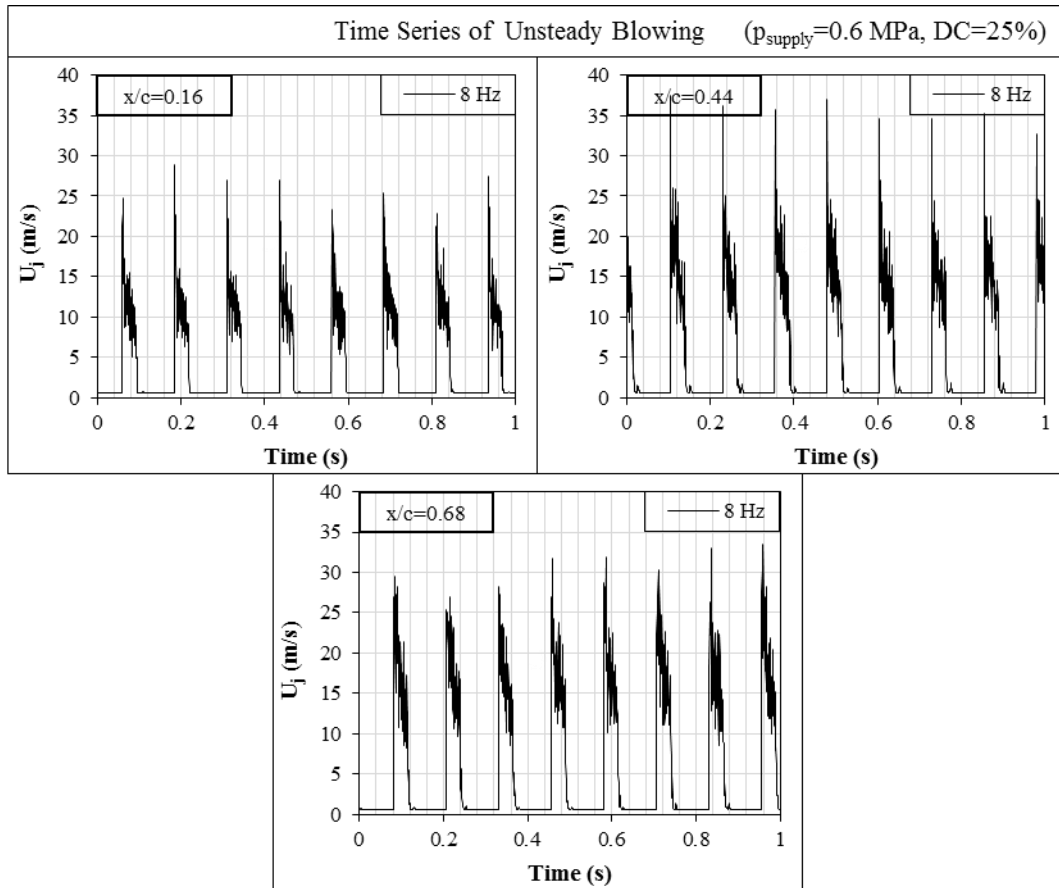


Figure 4.4 Time series of unsteady blowing jet velocity at different hole locations for 8 Hz excitation frequency on a random flow meter adjustment.

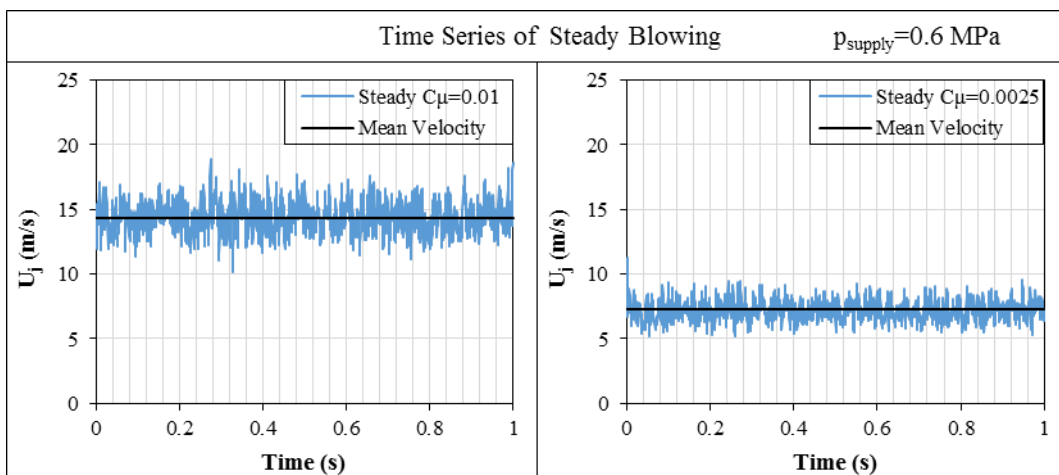


Figure 4.5 Time series of steady blowing jet velocity for $C_\mu=0.0025$ and $C_\mu=0.01$.

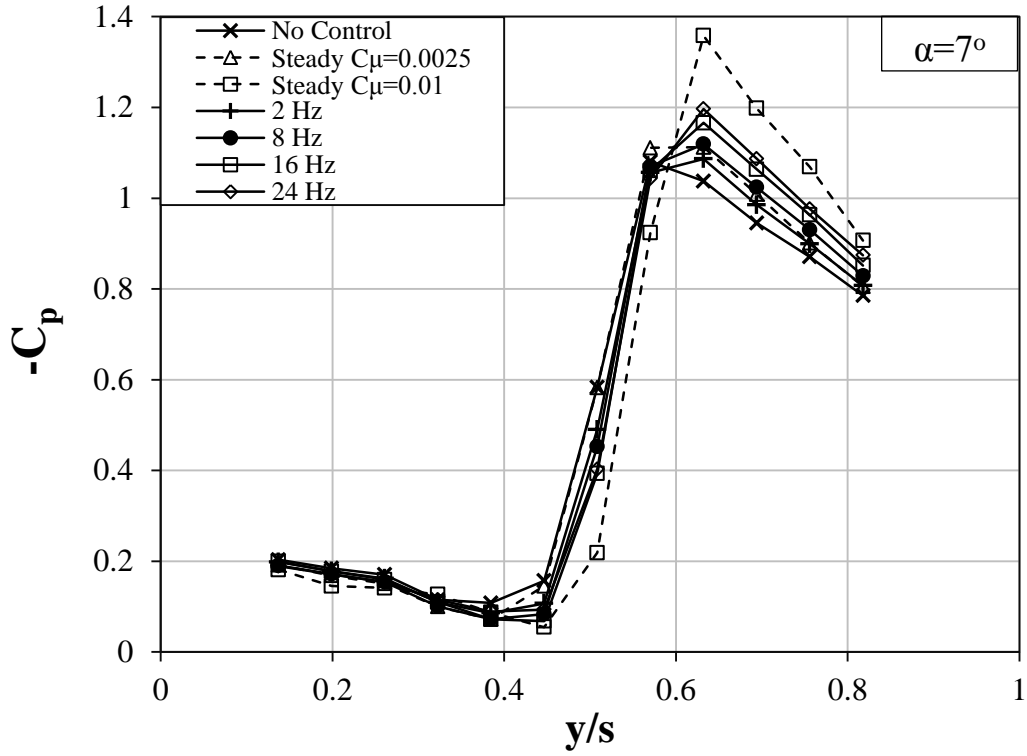


Figure 4.6 Spanwise $-C_p$ distribution on $x/C=0.56$ at $\alpha=7^\circ$ and $Re=35000$ for selected cases.

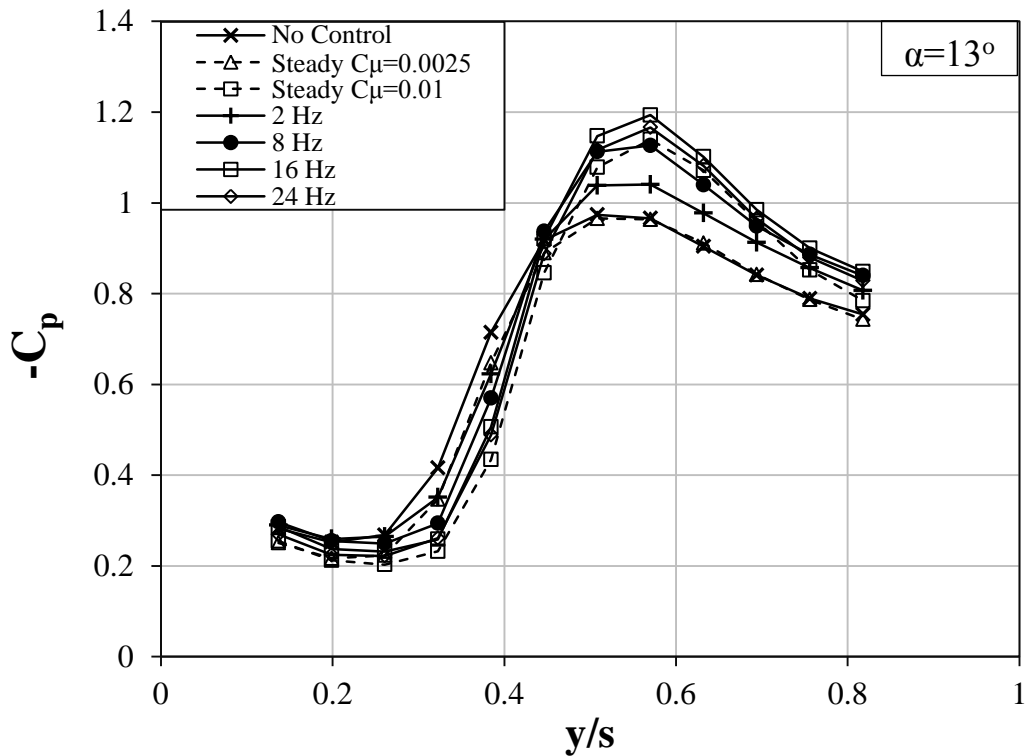


Figure 4.7 Spanwise $-C_p$ distribution on $x/C=0.56$ at $\alpha=13^\circ$ and $Re=35000$ for selected cases

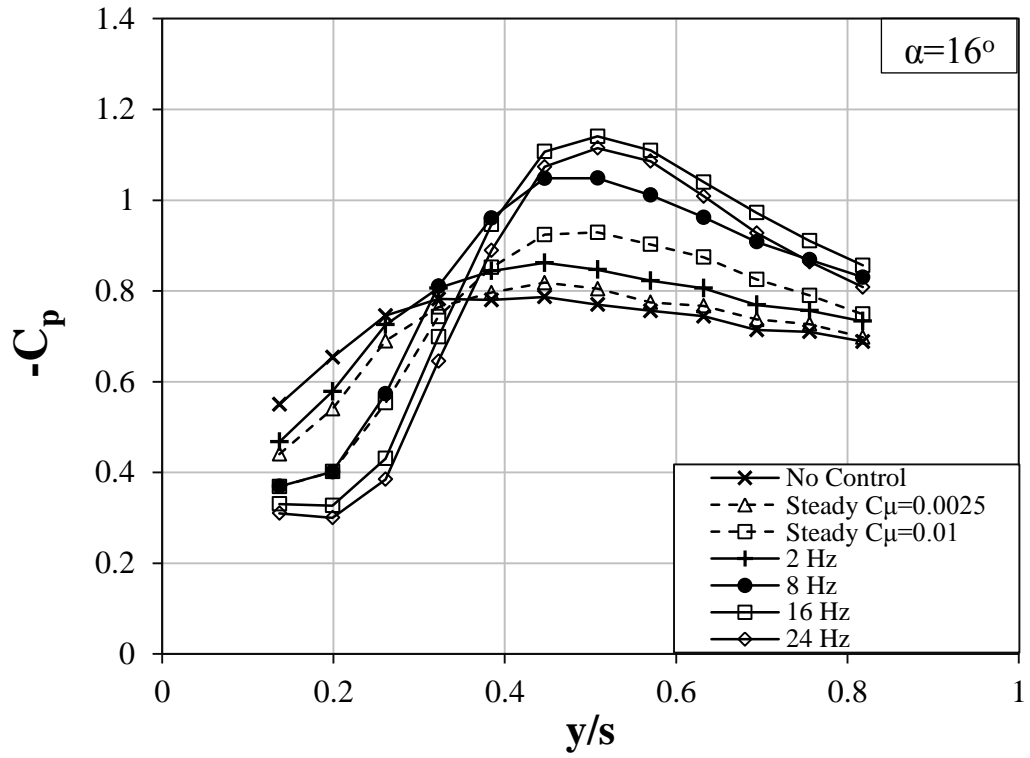


Figure 4.8 Spanwise $-C_p$ distribution on $x/C=0.56$ at $\alpha=16^\circ$ and $Re=35000$ for selected cases.

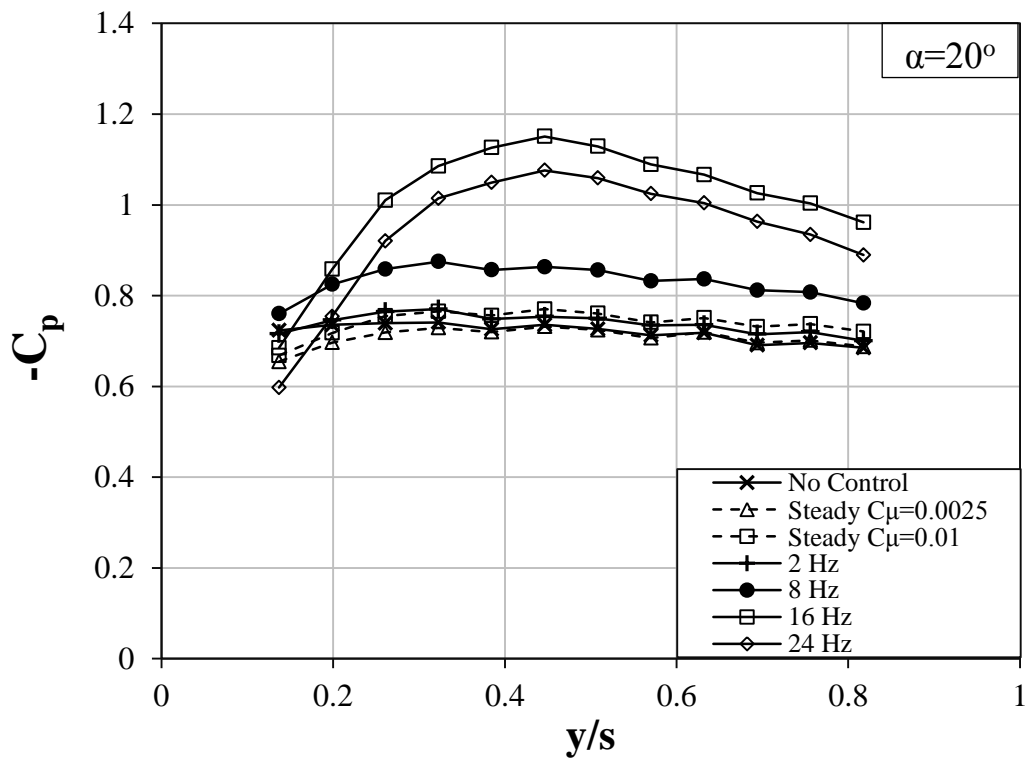


Figure 4.9 Spanwise $-C_p$ distribution on $x/C=0.56$ at $\alpha=20^\circ$ and $Re=35000$ for selected cases.

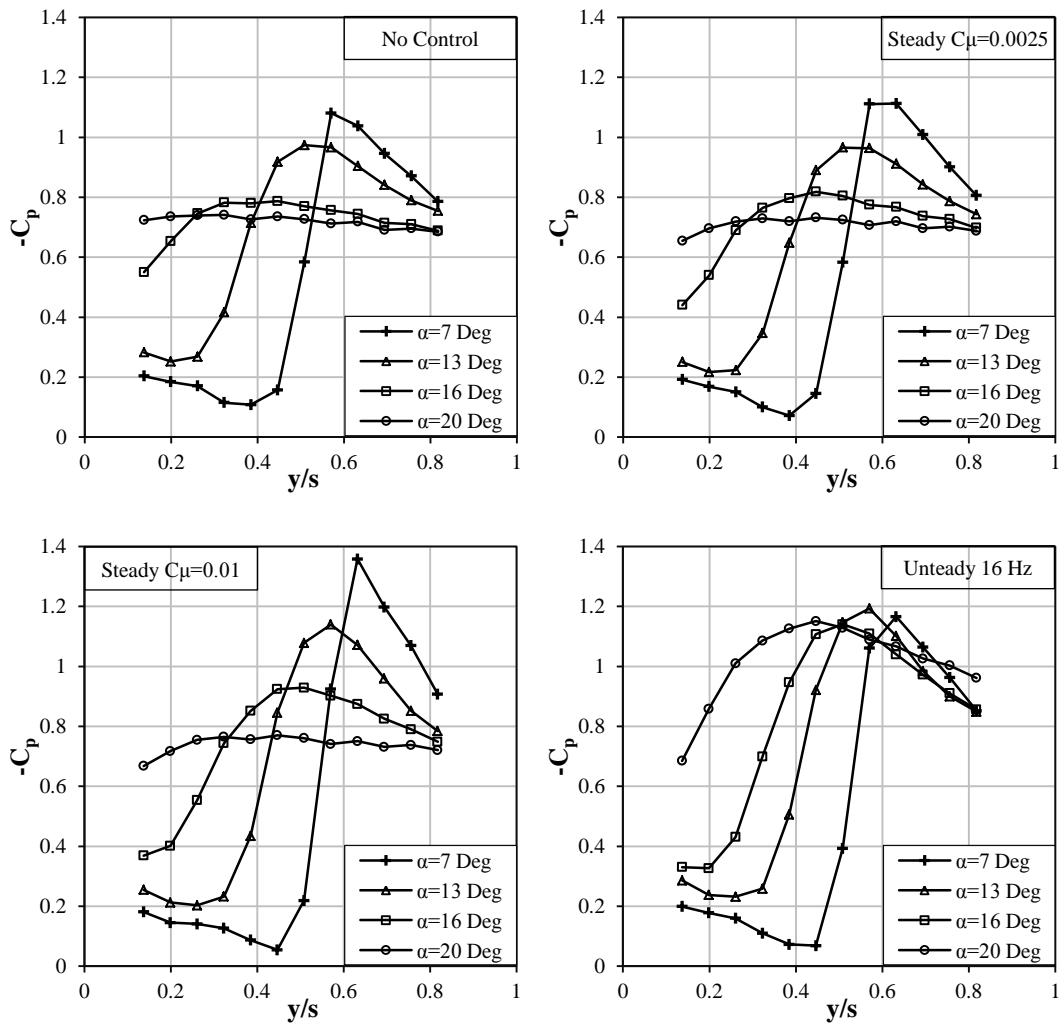


Figure 4.10 Spanwise $-C_p$ distribution on $x/C=0.56$ for no control, steady control with $C_\mu=0.0025$, steady control with $C_\mu=0.01$ and unsteady control with 16 Hz excitation frequency for different attack angles at $Re=35000$.

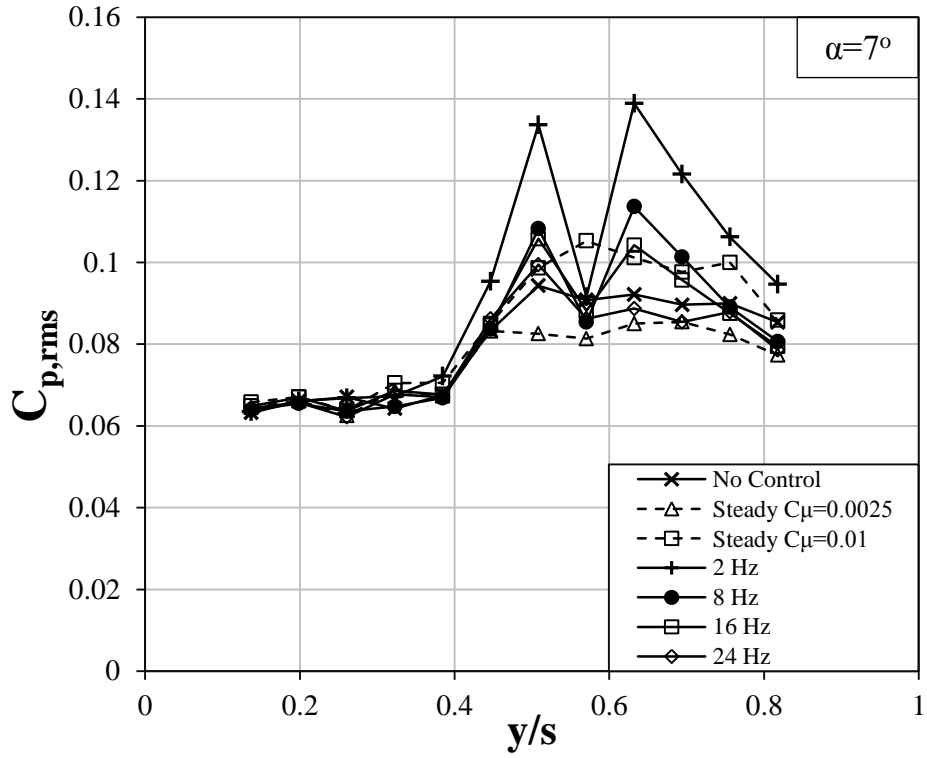


Figure 4.11 Spanwise $C_{p,RMS}$ distribution on $x/C=0.56$ at $\alpha=7^\circ$ and $Re=35000$ for selected cases.

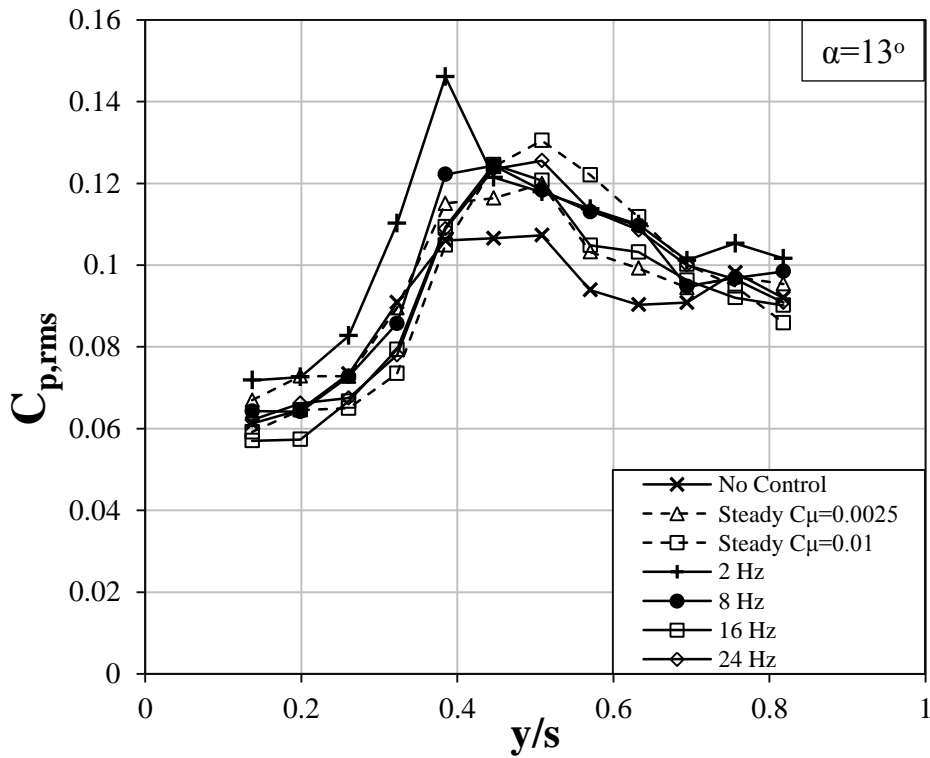


Figure 4.12 Spanwise $C_{p,RMS}$ distribution on $x/C=0.56$ at $\alpha=13^\circ$ and $Re=35000$ for selected cases.

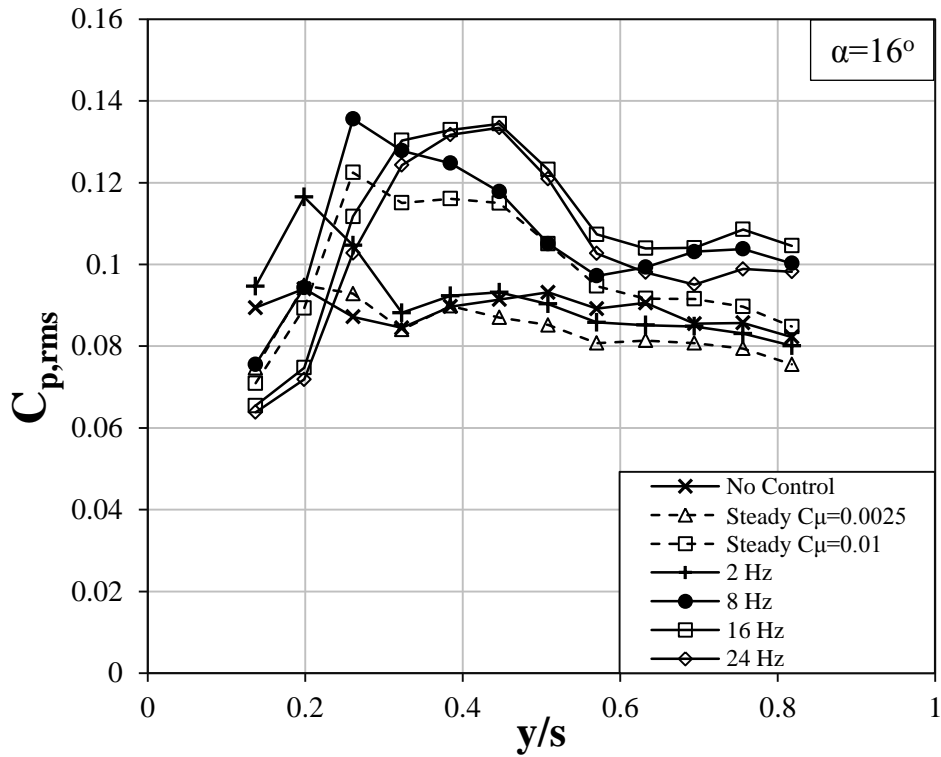


Figure 4.13 Spanwise $C_{p,RMS}$ distribution on $x/C=0.56$ at $\alpha=16^\circ$ and $Re=35000$ for selected cases.

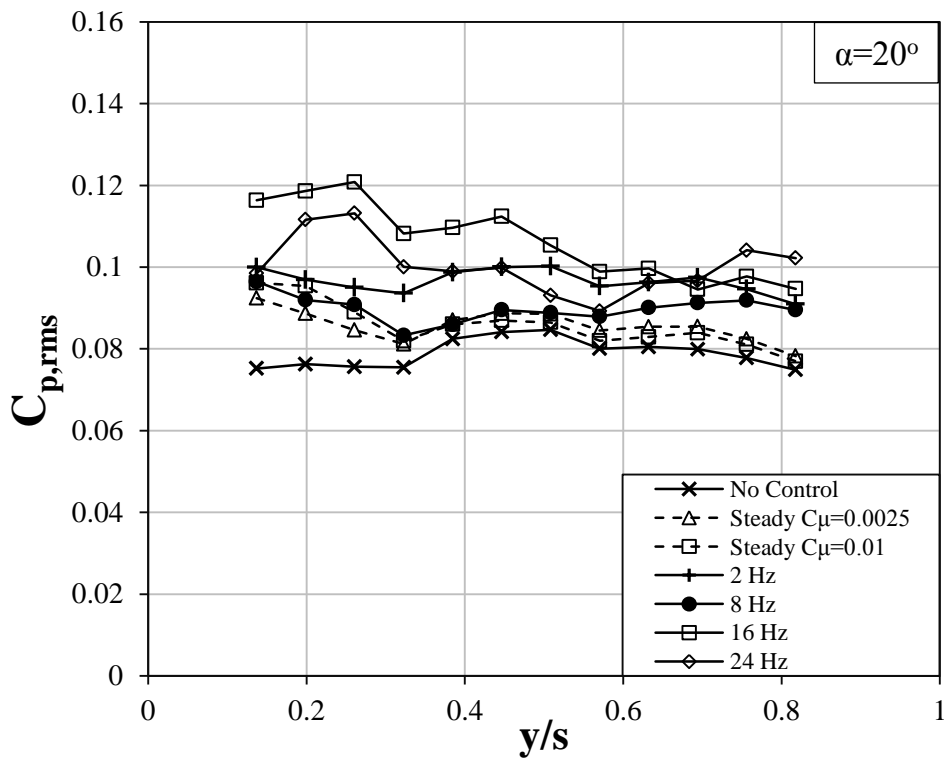


Figure 4.14 Spanwise $C_{p,RMS}$ distribution on $x/C=0.56$ at $\alpha=20^\circ$ and $Re=35000$ for selected cases.

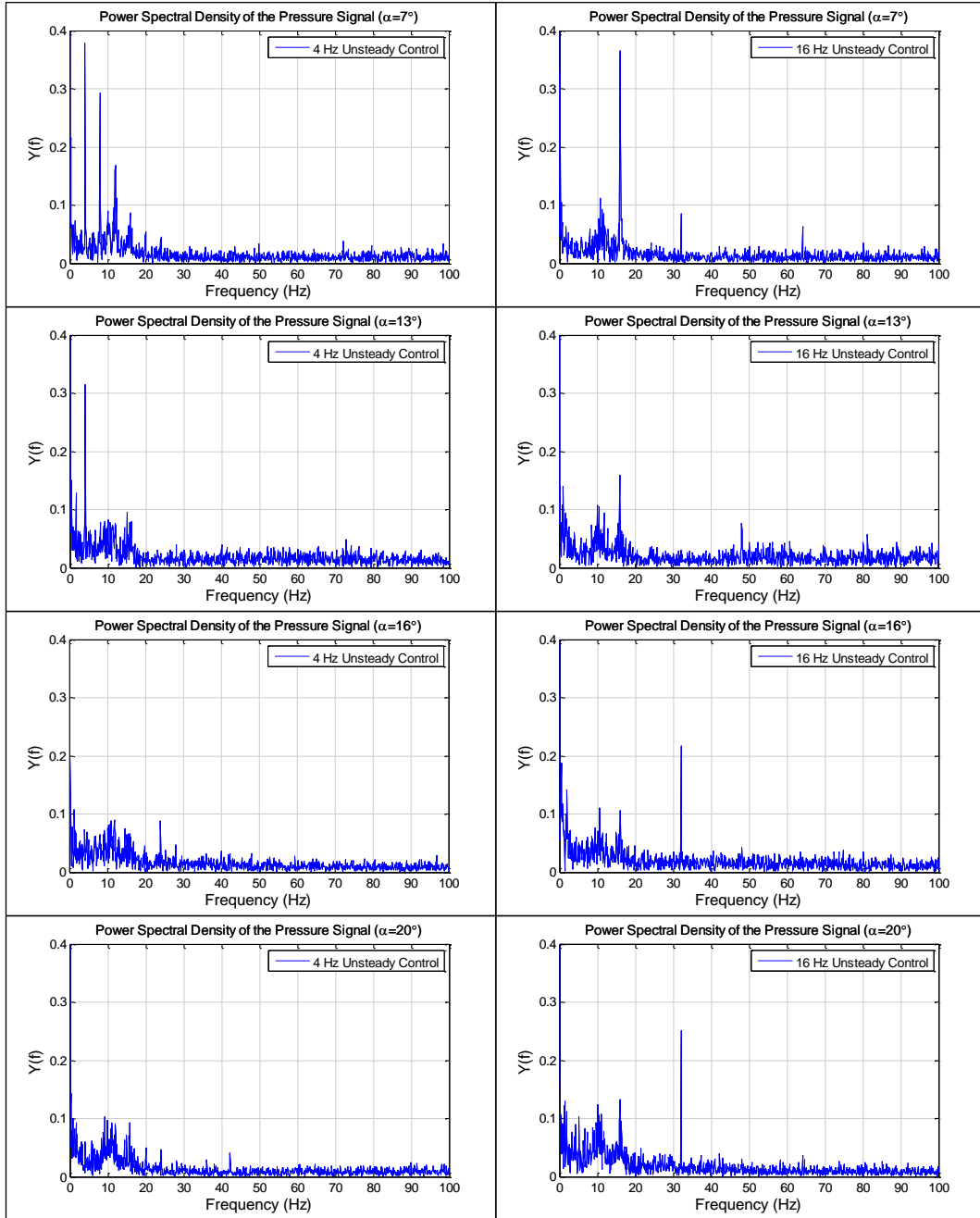


Figure 4.15 Power spectral densities of pressure signals measured at $x/C=0.56$ and $y/S=0.63$ for all attack angles (4 Hz excitation frequency on the left and 16 Hz excitation frequency on the right).

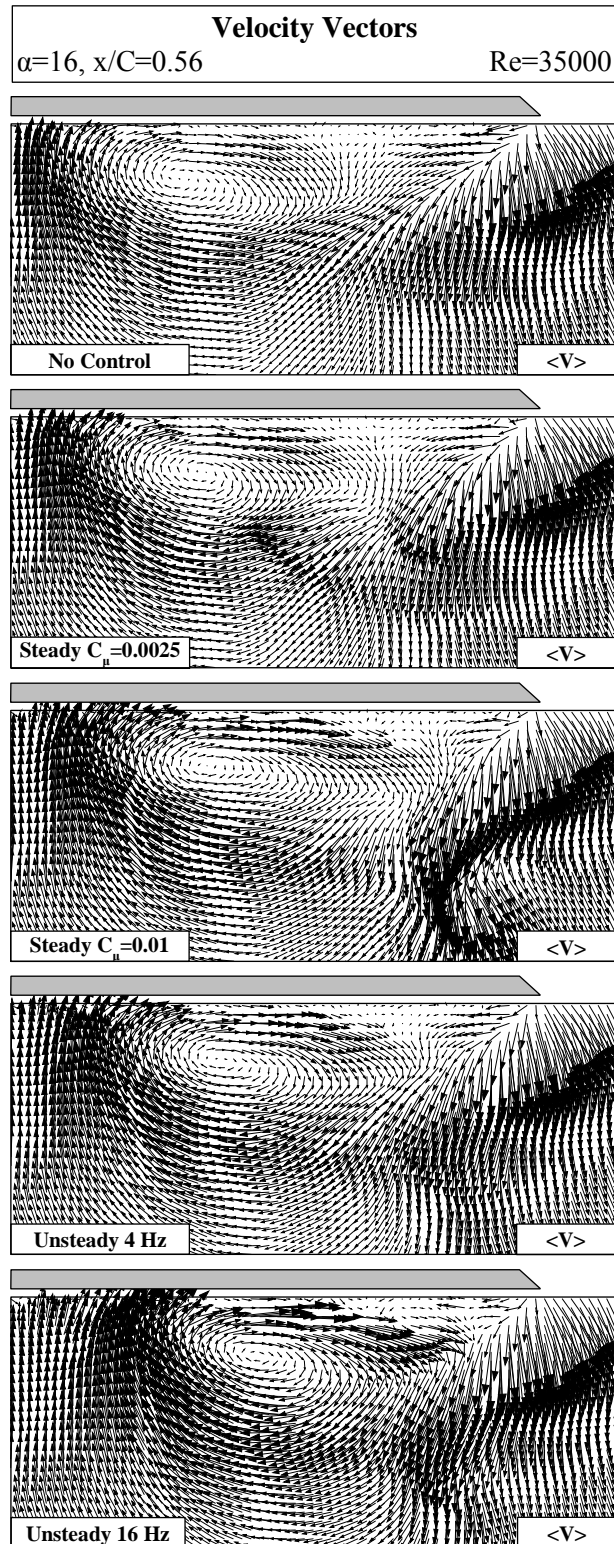


Figure 4.16 Time averaged cross flow velocity vectors at $x/C=0.56$ and $\alpha=16^\circ$ for no control, steady control $C_{\mu}=0.0025$, 0.01 and unsteady control with 4 , 16 Hz excitation frequencies.

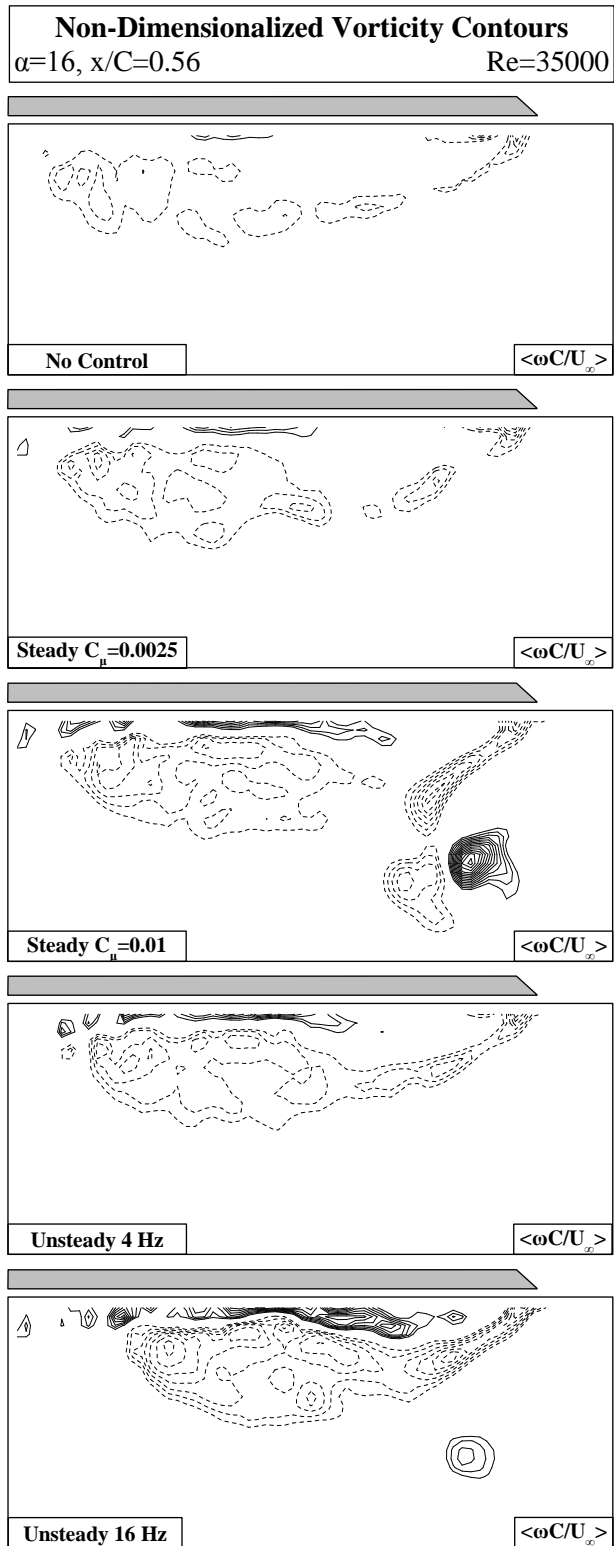


Figure 4.17 Time averaged cross flow vorticity contours at $x/C=0.56$ and $\alpha=16^\circ$ for no control, steady control $C_{\mu}=0.0025$, 0.01 and unsteady control with 4 , 16 Hz excitation frequencies.

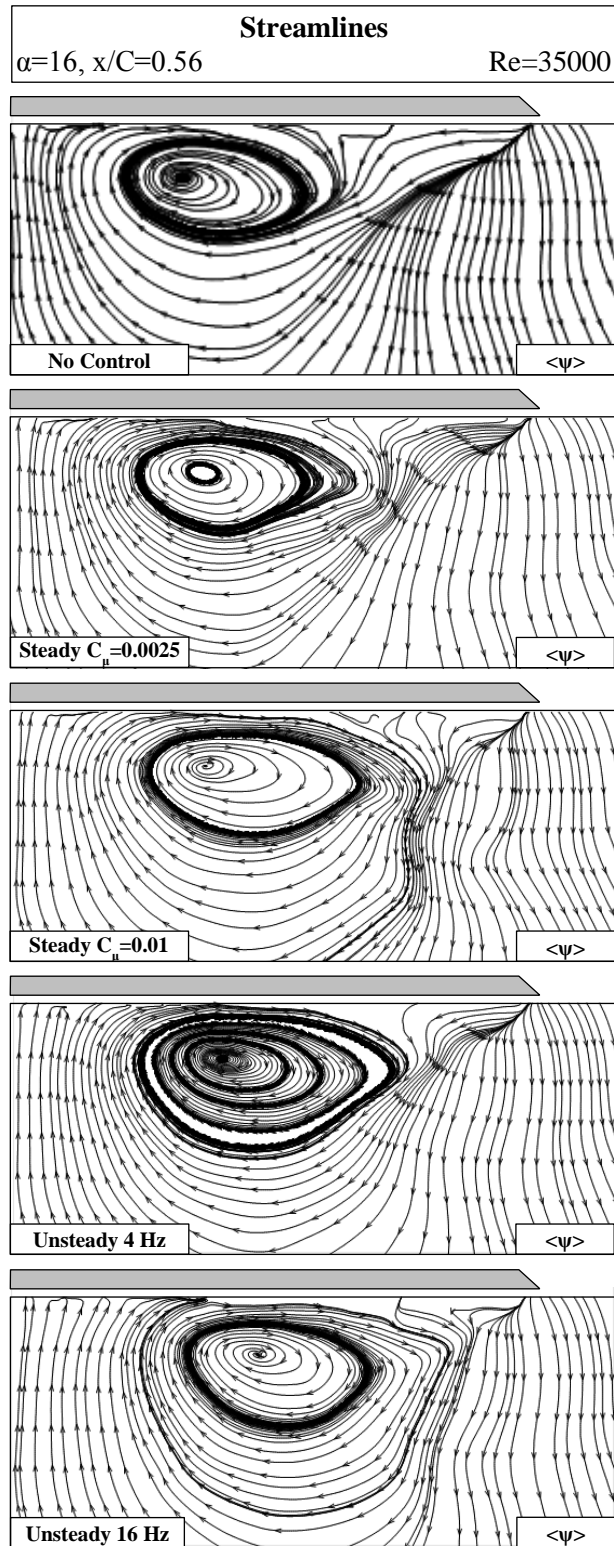


Figure 4.18 Time averaged cross flow streamline patterns at $x/C=0.56$ and $\alpha=16^\circ$ for no control, steady control $C_\mu=0.0025$, 0.01 and unsteady control with 4 , 16 Hz excitation frequencies.

CHAPTER 5

CONCLUSION

5.1 Summary and Conclusions

In this study the effect of unsteady leading edge blowing on the flow structure of a low swept delta wing with $\Lambda=45^\circ$ sweep angle was investigated. First, the unsteady blowing test set-up, which was able to provide a broad range of periodic excitation frequencies and injection rates, was built and characterized using Hot Wire Anemometry. Then, the flow structure on the wing was quantified using surface pressure measurements and Particle Image Velocimetry (PIV) technique for the attack angles of $\alpha= 7^\circ, 13^\circ, 16^\circ$ and 20° at Reynolds number of $Re=35000$. Different periodic excitation frequencies, varying from 2 Hz to 24 Hz, at fix momentum coefficient were tested and compared with the steady injection cases. The periodic excitation pattern was in the form of the square wave with a 25% duty cycle. The momentum coefficient for unsteady blowing was selected as $C_{\mu,eff}=0.0025$ which corresponds to $C_{\mu,max}=0.01$. For comparison purposes, the momentum coefficient values for steady blowing control were selected as $C_{\mu}=0.0025$ and 0.01.

Based on the results of the current study, the following conclusions can be drawn:

- Performance of the flow control set-up is found to be satisfactory in terms of achieving the desired excitation pattern, frequency, and duty cycle.
- The peaks of the suction pressure decreases and moves inboard with increasing attack angle for no control cases.
- Effect of unsteady leading edge blowing is apparent from suction peak values for all incidences with varying contributions according to the excitation frequencies.

- The pre-stall and stall incidences at $\alpha=16^\circ$ and 20° characterized by almost flat pressure distributions in no control case could be significantly improved by pulsed blowing. Especially for $\alpha=16^\circ$ the pressure distribution transforms to a state having stronger suction peaks with respect to the no control case.
- For the incidences between $\alpha=7^\circ$ and 16° , pressure fluctuations exhibits the greater values between the reattachment locations and vortex core regions where could be identified according to the lowest and peak values of $-C_p$.
- For unsteady leading edge blowing increasing excitation frequency adjusts the effect of the technique. For most of the cases 16 Hz excitation frequency is found to be the most effective one.
- For all of the incidences and most of the excitation frequencies, the unsteady leading edge blowing that has $C_{\mu,eff}=0.0025$ is found to be more actively controlling the flow compared to the steady leading edge blowing that has $C_\mu=0.0025$.
- For the significant amount of the excitation frequencies, unsteady leading edge blowing that has $C_{\mu,eff}=0.0025$ is found to be more actively controlling the flow then steady leading edge blowing that has $C_\mu=0.01$ at the incidences greater than $\alpha=7^\circ$.
- PIV experiment results reveal that the effect of unsteady leading edge blowing on flow structure is substantial at $\alpha=16^\circ$. Compared to no control and steady blowing cases, greater velocity magnitudes and condensed vorticity contours could be achieved with unsteady blowing. There exists a good agreement between the surface pressure measurement results and cross flow PIV measurements.
- Operational limits of low swept wing could be improved with unsteady leading edge blowing technique in a quite effectively. The results presented here are in line with the conclusions of Gursul et al. [3] for unsteady excitation techniques.

5.2 Recommendations for Future Work

In this thesis the effect of unsteady blowing on flow structure of a low swept delta wing has been investigated experimentally. The present study can be further improved in the following ways:

- Unsteady blowing experiments can be conducted at different momentum coefficients and excitation values for various Reynolds numbers in order to figure out the effective control parameters at different flight conditions.
- Effect of duty cycle can be investigated which represents the ratio of average of the added momentum in unsteady blowing to the maximum momentum added in open state of the valve (the total momentum added in steady blowing case with same coefficient).
- Unsteady blowing can be applied through the leading the edges of the wing with different configurations. Different hole geometries can be tested, besides phase shifted pulses can be generated and injected from different hole locations.
- Aerodynamic force measurements can be conducted to quantify the lift loads that the wing model experiences and compare with results obtained in this study.

REFERENCES

- [1] I. Gursul, R. Gordnier, and M. Visbal, “Unsteady Aerodynamics of Nonslender Delta Wings,” *Progress in Aerospace Sciences*, vol. 41, no. 7, pp. 515–557, 2005.
- [2] I. Gursul, “Vortex Flows on UAVs: Issues and Challenges,” *Aeronautical Journal*, vol. 108, no. 1090, pp. 597–610, 2004.
- [3] I. Gursul, Z. Wang, and E. Vardaki, “Review of Flow Control Mechanisms of Leading-Edge Vortices,” *Progress in Aerospace Sciences*, vol. 43, no. 7–8, pp. 246–270, 2007.
- [4] P. B. Earnshaw and J. A. Lawford, “Low-Speed Wind-Tunnel Experiments on a Series of Sharp-Edged Delta Wings,” *Aeronautical Research Council, Reports and Memoranda*, no. 3424, 1964.
- [5] C. Breitsamter, “Unsteady Flow Phenomena Associated with Leading-Edge Vortices,” *Progress in Aerospace Sciences*, vol. 44, no. 1, pp. 48–65, 2008.
- [6] I. Gursul, “Review of Unsteady Vortex Flows over Slender Delta Wings,” *Journal of Aircraft*, vol. 42, no. 2, pp. 299–319, 2005.
- [7] H. Werlé, “Quelques Résultats Expérimentaux Sur les Ailes en Flèche, aux Faibles Vitesses, Obtenus en Tunnel Hydrodynamique,” *La Recherche Aéronautique*, 1954.
- [8] J. D. Bird, “Tuft-Grid Surveys at Low Speeds for Delta Wings,” *NASA Technical Note*, 1969.
- [9] E. C. Polhamus, “Predictions of vortex-lift characteristics by a leading-edge suction analogy,” *Journal of Aircraft*, vol. 8, no. 4, pp. 193–199, 1971.
- [10] G. Erickson, “Water-Tunnel Studies of Leading-Edge Vortices,” vol. 19, no. 6, pp. 442–448, 1981.
- [11] T. B. Benjamin, “Theory of the Vortex Breakdown Phenomenon,” *Journal of Fluid Mechanics*, vol. 14, no. June, pp. 593–629, 1962.
- [12] T. Benjamin, “Some developments in the theory of vortex breakdown,”

- Journal of Fluid Mechanics*, vol. 28, no. 1, pp. 65–84, 1967.
- [13] T. Sarpkaya, “On Stationary and Travelling Vortex Breakdowns,” *Journal of Fluid Mechanics*, vol. 45, no. 03, p. 545, Mar. 1971.
- [14] T. Sarpkaya, “Vortex Breakdown in Swirling Conical Flows,” *AIAA Journal*, vol. 9, no. 9, pp. 1792–1799, 1971.
- [15] T. Sarpkaya, “Effect of the Adverse Pressure Gradient on Vortex Breakdown,” *AIAA Journal*, vol. 12, no. 5, pp. 602–607, 1974.
- [16] E. Wedemayer, “Vortex Breakdown,” *AGARD High Angle-of-Attack Aerodynamics*, no. 9, 1982.
- [17] M. Escudier, “Vortex Breakdown: Observations and Explanations,” *Progress in Aerospace Sciences*, vol. 25, no. 2, pp. 189–229, Jan. 1988.
- [18] M. Gad-El-Hak and R. F. Blackwelder, “The Discrete Vortices from a Delta Wing,” *AIAA Journal*, vol. 23, no. 6, pp. 963–962, 1985.
- [19] M. V. Ol and M. Gharib, “Leading-Edge Vortex Structure of Nonslender Delta Wings at Low Reynolds Number,” *AIAA Journal*, vol. 41, no. 1, pp. 16–26, 2003.
- [20] R. E. Gordnier and M. R. Visbal, “Compact Difference Scheme Applied to Simulation of Low-Sweep Delta Wing Flow,” *AIAA Journal*, vol. 43, no. 8, pp. 1744–1752, 2005.
- [21] G. S. Taylor, T. Schnorbus, and I. Gursul, “An Investigation of Vortex Flows Over Low Sweep Delta Wings,” *33rd AIAA Fluid Dynamics Conference and Exhibit*, no. June, pp. 1–13, 2003.
- [22] B. Yaniktepe and D. Rockwell, “Flow Structure on a Delta Wing of Low Sweep Angle,” *AIAA Journal*, vol. 42, no. 3, pp. 513–523, 2004.
- [23] W. Jin-Jun and Z. Wang, “Experimental Investigations on Leading-Edge Vortex Structures for Flow over Non-Slender Delta Wings,” *Chinese Physics Letters*, vol. 25, no. 7, pp. 2550–2553, 2008.
- [24] H. Ashley, J. Katz, M. A. Jarrah, and T. Vaneck, “Survey of Research on Unsteady Aerodynamic Loading of Delta Wings,” *Journal of Fluids and Structures*, vol. 5, no. 4, pp. 363–390, Jul. 1991.
- [25] D. Rockwell, “Three-Dimensional Flow Structure on Delta Wings at High Angle-of-Attack - Experimental Concepts and Issues,” in *31st Aerospace*

- Sciences Meeting*, American Institute of Aeronautics and Astronautics, 1993.
- [26] R. E. Gordnier and M. R. Visbal, “Unsteady vortex structure over a delta wing,” *Journal of Aircraft*, vol. 31, no. 1, pp. 243–248, 1994.
- [27] I. Gursul, “Unsteady Flow Phenomena Over Delta Wings at High Angle of Attack,” *AIAA Journal*, vol. 32, no. 2, pp. 225–231, 1994.
- [28] M. Menke, H. Yang, and I. Gursul, “Experiments on the Unsteady Nature of Vortex Breakdown over Delta Wings,” *Experiments in Fluids*, vol. 27, no. 3, pp. 262–272, 1999.
- [29] I. Gursul and W. Xie, “Buffeting Flows over Delta Wings,” *AIAA Journal*, vol. 37, no. 1, 1999.
- [30] R. C. Nelson and A. Pelletier, “The Unsteady Aerodynamics of Slender Wings and Aircraft Undergoing Large Amplitude Maneuvers,” *Progress in Aerospace Sciences*, vol. 39, no. 2–3, pp. 185–248, 2003.
- [31] G. S. Taylor and I. Gursul, “Buffeting Flows over a Low-Sweep Delta Wing,” *AIAA Journal*, vol. 42, no. 9, pp. 1737–1745, 2004.
- [32] M. M. Yavuz, M. Elkhoury, and D. Rockwell, “Near-Surface Topology and Flow Structure on a Delta Wing,” *AIAA Journal*, vol. 42, no. 2, pp. 332–340, 2004.
- [33] I. Ozturk, “Experimental Analysis of Flow Structure on Moderate Sweep Delta Wing” M.S. thesis, Dept. Mech. Eng. Dept., METU., Ankara, Turkey, 2014.
- [34] M. Zharfa, I. Ozturk, and M. M. Yavuz, “Flow Structure on Nonslender Delta Wing: Reynolds Number Dependence and Flow Control,” *AIAA Journal*, vol. 54, no. 3, pp. 880–897, 2016.
- [35] P. B. Earnshaw, “An Experimental Investigation of the Structure of a Leading Edge Vortex,” *R.A.E. Tech. Note*, no. Aero 2740 March, 1961.
- [36] M. Ozgoren, B. Sahin, and D. Rockwell, “Vortex Structure on a Delta Wing at High Angle of Attack,” *AIAA Journal*, vol. 40, no. 2, pp. 285–292, 2002.
- [37] A. J. Riley and M. V Lowson, “Development of a Three-Dimensional Free Shear Layer,” vol. 369, pp. 49–89, 1998.

- [38] M. G. Hall, "Vortex Breakdown," *Annual Review of Fluid Mechanics*, vol. 4, no. 1, pp. 195–218, 1972.
- [39] O. Lucca-Negro and T. O'Doherty, "Vortex breakdown: A review," *Progress in Energy and Combustion Science*, vol. 27, no. 4, pp. 431–481, 2001.
- [40] N. C. Lambourne and D. W. Bryer, "The Bursting of Leading-Edge Vortices-Some Observations and Discussion of the Phenomenon," *Aero. Res. Council.*, vol. 3282, pp. 1–35, 1961.
- [41] W. H. J. Wentz and D. L. Kohlman, "Vortex Breakdown on Slender Sharp-Edged Wings," *Journal of Aircraft*, vol. 8, no. 3, pp. 156–161, 1971.
- [42] M. Lowson, "Some Experiments with Vortex Breakdown (Water Tunnel Flow Visualization on Slender Delta Wings Reveal Vortex Breakdown Formation to Be a Nonaxisymmetric)," *Royal Aeronautical Society Journal*, 1964.
- [43] M. M. Yavuz, "Origin and Control of the Flow Structure and Topology on Delta Wings," Ph.D. dissertation, Dept. Mech. Eng. and Mechanics, Lehigh Univ, Bethlehem, PA., 2005.
- [44] A. Honkan and J. Andreopoulos, "Instantaneous Three-Dimensional Vorticity Measurements in Vortical Flow over a Delta Wing," *AIAA Journal*, vol. 35, no. 10, pp. 1612–1620, 1997.
- [45] D. Peake and M. Tobak, "Three-dimensional separation and reattachment," *AGARD High Angle-of-Attack Aerodynamics*, 1982.
- [46] M. Gad-el-Hak, "Flow Control: The Future," *Journal of Aircraft*, vol. 38, no. 3, pp. 402–418, 2001.
- [47] E. Vardaki, I. Gursul, G. S. Taylor, and P. Student, "Physical Mechanisms of Lift Enhancement for Flexible Delta Wings," *AIAA paper*, no. January, pp. 1–13, 2005.
- [48] G. Taylor, Z. Wang, E. Vardaki, and I. Gursul, "Lift Enhancement over Flexible Nonslender Delta Wings," *AIAA Journal*, vol. 45, no. 12, pp. 2979–2993, 2007.
- [49] Y. Liu, L. X. Zuo, and J. J. Wang, "Effects of Flexibility on Aerodynamic

- Performance of Delta Wings with Different Sweep Angles,” *Science China: Physics, Mechanics and Astronomy*, vol. 53, no. 5, pp. 915–922, 2010.
- [50] T. Goruney and D. Rockwell, “Flow Past a Delta Wing with a Sinusoidal Leading Edge: Near-Surface Topology and Flow Structure,” *Experiments in Fluids*, vol. 47, no. 2, pp. 321–331, 2009.
- [51] H. Chen, C. Pan, and J. Wang, “Effects of Sinusoidal Leading Edge on Delta Wing Performance and Mechanism,” *Science China Technological Sciences*, vol. 56, no. 3, pp. 772–779, 2013.
- [52] H. Chen and J. J. Wang, “Vortex Structures for Flow over a Delta Wing with Sinusoidal Leading Edge,” *Experiments in Fluids*, vol. 55, no. 6, pp. 1–9, 2014.
- [53] A. Çelik and M. M. Yavuz, “Effect of Edge Modifications on Flow Structure of Low Swept Delta Wing,” *AIAA Journal*, vol. 54, no. 5, pp. 1789–1797, 2016.
- [54] S. M. Klute, O. K. Rediniotis, and D. P. Telionis, “Flow Control over a Maneuvering Delta Wing at High Angles of Attack,” *AIAA Journal*, vol. 34, no. 4, pp. 662–668, 1996.
- [55] I. Gursul, E. Vardaki, P. Margaris, and Z. Wang, “Control of Wing Vortices,” *Notes on Numerical Fluid Mechanics and Multidisciplinary Design*, vol. 95, pp. 137–151, 2007.
- [56] J. Lamar and J. Campbell, “Vortex Flaps- Advanced Control Devices for Supercruise Fighters,” *Aerospace America*, 1984.
- [57] G. Spedding, T. Maxworthy, and E. Rignot, “Unsteady Vortex Flows over Delta Wings,” *Proceedings of 2nd AFOSR Workshop on Unsteady and Separated Flows*, pp. 283–287, 1987.
- [58] Q. Deng and I. Gursul, “Effect of Leading-Edge Flaps on Vortices and Vortex Breakdown,” *Journal of Aircraft*, vol. 33, no. 6, pp. 1079–1086, 1996.
- [59] T. Hu, Z. Wang, and I. Gursul, “Passive Control of Roll Oscillations of Low-Aspect-Ratio Wings Using Bleed,” *Experiments in Fluids*, vol. 55, no. 6, p. 1752, May 2014.

- [60] J. M. Kearney and A. Glezer, "Aero-Effected Flight Control Using Distributed Active Bleed," *AIAA Paper*, no. 3099, 2011.
- [61] J. Jin, K. Yee, and S. Oh, "Trailing Vortex Strength Attenuation via Chipped Wingtip Shapes," *31st AIAA Applied Aerodynamics Conference*, 2013.
- [62] N. J. Wood, L. Roberts, and Z. Celik, "Control of Asymmetric Vortical Flows over Delta Wings at High Angles of Attack," *Journal of Aircraft*, vol. 27, no. 5, pp. 429–435, 1990.
- [63] S. McCormick and I. Gursul, "Effect of Shear-Layer Control on Leading-Edge Vortices," *Journal of Aircraft*, vol. 33, no. 6, pp. 1087–1093, 1996.
- [64] H. E. Helin and C. W. Watry, "Effects of Trailing-Edge Jet Entrainment on Delta Wing Vortices," *AIAA Journal*, vol. 32, no. 4, pp. 802–804, 1994.
- [65] C. Shih and Z. Ding, "Trailing-Edge Jet Control of Leading-Edge Vortices of a Delta Wing," *AIAA Journal*, vol. 34, no. 7, pp. 1447–1457, 1996.
- [66] S. Phillips, C. Lambert, and I. Gursul, "Effect of a Trailing-Edge Jet on Fin Buffeting Introduction," *Journal of Aircraft*, vol. 40, no. 3, pp. 590–599, 2003.
- [67] S. Guillot, E. Gutmark, and T. Garrison, "Delay of Vortex Breakdown over a Delta Wing via Near-Core Blowing," *AIAA Paper*, no. 315, 1998.
- [68] A. M. Mitchell, D. Barberis, P. Molton, and J. Delery, "Oscillation of Vortex Breakdown Location and Blowing Control of Time-Averaged Location," *AIAA Journal*, vol. 38, no. 5, pp. 793–803, 2000.
- [69] Z. Wang, P. Jiang, and I. Gursul, "Effect of Thrust-Vectoring Jets on Delta Wing Aerodynamics," *Journal of Aircraft*, vol. 44, no. 6, pp. 1877–1888, 2007.
- [70] M. M. Yavuz and D. Rockwell, "Control of Flow Structure on Delta Wing with Steady Trailing-Edge Blow," *AIAA Journal*, vol. 44, no. 3, pp. 493–501, 2006.
- [71] M. M. Yavuz and D. Rockwell, "Identification and Control of Three-Dimensional Separation on Low Swept Delta Wing," *AIAA Journal*, vol. 44, no. 11, pp. 2805–2811, 2006.

- [72] I. Gursul, S. Srinivas, and G. Batta, “Active Control of Vortex Breakdown over a Delta Wing,” *AIAA Journal*, vol. 33, no. 9, pp. 1743–1745, 1995.
- [73] Y. Liu, M. Wu, J. J. Zhu, D. A. Lawrence, E. J. Gutmark, J. H. Myatt, and C. a. May, “Reactive Flow Control of Delta-Wing Vortex,” *Journal of Aircraft*, vol. 45, no. 3, pp. 880–892, 2008.
- [74] Q. Deng and I. Gursul, “Vortex Breakdown over a Delta Wing with Oscillating Leading Edge Flaps,” *Experiments in Fluids*, vol. 23, no. 4, pp. 347–352, 1997.
- [75] H. Yang and I. Gursul, “Vortex Breakdown Over Unsteady Delta Wings and Its Control,” *AIAA Journal*, vol. 35, no. 3, pp. 571–574, 1997.
- [76] M. Gad-El-Hak and R. F. Blackwelder, “Control of the Discrete Vortices From a Delta Wing,” *AIAA Journal*, vol. 25, no. 8, pp. 1042–1049, 1987.
- [77] W. Gu, O. Robinson, and D. Rockwellf, “Control of Vortices on a Delta Wing by Leading-Edge Injection,” *AIAA Journal*, vol. 32, no. 10, pp. 2134–2135, 1994.
- [78] Y. Guy, J. Morrow, and T. McLaughlin, “Control of Vortex Breakdown on a Delta Wing by Periodic Blowing and Suction,” *37th AIAA Aerospace Sciences Meeting and Exhibit*, 1999.
- [79] Y. Guy, J. Morrow, T. McLaughlin, and I. Wygnanski, “Pressure Measurements and Flow Field Visualization on a Delta Wing with Periodic Blowing and Suction,” *AIAA Paper*, 1999.
- [80] S. Morton, Y. Guy, J. Morrow, and D. Blake, “Numerical Simulation of Periodic Suction and Blowing Control of Vortex Breakdown on a Delta Wing,” *AIAA Paper*, vol. 99, no. 3195, 1999.
- [81] A. M. Mitchell and J. Délery, “Research into Vortex Breakdown Control,” *Progress in Aerospace Sciences*, vol. 37, no. 4, pp. 385–418, 2001.
- [82] S. Margalit, D. Greenblatt, A. Seifert, and I. Wygnanski, “Delta Wing Stall and Roll Control Using Segmented Piezoelectric Fluidic Actuators,” *Journal of Aircraft*, vol. 42, no. 3, pp. 698–709, 2005.
- [83] A. Kölzsch and C. Breitsamter, “Vortex-Flow Manipulation on a Generic Delta-Wing Configuration,” *Journal of Aircraft*, vol. 51, no. 5, pp. 1380–1390, 2014.

- [84] P. Jiang, Z. Wang, and I. Gursul, "Effects of Unsteady Trailing-Edge Blowing on Delta Wing Aerodynamics," *Journal of Aircraft*, vol. 47, no. 2, pp. 591–602, 2010.
- [85] C. H. Kuo and N. Y. Lu, "Unsteady Vortex Structure over Delta-Wing Subject to Transient Along-Core Blowing," *AIAA Journal*, vol. 36, no. 9, pp. 1658–1664, 1998.
- [86] E. Vardaki, Z. Wang, and I. Gursul, "Flow Reattachment and Vortex Reformation on Oscillating Low-Aspect-Ratio Wings," *AIAA Journal*, vol. 46, no. 6, pp. 1453–1462, 2008.
- [87] N. M. Williams, Z. Wang, and I. Gursul, "Active Flow Control on a Non slender Delta Wing," *Journal of Aircraft*, vol. 45, no. 6, 2008.
- [88] A. Seifert, A. Darabi, and I. J. Wagnanski, "Delay of Airfoil Stall by Periodic Excitation," *J. Aircraft*, vol. 33, no. 4, pp. 691–698, 1996.
- [89] D. P. Coiro, E. F. Bellobuono, F. Nicolosi, and R. Donelli, "Improving Aircraft Endurance Through Turbulent Separation Control by Pulsed Blowing," *Journal of Aircraft*, vol. 45, no. 3, pp. 990–1001, 2008.
- [90] S. D. Goodfellow, S. Yarusevych, and P. E. Sullivan, "Momentum Coefficient as a Parameter for Aerodynamic Flow Control with Synthetic Jets," *AIAA Journal*, vol. 51, no. 3, pp. 623–631, 2013.
- [91] "C Series Analog Output Modules," *Online*. [Online]. Available: http://www.ni.com/pdf/products/us/c_series_ao.pdf.
- [92] A. J. Wheeler and A. R. Ganji, "Experimental Uncertainty Analysis," in *Introduction to Engineering Experimentation*. 3rd ed. New Jersey: Pearson, 2010, pp. 199-237.
- [93] R. W. Fox and A. T. McDonald, "Analysis of Experimental Uncertainty" in *Introduction to Fluid Mechanics*. 6th ed. Danvers, MA: Wiley 2003, pp. 755-761.

APPENDIX A

UNSTEADY BLOWING MEASUREMENTS RAW DATA

In this appendix, time series of unsteady blowing jet velocity (no moving average applied) and the confirmation of the excitation frequencies are given:

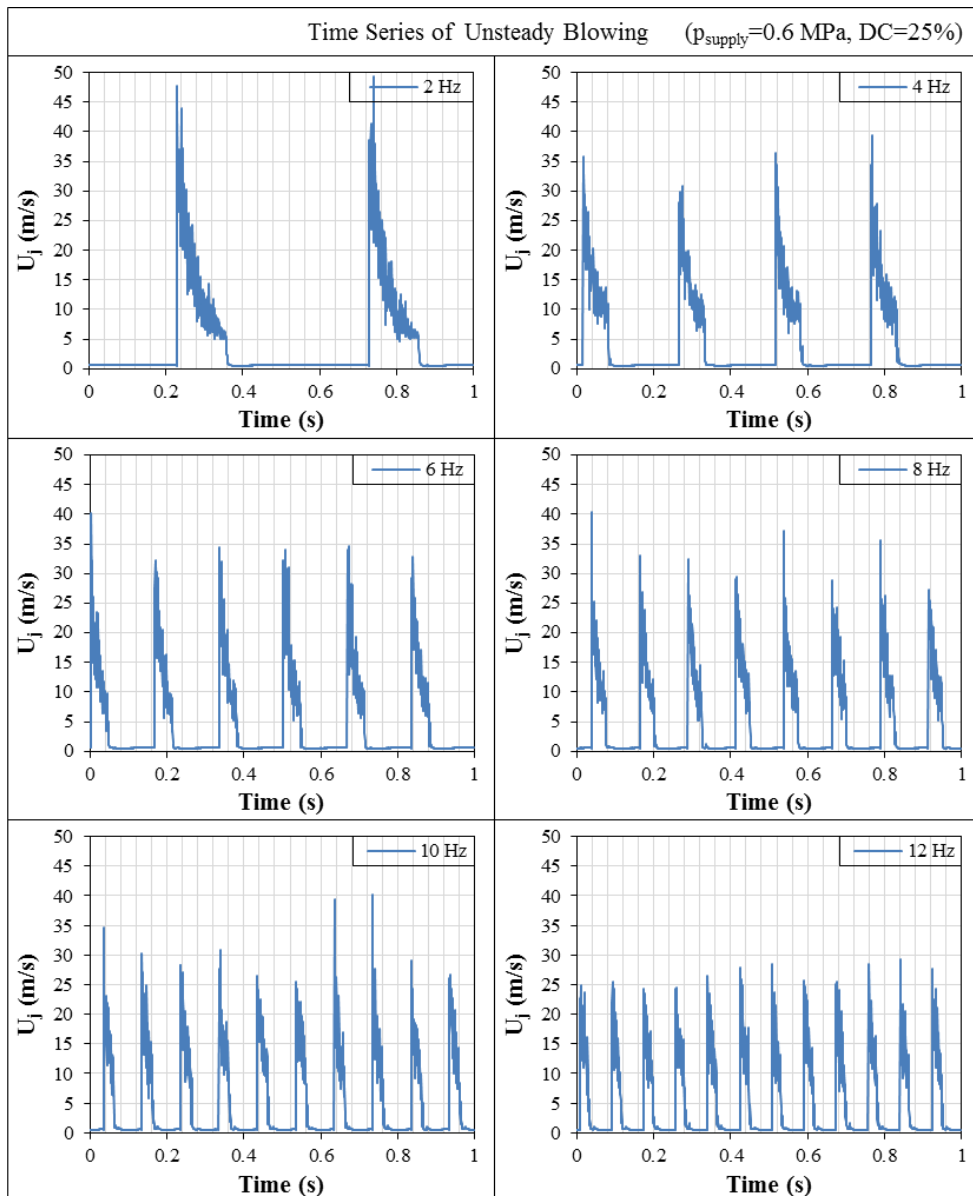


Figure A.1 Time series of unsteady blowing jet velocity for all excitation frequencies

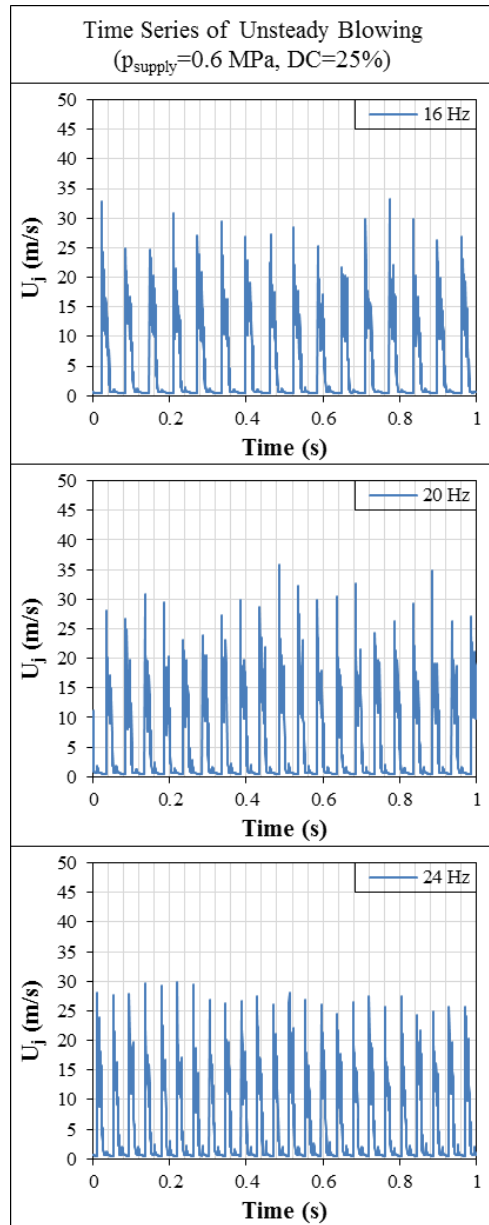


Figure A.1 (continued) Time series of unsteady blowing jet velocity for all excitation frequencies.

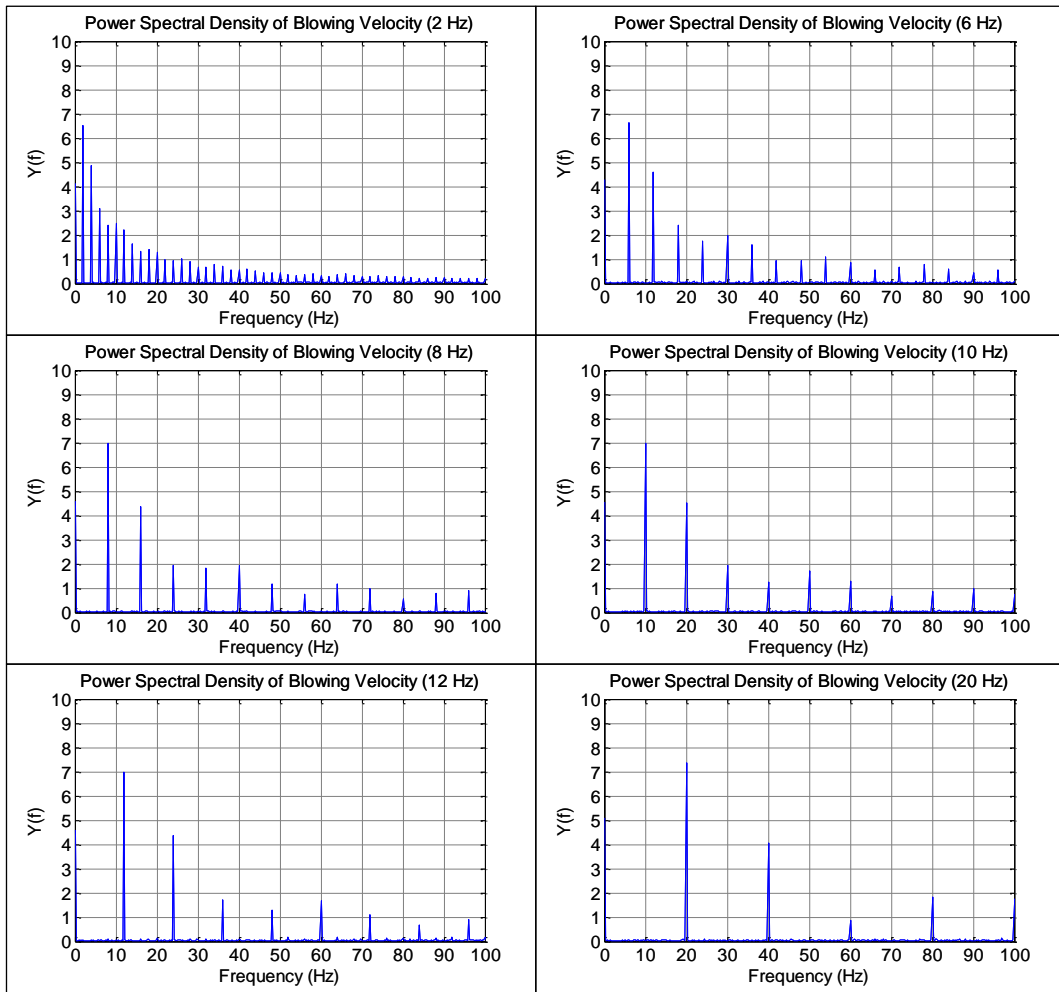


Figure A.2 Power spectral densities of unsteady blowing jet velocity for the remaining frequencies.

Source codes for power spectral analysis of jet velocity:

```
%% =====Power Spectral Analysis of Jet Velocity=====
clear all
clc

excitationFrequency = {'24'};    %% Enter the excitation frequency
m=size(excitationFrequency);

for i = 1:m(2)
    % START of data input
    filename = strcat(excitationFrequency{i}, 'Hz.xlsx');
    xlRange = 'c9:c8008';
    Data = xlsread(filename,xlRange);
    % START of Calculate Fast Fourier Transform
    figure(i)
    FsFs = 2000;                % Sampling frequency
    TT = 1/FsFs;                % Sample time
    LL = length(Data);         % Length of signal
    tt = (0:LL-1)*TT;          % Time vector

    YY = fft(Data);
    P2 = abs(YY/LL);
    P1 = P2(1:LL/2+1);
    P1(2:end-1) = 2*P1(2:end-1);
    ff = FsFs*(0:(LL/2))/LL;
    % END of Calculate FFT

    fs=14
    fgh = figure (i)
    plot(ff,P1),grid, hold on
    title('Power Spectral Density of Blowing Velocity
    (_Hz)', 'FontSize', fs);
    FigureSize = [1.0,1.0,15.0,9.0];
    set(fgh, 'Units', 'centimeters');
    set(fgh, 'Position', FigureSize);
    xlabel('Frequency (Hz)', 'FontSize', fs);
    ylabel('Y(f)', 'FontSize', fs);
    set(gca, 'fontsize', fs);
    set(gca, 'XLim', [0.0 100]);
    set(gca, 'YLim', [0 10]);
    set(gca, 'XTick', 0:10:100);
    set(gca, 'YTick', 0:1:10);
    set(gca, 'GridLineStyle', '-')
    set(gca, 'Xcolor', [0.5 0.5 0.5]);
    set(gca, 'Ycolor', [0.5 0.5 0.5]);
    Caxes = copyobj(gca,gcf);
    set(Caxes, 'color', 'none', 'xcolor', 'k', 'xgrid', 'off',
    'ycolor', 'k',
    'ygrid', 'off');
end
```

APPENDIX B

SOURCE CODES FOR PRESSURE COEFFICIENT CALCULATION

Source codes for pressure coefficient calculation, main codes:

```
clear all;
close all;
clc;
addpath ./Cenk_Exp2
%%%%%%%%%%%%%%%%%%%%%%%%%%%%%%%%%%%%%%%%%%%%%%%%%%%%%%%%%%%%%%%%%%%%%%%%
=%
% Input number of samples for the dataset
NSamples = 3;
%
[Channel] = ReadChannelInfo();
ChannelMax = max(Channel.Number);
%===== To Read the file input the following
parameters=====
alpha = [7]; % Angle of attack
Reynolds = [35]; % Reynolds No (10^3)
Cu = [0.01]; % Momentum coefficient (10^3)
Hz = [0 1025 1000 2 4 6 8 10 12 16]; % Excitation Frequency

% START of Noise data read and calculation

Noise_1 = ReadData(7,0,0,0,1);
Noise_2 = ReadData(7,0,0,0,2);
Noise_3 = ReadData(7,0,0,0,3);

MeanNoise_1 = mean(Noise_1(:,2:end),1);
DiffMat_noise1 = Noise_1(:,2:end)-ones(length(Noise_1),1)*MeanNoise_1;
RMS_noise1 = sqrt(sum(DiffMat_noise1.^2)/length(DiffMat_noise1));

MeanNoise_2 = mean(Noise_2(:,2:end),1);
DiffMat_noise2 = Noise_2(:,2:end)-ones(length(Noise_2),1)*MeanNoise_2;
RMS_noise2 = sqrt(sum(DiffMat_noise2.^2)/length(DiffMat_noise2));

MeanNoise_3 = mean(Noise_3(:,2:end),1);
DiffMat_noise3 = Noise_3(:,2:end)-ones(length(Noise_3),1)*MeanNoise_3;
RMS_noise3 = sqrt(sum(DiffMat_noise3.^2)/length(DiffMat_noise3));

MeanNoise=(MeanNoise_1+MeanNoise_2+MeanNoise_3)/3

MeanRMS_noise = (RMS_noise1 + RMS_noise2 + RMS_noise3)/3

% END of Noise data read and calculation

% START of Pressure data read and calculation

Na = length(alpha);
Nr = length(Reynolds);
Nc = length(Cu);
Nh = length(Hz);
% %
```

```

ETot = NSamples*Na*Nr*Nc*Nh;
% %

for i=1:Na
    for j=1:Nr
        for k=1:Nc
            for m=1:Nh
                for s = 1:NSamples
%
                    a = alpha(i);
                    r = Reynolds(j);
                    c = Cu(k);
                    h = Hz(m);
%
                    fprintf('Reading Alpha = %d\tReynolds=%d\t Cu=%d\t
Hz=%d\t Sample = %d \n', a,r,c,h,s);
                    Data = ReadData(a,r,c,h,s);
                    Data(:,2:end) = Data(:,2:end) -
ones(length(Data),1)*MeanNoise;
                    DataMean = mean(Data(:,2:end),1);
                    DATA{i,j,k,m}.Mean(s,:) = DataMean;
                    DiffMat = Data(:,2:end)-ones(length(Data),1)*DataMean;
                    RMS = sqrt(sum(DiffMat.^2)/length(DiffMat));
                    DATA{i,j,k,m}.RMS(s,:) = RMS;
                    % % % %

                    if(s==1)
                        DATA{i,j,k,m}.MeanTotal = DataMean;
                        DATA{i,j,k,m}.RMSTotal = RMS;
                    else
                        DATA{i,j,k,m}.MeanTotal = DATA{i,j,k,m}.MeanTotal +
DataMean;
                        DATA{i,j,k,m}.RMSTotal = DATA{i,j,k,m}.RMSTotal +
RMS;
                    end
                end
            end
        end
    end

    DATA{i,j,k,m}.MeanTotal = DATA{i,j,k,m}.MeanTotal/ NSamples;
    DATA{i,j,k,m}.RMSTotal = DATA{i,j,k,m}.RMSTotal/ NSamples;

    MeanTotal = DATA{i,j,k,m}.MeanTotal;
    RMSTotal = DATA{i,j,k,m}.RMSTotal;

    for dataDot=1:ChannelMax
        DATA{i,j,k,m}.Cp(dataDot) = (MeanTotal(ChannelMax+1)-
MeanTotal(dataDot))/(MeanTotal(ChannelMax+2)- MeanTotal(ChannelMax+1));

        DATA{i,j,k,m}.RMScp(dataDot)= RMSTotal(dataDot) /
(MeanTotal(ChannelMax+2)- MeanTotal(ChannelMax+1));
    end
end
end
end
end

% END of Pressure data read and calculation

```

```

% START of print -Cp Results
filename = '16Degree.xlsx';
excelString =
char('A1','B1','C1','D1','E1','F1','G1','H1','I1','J1','K1','L1','M1','N1
')
for i=1:length(Hz)
    xlswrite(filename,DATA{1,1,1,i}.Cp(:,1),excelString(i))
end
% END of print -Cp Results

% START of print -Cp_RMS Results
filename = '16DegreeRMS.xlsx';
excelString =
char('A1','B1','C1','D1','E1','F1','G1','H1','I1','J1','K1','L1','M1','N1
')
for i=1:length(Hz)
    xlswrite(filename,DATA{1,1,1,i}.RMScp(:,1),excelString(i))
end
% END of print -Cp_RMS Results

% START of calculate fft
figure(10)
FsFs = 500; % Sampling frequency
TT = 1/FsFs; % Sample time
LL = length(Data(:,5)); % Length of signal
tt = (0:LL-1)*TT; % Time vector

YY = fft(Data(:,5));
P2 = abs(YY/LL);
P1 = P2(1:LL/2+1);
P1(2:end-1) = 2*P1(2:end-1);
fgh1 = figure(10);
ff = FsFs*(0:(LL/2))/LL;
fss=13;
plot(ff,P1),grid ,hold on;
title('Power Spectral Density of the Pressure Signal
(\alpha=7\circ)','FontSize',fss-1)
FigureSize = [1.0,1.0,15.0,9.0];
set(fgh1,'Units','centimeters');
set(fgh1,'Position',FigureSize);
xlabel('Frequency (Hz)','FontSize',fss);
ylabel('Y(f)','FontSize',fss);
set(gca,'fontsize',fss-2);
set(gca,'XLim',[0.0 100]);
set(gca,'YLim',[0 1]);
set(gca,'XTick',0:10:100);
set(gca,'YTick',0:0.1:1);
set(gca,'GridLineStyle','-');
set(gca,'Xcolor',[0.8 0.8 0.8]);
set(gca,'Ycolor',[0.8 0.8 0.8]);
Caxes = copyobj(gca,gcf);
set(Caxes,'color','none','xcolor','k','xgrid','off','ycolor','k',
'ygrid','off');
legend('16 Hz Unsteady Control'); % Adjust the legend for respective
case.

% END of calculate FFT

```

Sub class codes to read file:

```
function [Data] = ReadData(a,r,c,h,s)
as = num2str(a);
rs = num2str(r);
cs = num2str(c);
hs = num2str(h);
ss = num2str(s);

if(c~=0)
    filename=strcat(as,'DG-Re',rs,'-',cs,'Cm-',hs,'Hz-',
    ',ss,'_Stream1.csv');
else
    filename=strcat(as,'DG-Noise-',ss,'_Stream1.csv');
end
[fid, message]=fopen(filename,'r');

for i =1:7
    line = fgetl(fid);
end

sk=1;
line = fgetl(fid);
while(line~=-1)
    line = str2num(line);

    Data(sk,:) = line;
    sk = sk+1;
    line = fgetl(fid);
end
fclose(fid);
end
```

Sub class codes to read pressure tab locations:

```
function [Data] = ReadChannelInfo()

filename = strcat('Channels2.txt');

[fid, message]=fopen(filename,'r');

line = fgetl(fid);

for i =1:12
    line = fgetl(fid);
    line = str2num(line);
    Data.Station(i)=line(1);
    Data.Number(i)=line(2);
    Data.x(i)=line(3);
end
end
```

APPENDIX C

PRESSURE MEASUREMENT RESULTS

In Appendix C dimensionless pressure distributions at a Reynolds number of 35000 for no control and all steady, unsteady control cases are given. Each figure corresponds to attack angles $\alpha=7^\circ$, 13° , 16° and 20° respectively.

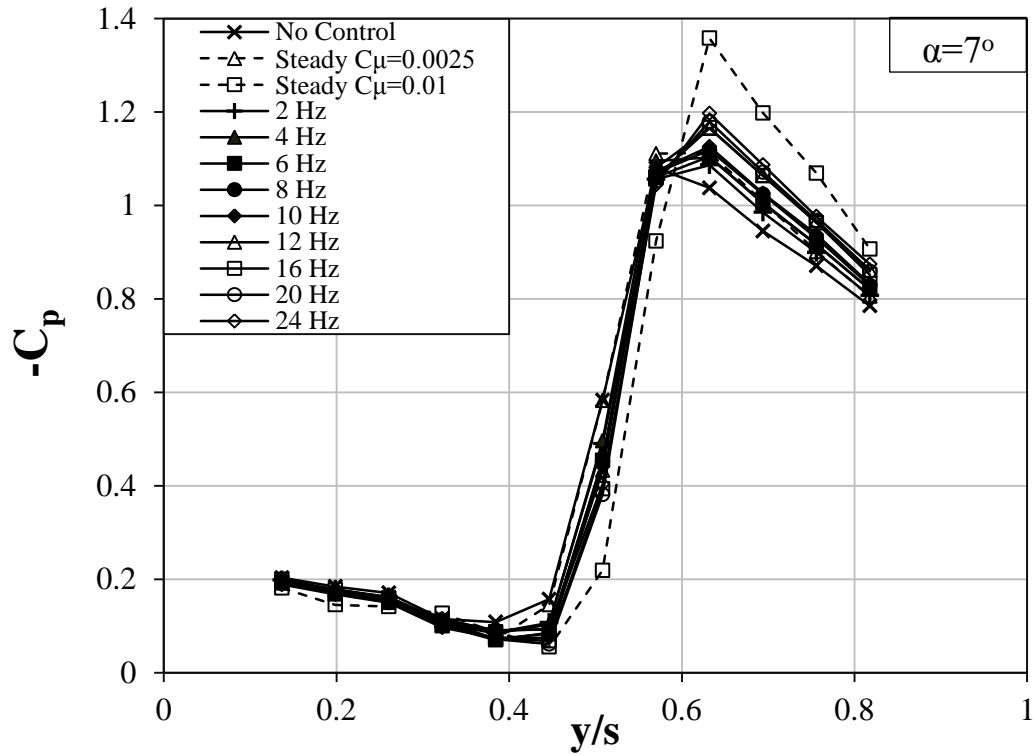


Figure C.1 Spanwise $-C_p$ distribution on $x/C=0.56$ at $\alpha=7^\circ$ and $Re=35000$ for all cases

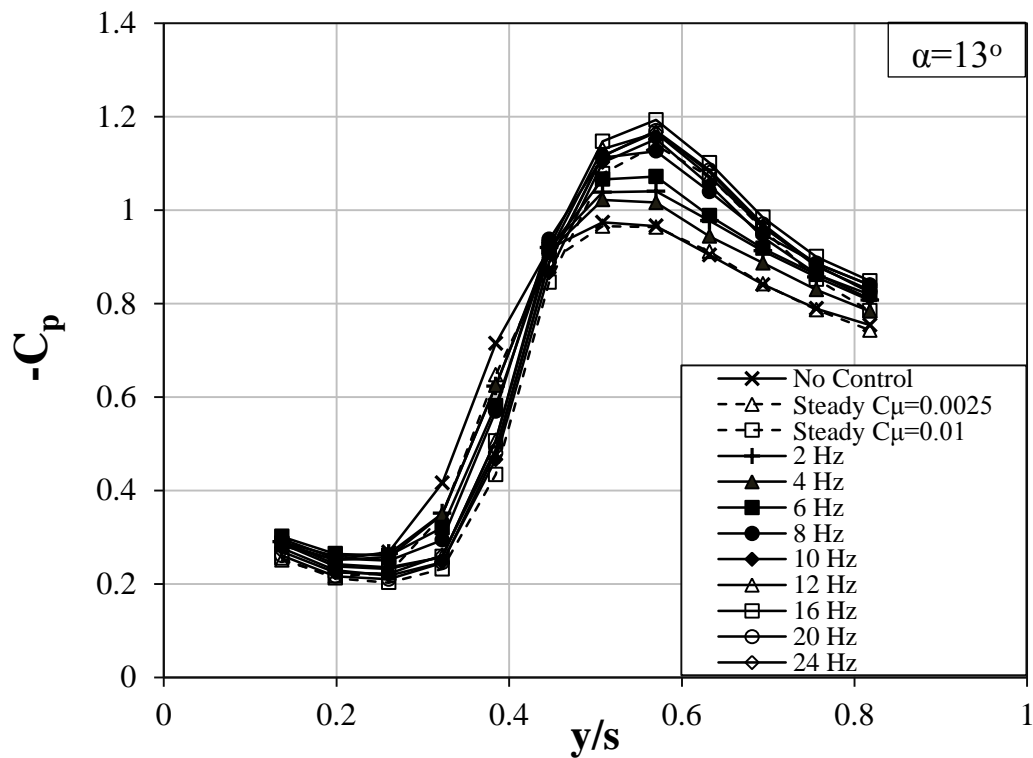


Figure C.2 Spanwise $-C_p$ distribution on $x/C=0.56$ at $\alpha=13^\circ$ and $Re=35000$ for all cases.

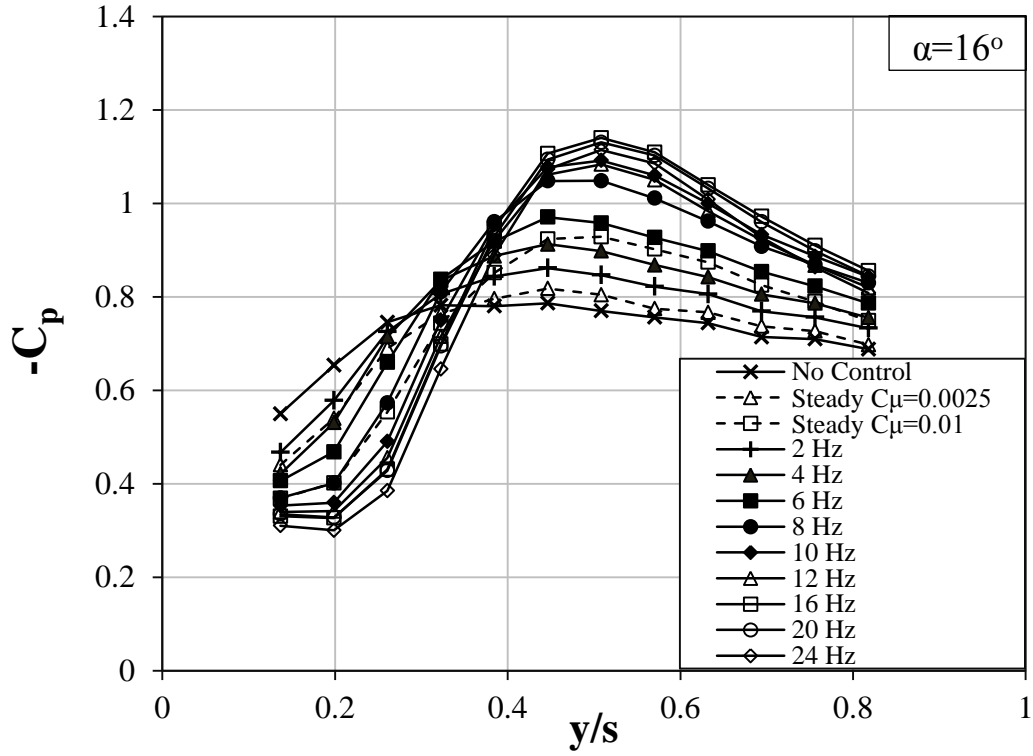


Figure C.3 Spanwise $-C_p$ distribution on $x/C=0.56$ at $\alpha=16^\circ$ and $Re=35000$ for all cases.

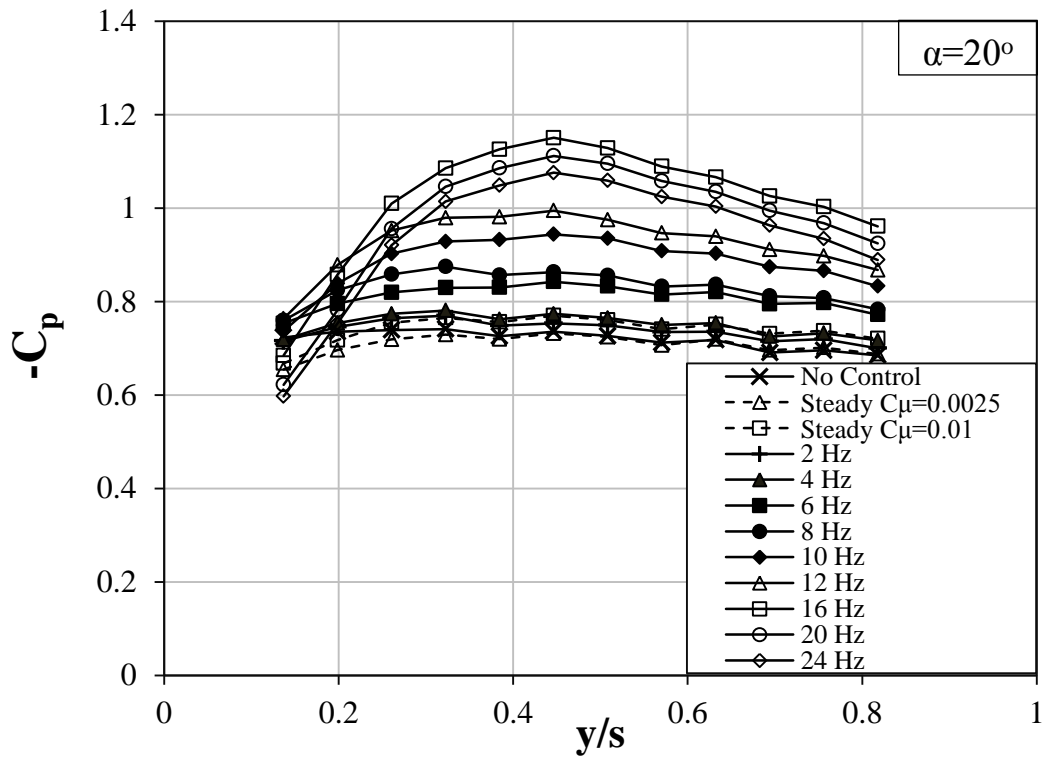


Figure C.4 Spanwise $-C_p$ distribution on $x/C=0.56$ at $\alpha=20^\circ$ and $Re=35000$ for all cases.

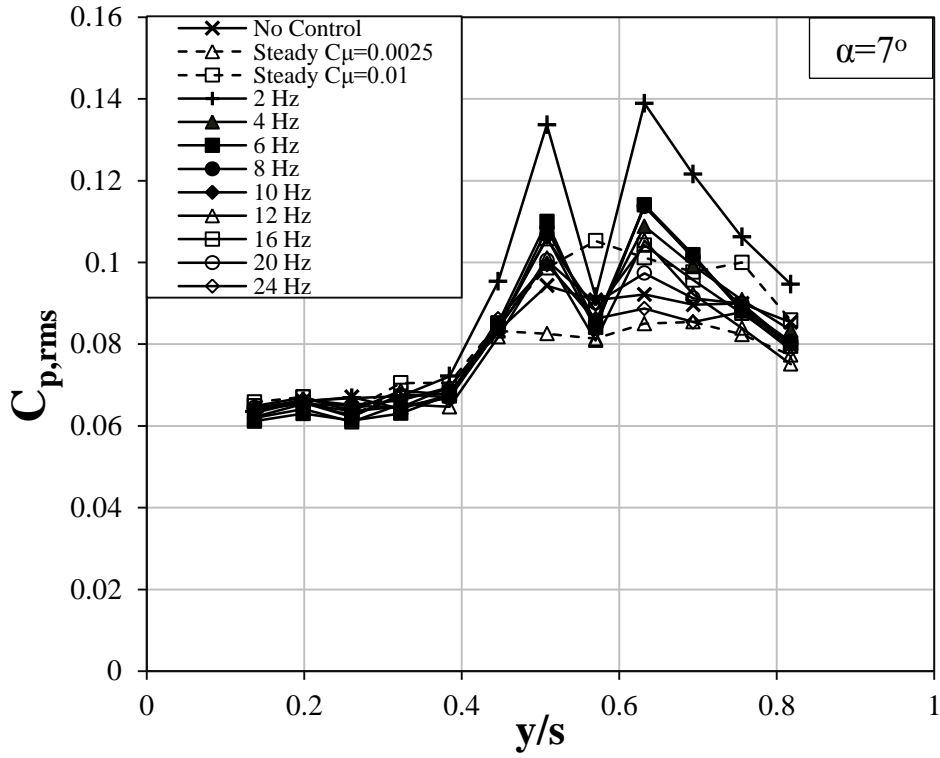


Figure C.5 Spanwise $C_{p,RMS}$ distribution on $x/C=0.56$ at $\alpha=7^\circ$ and $Re=35000$ for all cases.

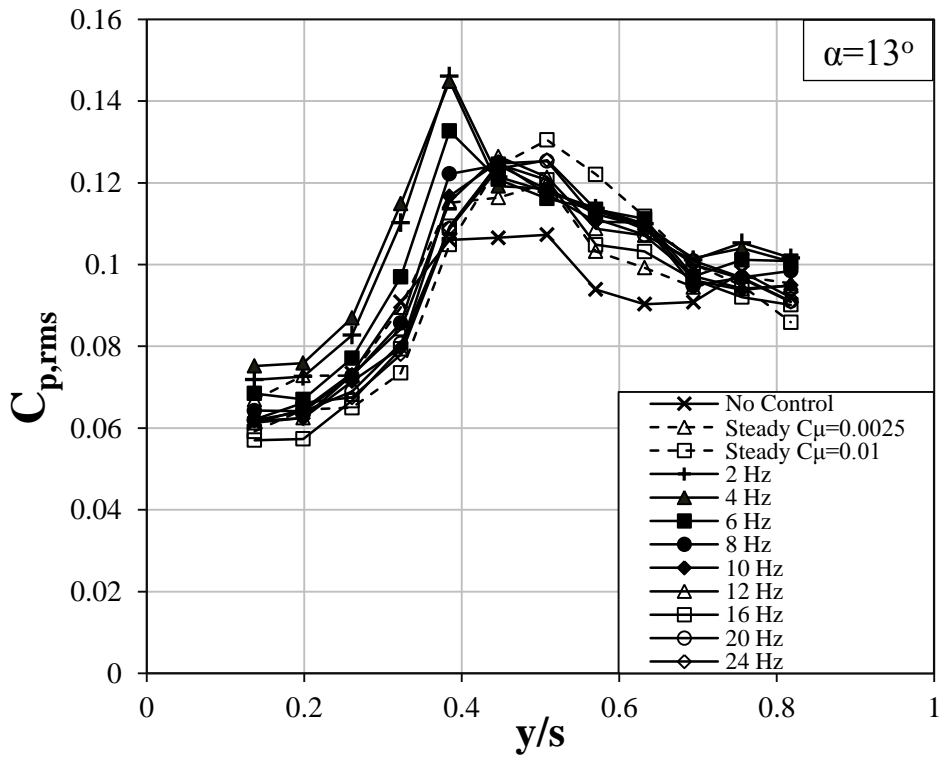


Figure C.6 Spanwise $C_{p,RMS}$ distribution on $x/C=0.56$ at $\alpha=13^\circ$ and $Re=35000$ for all cases.

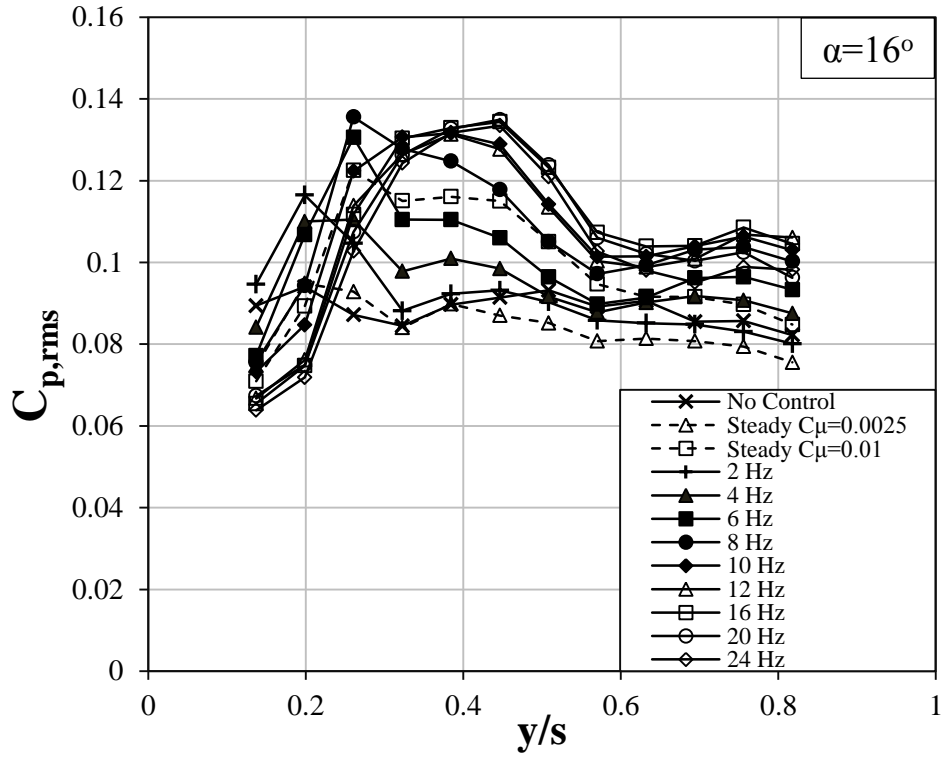


Figure C.7 Spanwise $C_{p,RMS}$ distribution on $x/C=0.56$ at $\alpha=16^\circ$ and $Re=35000$ for all cases.

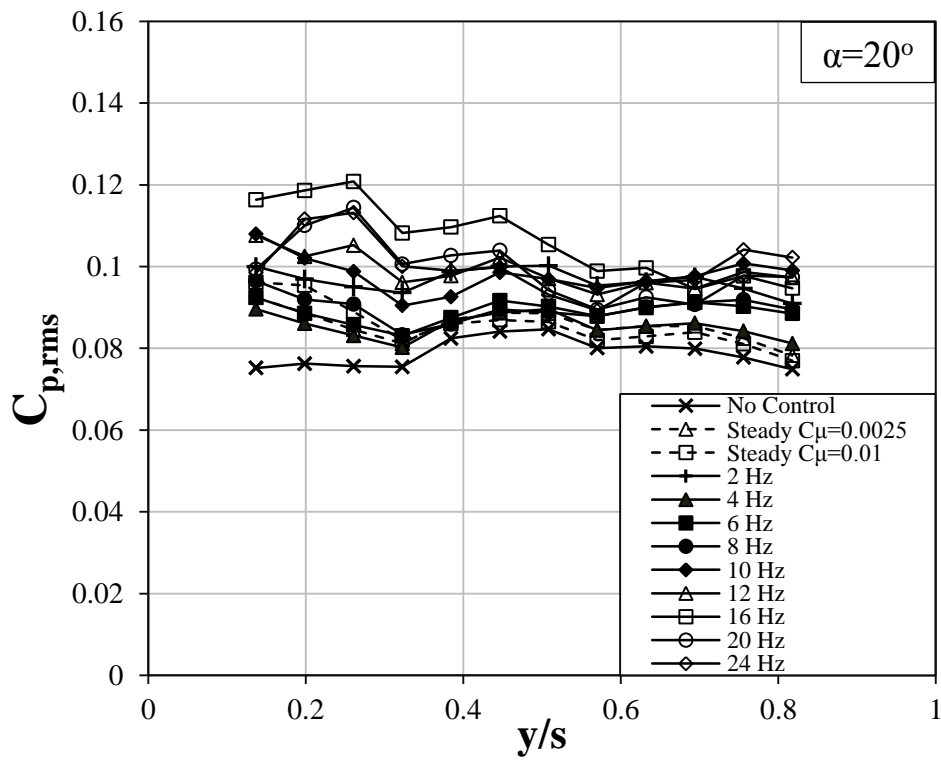


Figure C.8 Spanwise $C_{p,RMS}$ distribution on $x/C=0.56$ at $\alpha=20^\circ$ and $Re=35000$ for all cases.